TÉCNICO LISBOA

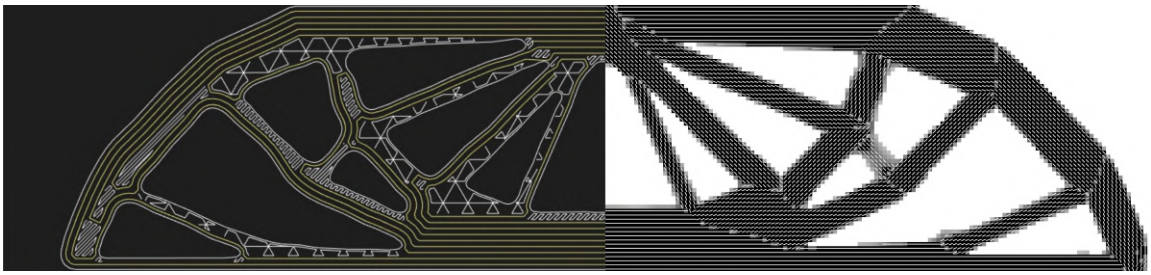

Optimization of Structures in Composite Reinforced by Fiber and Bidimensional Additive Processes

Pedro Miguel Alves da Costa

Thesis to obtain the Master of Science Degree in

Mechanical Engineering

Supervisor(s): Prof. José Arnaldo Pereira Leite Miranda Guedes
Prof. Marco Alexandre De Oliveira Leite

Examination Committee

Chairperson: Prof. Luís Filipe Galrão dos Reis
Supervisor: Prof. Marco Alexandre de Oliveira Leite
Member(s) of the Committee: Prof. Bruno Alexandre Rodrigues Simões Soares
Prof. João Orlando Marques Gameiro Folgado

December 2019

Acknowledgments

I would like to express my gratitude to Professors José Miranda Guedes and Marco Leite for the guidance given during the development of this thesis. In addition, I would also like to thank Professor Luís Reis for helping during the experimental part of this work.

I also wish to thank Professor Krister Svanberg from the Royal Institute of Technology in Stockholm, Sweden for providing the Matlab source code for the MMA optimizer.

Finally, I want to thank my family and friends for all the help, support and encouragement and for making me persevere in my work during these last stages of my academic life.

Abstract

Recently, the development of continuous fiber filament technology in the Fused Filament Fabrication process enabled the production of lighter, stronger structural parts. In order to develop optimal structures using this technology, this thesis aims to optimize the material distribution and orientation of bidimensional structures produced by FFF using continuous fiber. The finite element method is used to simulate the structure, using the Siemens NX commercial software to generate the finite element mesh and impose boundary conditions. This data is then read by the optimization program which was developed in Matlab. The optimization is performed by implementing the DMO method to discretize the fiber material orientations and the void material, together with a density filter to avoid checkerboard results. The optimization is performed using the MMA optimizer.

Using the developed Matlab program, optimizations are performed and structures are printed according to the results using the Markforged Mark Two continuous fiber 3D printer. Results show that topology optimized structures and topology with fiber orientation optimized structures, when printed with Concentric fiber fill, have similar stiffness, showing agreement with the computational results, although with significantly lower stiffness values. A technique to force the orientation of the fiber is tested for fiber orientation optimized structures, against structures printed with a quasi-isotropic layup. The results aren't conclusive if the technique is successful, requiring further investigation for different structures or boundary conditions. Structures printed with fiber aligned with the principal stress directions revealed stiffer than structures printed with a quasi-isotropic layup.

Keywords: Discrete Material Optimization (DMO), Markforged Mark Two, Fiber orientation optimization, Additive Manufacturing, Fiber reinforced composite structures

Resumo

Recentemente, o desenvolvimento de tecnologias de FFF recorrendo a fibra contínua permitiu a produção de peças estruturais mais leves e resistentes. De forma a desenvolver estruturas ótimas com recurso a estas tecnologias, o objetivo desta tese passa pela otimização da distribuição e orientação do material em estruturas bidimensionais produzidas com recurso a esta tecnologia. A estrutura é simulada utilizando elementos finitos, usando-se o software Siemens Nx para geração da malha e aplicação das condições de fronteira. Esta informação é transmitida para o programa de otimização desenvolvido em Matlab. A otimização é feita pela implementação do método DMO para discretizar as orientações da fibra e vazio, utilizando um filtro de densidade para evitar resultados em "xadrez". O optimizador MMA é utilizado para a optimização.

Usando o programa desenvolvido, são feitas otimizações sendo as estruturas daí provenientes impressas recorrendo à impressora 3D Mark Two da Markforged. Os resultados mostram que estruturas otimizadas somente quanto à topologia e estruturas também otimizadas quanto à orientação da fibra, quando impressas com preenchimento "Concêntrico" de fibra, apresentam rigidez semelhante, concordando com os resultados computacionais, no entanto com valores inferiores. Foi testada uma técnica para orientar a fibra de acordo com os resultados das otimizações, comparando os resultados com estruturas impressas com um laminado quasi-isotrópico. Os resultados revelaram-se inconclusivos quanto ao sucesso da técnica, sendo necessária uma investigação mais aprofundada. Foi também verificado que estruturas impressas com as fibras alinhadas nas direções de maior tensão são mais rígidas que estruturas impressas com um laminado quasi-isotrópico.

Palavras-chave: Discrete Material Optimization (DMO), Impressora 3D Mark Two, Otimização da orientação da fibra, Manufatura Aditiva, Estruturas em compósito reforçado por fibra

Contents

List of Tables

List of Figures

Nomenclature

Greek symbols

$\boldsymbol{\sigma}$	Stress Tensor
$\boldsymbol{\varepsilon}$	Strain Tensor
ν	Poisson's ratio
ψ^e	Shape function
ρ	Density
θ	Material orientation angle

Roman symbols

$\mathbf{B}$	Strain-displacement matrix
$\mathbf{C}$	Stiffness Tensor/Material constitutive matrix
$\mathcal{C}$	Compliance
E	Young's modulus
f	Volume fraction
G	Shear modulus
h	Thickness
h_ϵ	DMO convergence
$\mathbf{J}$	Jacobian matrix
$\mathbf{K}$	Global stiffness matrix
$\mathbf{K}^e$	Element stiffness matrix
M	Maximum mass of the structure
m	Mass of the structure
m_c	Mass constraint

N^e	Number of finite elements
n^e	Number of discrete materials
$\mathbf{p}$	Applied forces vector
p	Penalization factor
R	Relative change of design variables
r	Filter radius
$\mathbf{T}(\theta)$	Coordinate transformation matrix
$\mathbf{u}$	Nodal displacements vector
V	Volume
w_i	Weight factors
$\mathrm{w}^e(\mathbf{x}_i)$	Linear decaying weight function
x_i	Design variables

Superscripts

T	Transpose

Acronyms

2D	Two-dimensional
3D	Three-dimensional
3PT	Three-Point Tensile
AM	Additive Manufacturing
ASTM	American Society for Testing and Materials
BESO	Bidirectional Evolutionary Structural Optimization
BMP	Bitmap
CAD	Computer Aided Design
CCSA	Conservative Convex Separable Approximation
CFAO	Continuous Fiber Angle Optimization
CFC	Composite Fiber Coextrusion
CFF	Continuous Fiber Fabrication
DMO	Discrete Material Optimization
ESO	Evolutionary Structural Optimization
FFF	Fused Filament Fabrication
FRC	Fiber Reinforced Composite
FRTPC	Fiber Reinforced Thermoplastic Composite
MBB	Messerschimitt-Bölkow-Blohm
MMA	Method of Moving Asymptotes
SIMP	Solid Isotropic Material with Penalization
SLP	Sequential Linear Programming
SOMP	Solid Orthotropic Material with Penalization
SQP	Sequential Quadratic Programming

Chapter 1

Introduction

This chapter will provide an introduction to the subjects presented in this thesis. The motivation for this work as well as previous developments will be presented, concluding with the determination of the objectives for this thesis and its outline.

1.1 Structural Optimization

Optimization refers to the process of finding the ”best” or optimal solution for a given problem which can have certain restrictions. This solution is normally obtained by a process of trial and error, which begins with an original solution that will be analyzed, evaluated and improved, resulting in a new, preferably better solution. This process continues until no further improvements are possible and the solution is deemed optimal [1]. This methodology has been applied all over the human history and the process can also be observed in nature, through the concept of evolution and natural selection.

Structural optimization thus refer to obtaining the optimal structure subject to certain loads/ displacements normally with restrictions defined by the engineer. The concept of optimal can vary according to the imposed specifications that characterize the optimization objective. In structural optimization, the objective can be such as making the lightest structure , e.g. minimize weight, or the opposite by designing the stiffest structure e.g. maximizing stiffness. Of course these examples cannot be implemented without imposing constraints, as the former would result in a non-existent structure and the latter wouldn’t have limitations in the amount of material that could be used. Both cases implying a poorly defined optimization problem [2]. The most common methods used in structural optimization can be divided into three categories: size, shape and topology optimization. Size and shape optimizations were the first methods to be developed and are usually performed when the design is already in its final stages. Size optimization can be used to determine the optimal thickness distribution over the structure or overall dimensions. Shape optimization modifies the geometry of the structure, to prevent stress concentrations or optimize the material distribution. Topology optimization is used to determine the optimal material distribution from an initial design domain, by removing material were it’s not needed, normally introducing holes in the structure [1].

1.2 Fused Filament Fabrication

Additive manufacturing (AM) technologies have found potential applications in various industries such as the aerospace and automotive industries by allowing the creation of complex lightweight structures. These technologies allow the fabrication of prototypes or functional components with complex structures such as those obtained by topology optimization, which could be too expensive to manufacture by conventional methods, and also difficult, if not impossible [3].

One of these technologies is the Fused Filament Fabrication (FFF) method which consists in reproducing a three-dimensional geometry through the deposition of successive layers of extruded thermoplastic filament. This technology has become widely adopted due to its low cost, low material wastage and ease of use. The most common materials used by this process include Polycarbonate (PC), Polylactic acid (PLA), Acrylonitrile butadiene styrene (ABS) and Polyamide (PA or Nylon), due to their low cost and low melting temperature [4]. However, the poor mechanical properties of parts printed using these materials results in the FFF process being primarily used to develop prototypes [5]. In order to improve the mechanical properties of 3D printed parts, the combination of a polymeric matrix with reinforcements such as particles, fibers and nano-materials allows the manufacture of structural parts, characterized by their high-performance and functionality [3]. These advantages lead to the recent development of 3D printing technology of Fiber Reinforced Thermoplastic Composite (FRTPC) structures using short and continuous fibers. The first commercial printer capable of producing continuous fiber reinforced composite structures was the Mark One, developed by Markforged, using their patented technology of Continuous Fiber Fabrication (CFF). Since then, Markforged developed several others CFF 3D printers both for the consumer as well as the professional market [6]. A more recent example of FFF using continuous fiber can be found in the Composer printers, produced by the Anisoprint company, which uses their patent pending technology of Composite Fiber Coextrusion (CFC) [7].

1.3 Motivation

With the increasing development of additive manufacturing, the technology started to shift from initial prototyping, where prototypes were developed to quickly bring ideas to life or to check dimensional problems, to functional prototyping, were working, structural parts are created and ready to use. This change implied the use of stronger materials than thermoplastic polymers, such as PLA and ABS. An example of these materials are carbon fiber and fiberglass, that when applied as reinforcement in a polymeric matrix structure results in a Fiber Reinforced Composite (FRC) structure.

Although the use of fibers tends to improve the overall strength and stiffness of parts produced by Fused Filament Fabrication, this improvement is only relevant when the fibers are oriented towards the stresses that the part is set upon. Also, the use of these materials greatly increases the cost of production, resulting in the need for them to be used efficiently.

For these reasons, this thesis aims to optimize in terms of stiffness both the topology and material orientation of parts produced by FFF technology using continuous fiber as reinforcement.

1.3.1 State of the Art

Topology optimization as it is today began as a variation of shape optimization. Bendsøe and Kikuchi [8] were among the first to study this branch of structural optimization using the homogenization method. Instead of placing or removing material, the material's microstructure is composed of voids with varying sizes and orientations. By modifying the shape and orientation of these voids in each cell, the problem transforms from a shape optimization problem, in which the design domain changes constantly, into a sizing optimization problem, simplifying the whole process. A modification for the homogenization method was developed by Suzuki and Kikuchi [9] and tested for various examples of linearly elastic structures using shape and topology optimization.

Xie and Steven [10] proposed a topology optimization method inspired by the evolution of natural structures. This process, designated as Evolutionary Structural Optimization (ESO) method, computes the stress distribution across the structure using a finite element analysis and eliminates elements based on a rejection criterion such as the Von Mises stress being less than an established rejection ratio. This process is repeated until a steady state is reached. Afterwards, to the rejection ratio is added an evolution rate and the process continues until it reaches a new steady state. The optimization proceeds until a desired optimum is reached. Since the method functions by eliminating elements, a global optimum solution cannot be guaranteed and also the generation of high stress zones created by the elimination of material could not be alleviated with the addition of material. This lead to the development of the Bidirectional Evolutionary Structural Optimization (BESO) method, proposed by Querin et al. [11]. This method starts from a minimum possible design space and using a bidirectional technique, which adds or removes material, the structure evolves until an optimal solution is found.

Another approach to topology optimization is the Solid Isotropic Material with Penalization (SIMP) method, developed independently by Bendsøe [12] , Zhou and Rozvany [13] and Mlejnek [14]. Instead of introducing voids in the material microstructure as the homogenization method, or removing low-stressed finite elements as the ESO method, the SIMP methodology assumes the material properties constant for all the elements in the discretized domain and the design variables are the relative densities of each element, which vary between 0 and 1. Each elements material is then modeled by multiplying the isotropic solid material with the corresponding element relative density raised to a designated power. This method, also called "the power-law approach", is used to penalize intermediate densities and drive them to the values of 0 and 1, corresponding to void and solid material, respectively. An implementation of the method was developed by Sigmund [15] in Matlab, using a 99 line topology optimization code which could be modified to solve various structural optimization problems. A variation of the SIMP method using an orthotropic material model designated as Solid Orthotropic Material with Penalization (SOMP) method was used by Lee et al. [16] and Hoglund [17] to study the influence in topology results when using an orthotropic material with a specified orientation.

With the increasing use of fiber reinforced composites in areas of the industry such as the aerospace and automotive industry, a new branch of structural optimization designated by fiber orientation optimization emerged. The objective of this type of optimization is to find the optimal orientation for orthotropic material, such as fiber reinforced composites. The first studies regarding the optimal material orienta-

tion were developed by Pedersen [18, 19, 20] and Gibiansky and Cherkaev [21] with the former using a strain based method and the latter a stress method. The results obtained by these studies, confirmed by Suzuki and Kikuchi [9] , suggest that for ”weak” shear materials the optimal material orientation coincides with the principal stresses and strains direction.

One of the most straightforward methods used to optimize the orthotropic material orientation is the so-called Continuous Fiber Angle Optimization (CFAO) method [22–24] which uses the orientation angle itself as a design variable. This approach, however, has some local minima issues, as noted and illustrated by Stegmann [1], with the global design space becoming non-convex with the use of the continuous angle as design variable. Despite these issues, it has proven to be successful in simultaneously optimizing topology and fiber orientation, since it can easily be integrated with the SIMP method. This methodology was used by Jia et al. [25] in the optimization for minimal compliance of a cantilever beam. Recently, the use of the CFAO method with the SIMP approach was used by Hoglund [17] and Hoglund and Smith [26] for the two dimensional topology and fiber orientation optimization, with focus on structures printed using the FFF process with short fiber reinforced filament. This combination of CFAO + SIMP was latter implemented by Jiang [27] for the three dimensional model.

In order to avoid the local minima issues found using CFAO, Nomura et al. [28, 29] proposed a general topology optimization method capable of dealing with the material distribution design as well as continuous or discrete material orientation. This method employs a Cartesian representation for the orientation angle, using unit vectors. A transformation of the bound box of the Cartesian components is performed using isoparametric shape functions, into a circular element with unity radius. The transformation ensures continuity and prevents solution ambiguity. The design variables are regularized using a Helmholtz filter with a Heaviside function. The method was tested for the short cantilever problem, noting the resulting fiber orientation being coincident with the direction of the structural bars, confirming the results from previous studies.

Another method that was developed to tackle the local minima problem present in the CFAO method is the Discrete Material Optimization (DMO) method [1, 30]. This method determines the most appropriate material from a set of given options, with these ranging from a single material with different orientations to multiple materials. By reducing the number of possible angle configurations, the risk of encountering local minima diminishes, although with an increase of computational time as the number of design variables increases. The original parametrizations developed by Stegmann for the DMO method consist in representing the element constitutive matrix as a weighted sum formulation of the various materials constitutive matrices. These weights vary between 0 and 1, with a material being selected when its corresponding weight has the value of 1 and the others 0. The optimizers ability to select a single material determines the success of the method. Although this approach does not cover continuously varying orientation distributions problems, as can be found in the FFF process, an approximation can be achieved by using several orientation angles as design variables, with the already mentioned increase in computation time. To address this issue, several new parametrization schemes were developed [31, 32] that reduce the number of design variables while maintaining the number of possible orientation angles. However, these were not implemented in the present work.

1.4 Objectives

The objective of this thesis is to develop an optimization algorithm capable of optimizing material distribution and orientation for structures subject to plane stress. The algorithm has to be capable of reading and processing information provided by a commercial finite element software regarding the structures geometry, loading conditions and constraints. The computational results obtained from the algorithm will then be compared against the experimental results of structures printed using CFF.

As such, the key aspects of this work are:

- Implement an optimization algorithm for material distribution and orientation using the DMO method and a robust optimizer;
- Compare the optimization results with experimental data obtained by testing FRTPC structures using continuous fiber and similar boundary conditions.

1.5 Thesis Outline

This thesis is divided in 5 chapters.

Chapter 1 introduces the background for the developed work, revealing the motivation and objectives of this thesis.

Chapter 2 is dedicated to the optimization algorithm, detailing the governing equations, sensitivity analysis, filtering and the optimizer.

Chapter 3 treats the finite element model, detailing the equations behind the triangular and quadrilateral finite element. The implementation of the developed algorithm is also described and computational results are presented.

Chapter 4 deals with the experimental part of this thesis. Material properties for parts printed using Markforged's Mark Two printer are obtained and structures are printed and tested, according to the computational results. An analysis of the experiments is performed.

Chapter 5 is dedicated to the conclusions drawn from the present work and possibilities for future works are presented.

Chapter 2

Optimization

In this chapter, the formulation of the optimization problem is presented. The objective and constraints of the problem are defined as well as the design variables. The parametrization method known as Discrete Material Optimization (DMO) method is introduced and the objective function and sensitivity analysis are defined. Finally, the gradient-based optimizer known as Method of Moving Asymptotes (MMA) is presented, having been developed and provided by Krister Svanberg.

2.1 Problem Formulation

The formulation of an optimization problem is a process of transforming a real, tangible problem into a mathematical model. In order to do this, several stages must be considered:

- Objective - What it's trying to achieve, what are the desired goals.
- Design Variables - What parameters are being changed to achieve those goals.
- Objective Function - How can the problem be translated to a mathematical model.
- Constraints - What are the problem's limitations.

These 4 stages are what constitute the problem formulation. After the completion of these stages we are able to produce a mathematical formula for our design optimization problem. Once this is done the optimization process can begin. First we start with an initial design, which is then analyzed and calculated. If the conditions for optimum are not met, the design is altered according to a set of rules, generating a new design. This iterative process is performed until an optimum solution is achieved. In Fig. 2.1 we can observe how this process is done.

2.1.1 Objective

As was said earlier in 2.1, the objective is a description of the problem that we are trying to optimize, its requirements or goals and its limitations.

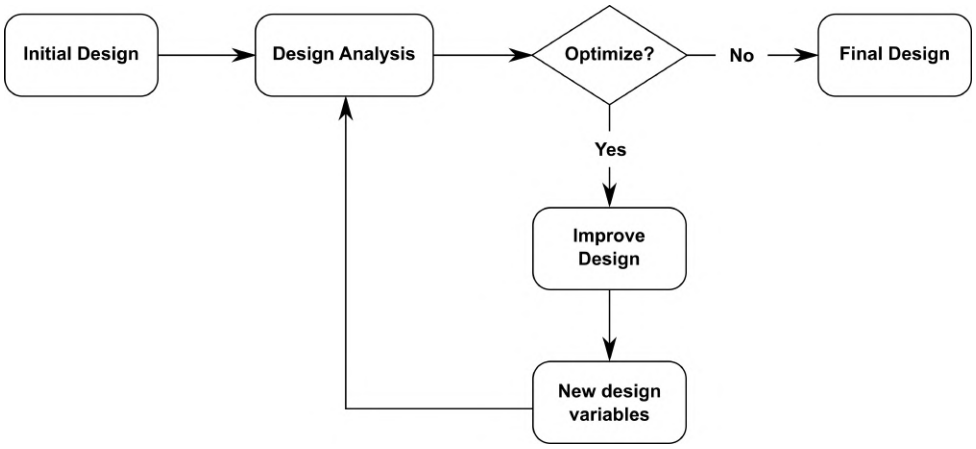

Figure 2.1: Flowchart of the optimization process

In this thesis, the optimization problem consists of maximizing the stiffness of a given structure under certain loads and boundary conditions while maintaining its weight under a certain threshold. The material that this structure is made of has an orthotropic nature.

2.1.2 Design Variables

As stated in 2.1, this stage serves to define the variables that will be changed in order to improve upon our design. These variables should be as much independent from each other as possible, i.e, the value of one variable should not affect the value of another. The number of *degrees of freedom* that a problem possesses is based on the number of independent design variables.

In 2.1.1 it was stated that the objective was to maximize the stiffness of a structure made of an orthotropic material. Contrary to isotropic materials, which have no preferred directions in the material, having infinite number of planes of material symmetry, orthotropic materials have three mutually orthogonal planes of material symmetry [33]. This means that, as opposed to isotropic materials, orthotropic materials have different material properties, depending on the direction at a certain point. As such, this should be exploited when optimizing for the stiffness of a structure.

In order to model the behavior of an orthotropic material under a given load or stress, we can make use of the so called *generalized Hooke's Law* (2.1), assuming that we are in the elastic regime of the material.

$$\boldsymbol{\sigma} = \mathbf{C} \cdot \varepsilon \tag{2.1}$$

In (2.1), $\boldsymbol{\sigma}$ is the stress tensor, ε is the strain tensor and $\mathbf{C}$ is the stiffness tensor. In matrix notation, equation (2.1) is written as:

$$\begin{Bmatrix} \sigma_{11} \\ \sigma_{22} \\ \sigma_{33} \\ \sigma_{23} \\ \sigma_{13} \\ \sigma_{12} \end{Bmatrix} = \begin{bmatrix} C_{11} & C_{12} & C_{13} & C_{14} & C_{15} & C_{16} \\ C_{21} & C_{22} & C_{23} & C_{24} & C_{25} & C_{26} \\ C_{31} & C_{32} & C_{33} & C_{34} & C_{35} & C_{36} \\ C_{41} & C_{42} & C_{43} & C_{44} & C_{45} & C_{46} \\ C_{51} & C_{52} & C_{53} & C_{54} & C_{55} & C_{56} \\ C_{61} & C_{62} & C_{63} & C_{64} & C_{65} & C_{66} \end{bmatrix} \cdot \begin{Bmatrix} \varepsilon_{11} \\ \varepsilon_{22} \\ \varepsilon_{33} \\ 2\varepsilon_{23} \\ 2\varepsilon_{13} \\ 2\varepsilon_{12} \end{Bmatrix} \tag{2.2}$$

Eq. (2.2) relates to a generic elastic material. If we assume this material is hyperelastic, then the stiffness coefficients C_{ij} must be symmetric, i.e, $C_{ij} = C_{ji}$. This leaves us with 21 unique stiffness coefficients.

For orthotropic materials this number is reduced to 9 stiffness coefficients due to the 3 planes of symmetry these materials possess at any given point. Because of this and substituting C_{ij} for the corresponding expressions featuring the engineering constants such as Young's modulus E, Poisson ratio ν and shear modulus G, the stiffness tensor $\mathbf{C}$ in (2.2) can be rewritten as:

$$\mathbf{C} = \begin{bmatrix} \frac{1-\nu_{23}\nu_{32}}{E_2E_3\Delta} & \frac{\nu_{21}+\nu_{23}\nu_{31}}{E_2E_3\Delta} & \frac{\nu_{31}+\nu_{21}\nu_{32}}{E_2E_3\Delta} & 0 & 0 & 0 \\ \frac{\nu_{21}+\nu_{23}\nu_{31}}{E_2E_3\Delta} & \frac{1-\nu_{13}\nu_{31}}{E_1E_3\Delta} & \frac{\nu_{32}+\nu_{12}\nu_{31}}{E_1E_3\Delta} & 0 & 0 & 0 \\ \frac{\nu_{31}+\nu_{21}\nu_{32}}{E_2E_3\Delta} & \frac{\nu_{32}+\nu_{12}\nu_{31}}{E_1E_3\Delta} & \frac{1-\nu_{12}\nu_{21}}{E_1E_2\Delta} & 0 & 0 & 0 \\ 0 & 0 & 0 & G_{23} & 0 & 0 \\ 0 & 0 & 0 & 0 & G_{31} & 0 \\ 0 & 0 & 0 & 0 & 0 & G_{12} \end{bmatrix} \tag{2.3}$$

$$\Delta = (1 - \nu_{12}\nu_{21} - \nu_{23}\nu_{32} - \nu_{13}\nu_{31} - 2\nu_{21}\nu_{32}\nu_{13})/(E_1E_2E_3)$$

in the principal directions of the material.

For isotropic materials the number of stiffness coefficients is further reduced to 3, while the number of independent elastic coefficients, i.e, engineering constants, necessary to fully characterize the material are 2.

$$\mathbf{C} = \begin{bmatrix} \frac{E}{1-\nu^2} & \frac{\nu E}{1-\nu^2} & \frac{\nu E}{1-\nu^2} & 0 & 0 & 0 \\ \frac{\nu E}{1-\nu^2} & \frac{E}{1-\nu^2} & \frac{\nu E}{1-\nu^2} & 0 & 0 & 0 \\ \frac{\nu E}{1-\nu^2} & \frac{\nu E}{1-\nu^2} & \frac{E}{1-\nu^2} & 0 & 0 & 0 \\ 0 & 0 & 0 & \frac{E}{2(1+\nu)} & 0 & 0 \\ 0 & 0 & 0 & 0 & \frac{E}{2(1+\nu)} & 0 \\ 0 & 0 & 0 & 0 & 0 & \frac{E}{2(1+\nu)} \end{bmatrix} \tag{2.4}$$

It is important to note that all these equations are written in the principal directions of the material which is not very useful because the loads and boundary conditions applied to the material will be written in the problem system of coordinates. In order to write all the necessary equations in the same

coordinate system, we need to perform a transformation of coordinates in the form of

$$\boldsymbol{\sigma}_t = \mathbf{T}(\theta)\,\mathbf{C}\,\mathbf{T}(\theta)^T\boldsymbol{\varepsilon}_t \tag{2.5}$$

in which $\boldsymbol{\sigma}_t$ and $\boldsymbol{\varepsilon}_t$ are written in the problem coordinate system, θ is the angle between x_1 and x, assuming that $x_3 = z$ (see Fig. 2.2) and $\mathbf{T}(\theta)$ is written as

$$\mathbf{T}(\theta) = \begin{bmatrix} \cos^2\theta & \sin^2\theta & 0 & 0 & 0 & -2\cos\theta\sin\theta \\ \sin^2\theta & \cos^2\theta & 0 & 0 & 0 & 2\cos\theta\sin\theta \\ 0 & 0 & 1 & 0 & 0 & 0 \\ 0 & 0 & 0 & \cos\theta & \sin\theta & 0 \\ 0 & 0 & 0 & -\sin\theta & \cos\theta & 0 \\ \cos\theta\sin\theta & -\cos\theta\sin\theta & 0 & 0 & 0 & \cos^2\theta - \sin^2\theta \end{bmatrix} \tag{2.6}$$

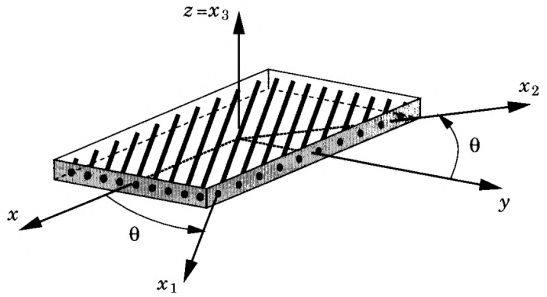

Figure 2.2: A lamina with material and problem coordinate system.[1]

Another design variable that should be accountable is the density of the material, as this is the only way to maintain the mass under a certain threshold as stated in the objectives in 2.1.1. This can be done in two different ways. Either we assume a pseudo-density as a design variable, with values between 0 and 1, as done by the SIMP method and then multiplying this pseudo-density by the stiffness tensor $\mathbf{C}$ or, in case we are already assuming discrete orientations of the orthotropic material as being different materials, we can simply add a low density, low stiffness isotropic material in order to simulate a void material, as suggested by Stegmann [1] for the DMO method.

2.1.3 Objective Function

In 2.1.1 we defined the objective as maximizing the stiffness of a given structure, in the elastic regime. As known from solid mechanics, the stiffer the structure, the smaller the displacement caused by a given applied force. This means that by maximizing the stiffness, we are actually minimizing the work produced by the applied forces in the structure. This is also known as *compliance*, $\mathcal{C}$, and will be our objective function. It's normal to use finite element analysis (see [34]) in structural optimization as is the

[1] Figure taken from J. N. Reddy. *Mechanics of Laminated Composite Plates and Shells: Theory and Analysis*. CRC Press, London, 2nd edition, 2004. ISBN 9780203502808. doi: 10.1201/b12409

case of this problem, and so we can write the compliance in finite element notation as

$$\mathcal{C} = \mathbf{p}^T \mathbf{u} = \mathbf{u}^T \mathbf{K}\, \mathbf{u} \tag{2.7}$$

were $\mathbf{p}$ are the forces applied, $\mathbf{u}$ are the displacements of the structure and $\mathbf{K}$ is the stiffness matrix of the structure, also known as global stiffness matrix.

In order to establish a connection between the objective structure and our design variables, we will be using finite elements as was discussed. As such, we can write the linear static equilibrium equation as

$$\mathbf{K}\, \mathbf{u} = \mathbf{p} \tag{2.8}$$

In finite elements, the global stiffness matrix is the sum of all the elemental stiffness matrix and so

$$\mathbf{K} = \sum_{e=1}^{N^e} \mathbf{K}^e \tag{2.9}$$

with

$$\mathbf{K}^e = \int_{V^e} \mathbf{B}^T\, \mathbf{C}\, \mathbf{B}\, dV \tag{2.10}$$

in which $\mathbf{K}^e$ is the element stiffness matrix, $\mathbf{B}$ is the strain-displacement matrix and $\mathbf{C}$ is the stiffness tensor defined in (2.1).

2.1.4 Constraints

As mentioned before, a mass constrain can be imposed in the optimization, which needs to be defined. This constraint can be formulated as

$$m < m_c \tag{2.11}$$

in which m is the sum of the weight of all elements in the structure and defined as:

$$m = \sum_{e=1}^{N^e} \rho_e V_e \tag{2.12}$$

with ρ_e and V_e being the density and the volume of the element, respectively. In (2.11) the parameter m_c is the allowed mass, which in this case is the maximum possible mass multiplied by the desired volume fraction f:

$$m_c = M \times \frac{V_{desired}}{V_{total}} = M \times f \tag{2.13}$$

2.2 DMO

DMO stands for Discrete Material Optimization and was developed by Jan Stegmann for his PHD thesis in 1994 [1]. It was created in order to improve upon the already established CFAO method as this approach had trouble dealing with local minima. This method uses ideas from topology optimization

where instead of having to choose between solid material and void, we are choosing between any number of different materials or, in the case of this thesis, different orientations of the same material and void material.

In order to be able to use gradient based optimizers when performing optimization with discrete materials, DMO implements methods similar to those used in *multiphase topology optimization*, first used by Sigmund and Torquato [35]. These methods, used at the finite element level, involve expressing the element constitutive matrix, $\mathbf{C}^e$, as a weighted sum of the material constitutive matrices (also known as stiffness tensors) $\mathbf{C}_i$ (2.1) of the different discrete materials, n^e:

$$\mathbf{C}^e = \sum_{i=1}^{n^e} w_i \mathbf{C}_i = w_1 \mathbf{C}_1 + w_2 \mathbf{C}_2 + \ldots + w_{n^e} \mathbf{C}_{n^e}, \quad 0 \leq w_i \leq 1 \tag{2.14}$$

By allowing the weight factors w_i to assume values between 0 and 1, the DMO method transforms this discrete optimization problem into a problem with a continuum design domain. These weight factors must remain between these values as it's not physically possible to have negative material properties and a material cannot contribute with more than his physical material properties.

It falls to the optimizer to select the optimal material for any given finite element in a matrix by pushing the weight factor associated with its constitutive matrix $\mathbf{C}_i$ to 1 and all the others to 0. This way the initial discretization of materials is achieved by having the weight factor functioning as "on/off switches" for the different materials, achieving convergence for a given element when only one single material is chosen.

To aid the optimizer in this endeavor, several interpolation schemes for the weight factors were developed by Stegmann. The design variables x_i in these schemes could start with any value between 0 and 1 but the best practice is to start all with the same value so as to not favor any material. The following schemes are the ones that were used for this work, as they are the ones that generate the best results according to Stegmann. They each have positive and negative aspects that will also be discussed.

DMO scheme 4

This scheme is an improvement from previous ones presented by Stegmann [1] and has each design variable x_i affecting all the weight factors:

$$\mathbf{C^e} = \sum_{i=1}^{n^e} \underbrace{\left[(x_i^e)^p \prod_{j=1; j \neq i}^{n^e} [1 - (x_j^e)^p] \right]}_{w_i} \mathbf{C}_i \tag{2.15}$$

This is achieved by having the term $(1 - (x_j^e)^p)$ which, if there's an increase in x_i, prompting an increase in the weight factor w_i, causes a decrease in all other weight factors and vice-versa. The exponent p is a penalization that is imposed in order to further help the optimizer to push the values of w_i towards 0/1. The manner in which this interpolation scheme behaves as p changes is demonstrated in Fig. 2.3 using two materials. As can be seen, as p increases, the steeper the curve and the faster the weight factor w_i reaches 0 as x_i decreases.

Although this scheme proves to be very successful in pushing the weight factors to the values of 0/1,

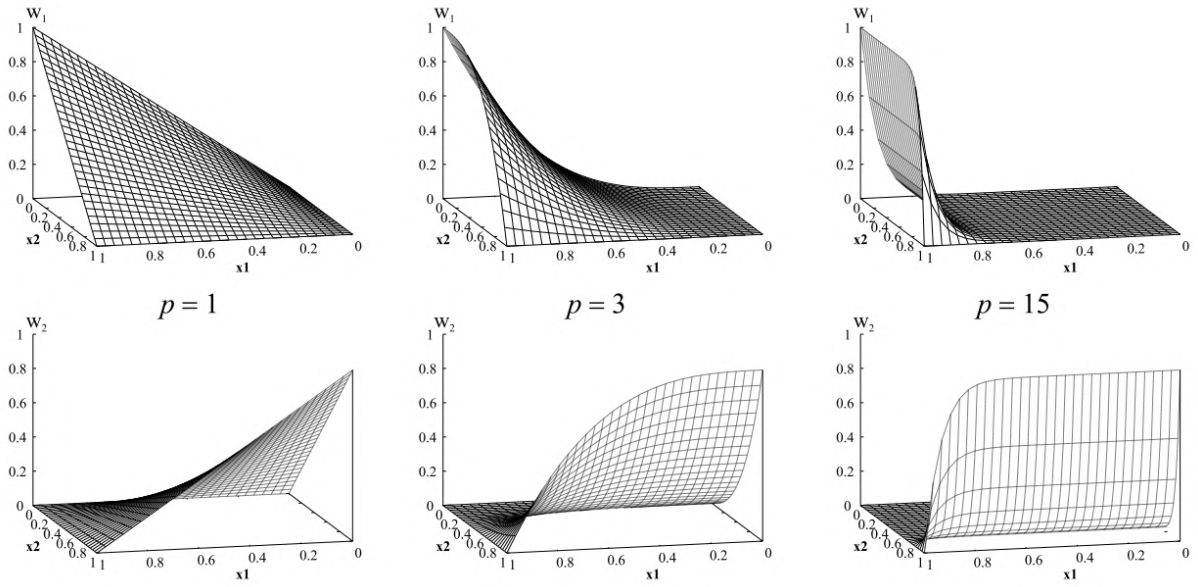

Figure 2.3: Weight functions, w_1 and w_2, for two materials, computed with DMO scheme 4. Top and bottom row represent w_1 and w_2, respectively.[2]

its main drawback is that generally the sum of the weight factors does not equal to one, i.e $\sum w_i \neq 1$. If we were only optimizing for material orientation, this would not be very troublesome, as although the initial stiffness would be too low, it would be slowly pushed to the physical stiffness as the solution converged to the "optimum" and in the end this sum would be indeed 1. If we are also evaluating for a mass constraint, this is problematic due to the poor scaling of results, as initially the optimizer might "assume" that the constraint are being satisfied but in reality, they are not. For this reason, the following scheme was developed, normalizing the weight factors.

DMO scheme 5

As mentioned, DMO scheme 5 is a modification of DMO sheme 4 developed in order to ensure that the sum of the weight factors always equals to one, i.e. $\sum w_i = 1$. This is accomplished by calculating $\hat{w}_i$ the same way as in (2.15) and then normalizing the weight factors by dividing for their sum.

$$\mathbf{C^e} = \sum_{i=1}^{n^e} \underbrace{\frac{\hat{w}_i}{\sum_{k=1}^{n^e} \hat{w}_k}}_{w_i} \mathbf{C}_i \qquad \hat{w}_i = (x_i^e)^p \prod_{j=1;j\neq i}^{n^e} [1-(x_j^e)^p] \tag{2.16}$$

As can be seen in Fig. 2.4, which shows the behavior of this interpolation scheme for different values of penalization p, as the value of the penalization increases, it increases the number of favorable combinations of design variables, represented by the flat regions that can be seen when $p = 15$. As such, although this scheme is faster to converge to a "near optimum" value, it can not effectively drive the design variables to 0/1, for the reasons explained above. However, because this scheme ensures

[2]Figure taken from J. Stegmann. *Analysis and optimization of laminated composite shell structures*. PhD thesis, Aalborg University, 2004. URL `https://www.researchgate.net/publication/235219180_Analysis_and_Optimization_of_Laminated_Composite_Shell_Structures`

that $\sum w_i = 1$, it becomes useful for dealing with the physical constraint that we will be imposing, i.e. mass constraint, for if we were using DMO scheme 4 and the design variables for a certain element had a very low value, its mass would also have a very low value, but if we use DMO scheme 5, now the computed mass would be accurate.

Due to this fact, Stegmann [1] proposed to use DMO scheme 4 for stiffness interpolation combined with DMO scheme 5 to compute the physical constraints. This type of combined interpolation was the one used in this work.

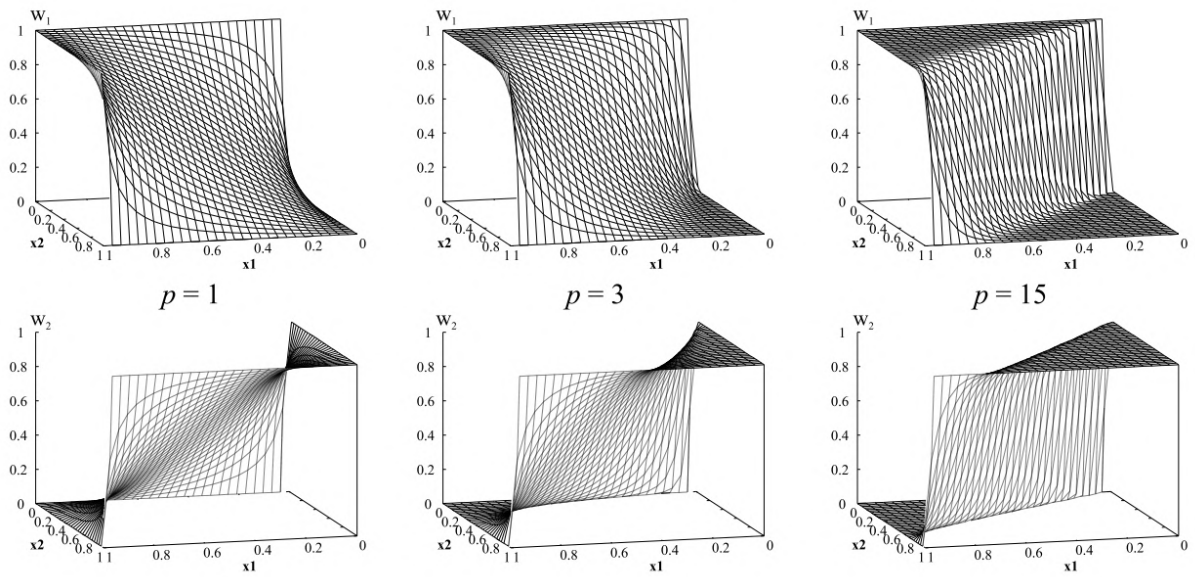

Figure 2.4: Weight functions, w_1 and w_2, for two materials, computed with DMO scheme 5. Top and bottom row represent w_1 and w_2, respectively.[3]

2.3 Optimization Problem

Having defined the objectives, design variables, objective function and constraints of the problem, the discrete material optimization problem, subject to a mass constraint, can be stated as:

$$\left.\begin{aligned} Objective: \quad & \min_x \ \mathcal{C}(x) = \mathbf{p}^T \mathbf{u} \\ Subject\ \ to: \quad & m \leq m_c \\ & 0 \leq x_{min} \leq x \leq 1 \\ & \mathbf{K}\,\mathbf{u} = \mathbf{p} \end{aligned}\right\} \tag{2.17}$$

As seen in Section 2.1.4, m is the mass of the structure and m_c is the allowable mass, defined as the maximum possible mass for the structure multiplied by a constraint. (see (2.13))

[3]Figure taken from J. Stegmann. *Analysis and optimization of laminated composite shell structures*. PhD thesis, Aalborg University, 2004. URL `https://www.researchgate.net/publication/235219180_Analysis_and_Optimization_of_Laminated_Composite_Shell_Structures`

The mass of the structure, m, is calculated as the sum of the weighted mass of all candidate materials, n^e, over all elements, N^e, i.e.

$$m = \sum_{e=1}^{N^e} \sum_{i=1}^{n^e} (w_i \rho_i V)^e \tag{2.18}$$

where ρ_i is the physical material density of the candidate material i, written in SI units as $[kg/m^3]$.

When doing pure fiber angle optimization, since there's no change of mass from the different fiber orientations, the volume fraction f in the allowable mass should be set above 1, as to allow the optimizer to only choose fiber for the optimization. When performing fiber angle optimization with topology optimization, f should be set between 0 and 1, forcing the optimizer to choose a percentage of void material for the final structure based on this constraint.

2.3.1 Sensitivity Analysis

In optimization, the optimizer needs to know how the objective function and the constraints will react to a change in the design variables and if this change improves the performance of the design while obeying the imposed constraint. To accomplish this, the gradients of these functions need to be calculated and passed to the optimizer.

The compliance sensitivity can be calculated as:

$$\frac{d\mathcal{C}}{dx_i} = \frac{d}{dx_i}(\mathbf{p}^T \mathbf{u}) = \frac{\partial \mathbf{p}^T}{\partial x_i}\mathbf{u} + \mathbf{p}^T \frac{\partial \mathbf{u}}{\partial x_i} = \mathbf{p}^T \frac{\partial \mathbf{u}}{\partial x_i} \tag{2.19}$$

The first partial derivation equals to zero since the applied forces don't depend on the design variables. From (2.8), we can substitute in (2.19), which gives us:

$$\frac{d\mathcal{C}}{dx_i} = \mathbf{u}^T \mathbf{K} \frac{\partial \mathbf{u}}{\partial x_i} \tag{2.20}$$

At this point we still don't know how $\mathbf{u}$ changes with x_i. If we now take (2.8) and differentiate in respect to the design variables we get:

$$\frac{d}{dx_i}(\mathbf{K}\,\mathbf{u}) - \frac{d}{dx_i}\mathbf{p} = 0 \Rightarrow \frac{\partial \mathbf{K}}{\partial x_i}\mathbf{u} + \mathbf{K}\frac{\partial \mathbf{u}}{\partial x_i} = 0 \Rightarrow \mathbf{K}\frac{\partial \mathbf{u}}{\partial x_i} = -\frac{\partial \mathbf{K}}{\partial x_i}\mathbf{u} \tag{2.21}$$

Substituting (2.21) into (2.20) and noting that the i'th design variable only affects the stiffness matrix on the element level, the compliance sensitivity can finally be written as:

$$\frac{d\mathcal{C}}{dx_i} = -(\mathbf{u}^e)^T \frac{\partial \mathbf{K}^e}{\partial x_i}\mathbf{u}^e \tag{2.22}$$

As for the mass constraint sensitivity, by rearranging the terms in (2.11) and differentiating in respect to the design variables, the following equation is obtained:

$$\frac{d}{dx_i}m - \frac{d}{dx_i}m_c \tag{2.23}$$

Substituting for (2.18) and taking into account that m_c is a constant:

$$\frac{d}{dx_i}\sum_{e=1}^{N^e}\sum_{j=1}^{n^e}(w_j\rho_j V)^e \tag{2.24}$$

By observing again that the i'th design variable influences the mass on the element level, the mass constraint sensitivity can then be written as:

$$\frac{d}{dx_i}\sum_{j=1}^{n^e}(w_j\rho_j V)^e \tag{2.25}$$

Obtaining the derivative of the stiffness matrix in (2.22) consists in obtaining the derivative of the element constitutive matrix $\mathbf{C}^e$ (2.14) as can be deduced from (2.10), since each element is dependent on a set of independent variables x_i. This derivative can be stated as:

$$\frac{\partial \mathbf{K}^e}{\partial x_i} = \int_{V^e} \mathbf{B}^T \frac{\partial \mathbf{C}^e}{\partial x_i}\mathbf{B}\, dV \tag{2.26}$$

with

$$\frac{\partial \mathbf{C}^e}{\partial x_i} = \frac{\partial w_1}{\partial x_i}\mathbf{C}_1 + \frac{\partial w_2}{\partial x_i}\mathbf{C}_2 + \ldots + \frac{\partial w_{n^e}}{\partial x_i}\mathbf{C}_{n^e} \tag{2.27}$$

with both the derivatives of $\mathbf{C}^e$ and (2.25) consisting in differentiating the polynomials of the employed DMO schemes. As an example, the derivatives of the polynomials from DMO schemes 4 and 5 will now be shown for 3 candidate materials.

DMO scheme 4 derivatives

Using 3 candidate materials, the DMO scheme 4 polynomials are written as:

$$\begin{aligned} w_i &= x_i^p(1-x_j^p)(1-x_k^p) \\ w_j &= x_j^p(1-x_i^p)(1-x_k^p) \\ w_k &= x_k^p(1-x_i^p)(1-x_j^p) \end{aligned} \tag{2.28}$$

The derivation of these polynomials is very simple and will be written as an example only for the first two weight factors, w_i and w_j, and the first design variable, x_i, as the remaining derivations are very similar. These can be written as:

$$\frac{dw_i}{dx_i} = p\, x_i^{p-1}(1-x_j^p)(1-x_k^p) \qquad \frac{dw_j}{dx_i} = -p\, x_i^{p-1}x_j^p(1-x_k^p) \tag{2.29}$$

As can be seen in (2.29), if w and x have matching indices, the derivative will be similar to the one on the left, and if they have different indices, the derivative will be similar to the one on the right.

DMO scheme 5 derivatives

As can be seen in (2.16), the weight factors in DMO scheme 5 are a modification of the ones used in DMO scheme 4 (2.28) and will be written here in a compact format:

$$\hat{w_i} = \frac{w_i}{w_i + w_j + w_k} \qquad \hat{w_j} = \frac{w_j}{w_i + w_j + w_k} \qquad \hat{w_k} = \frac{w_k}{w_i + w_j + w_k} \tag{2.30}$$

These functions are of the type $\left(\frac{b}{a}\right)$ and their derivatives are written as:

$$\left(\frac{b}{a}\right)' = \frac{b'a - ba'}{a^2} \tag{2.31}$$

From here, writing the derivatives of the different weight factors is also very similar and so only the derivative for the i'th design variable for w and x will be presented here:

$$\frac{d\hat{w_i}}{dx_i} = \frac{\frac{dw_i}{dx_i}(w_i + w_j + w_k) - w_i \frac{d}{dx_i}(w_i + w_j + w_k)}{(w_i + w_j + w_k)^2} \tag{2.32}$$

2.3.2 Material filter

When performing material distribution based topology optimization, two important issues that significantly influence the computational results and therefore should be avoided are the appearance of checkerboard designs and mesh-dependency [36]. The checkerboard problem gets its name for the pattern of solid and void elements organized in a checkerboard like design, which can be seen in Fig. 2.5, and is related to the bad numerical modeling of the linear Q4-displacement elements generally used in these optimizations that attribute an artificially high stiffness to these types of layouts. Mesh-dependence concerns the effect that different sized meshes generate different optimal solution (Fig. 2.6). These solutions tend to be increasingly complex and more detailed as the mesh size increases, generating designs which make better use of the material without changing the volume of the structure, leading to an increase in efficiency. However, this creates a problem for topology optimization as the near infinite amount of solutions poses questions for what structure should be implemented.

To deal with these issues, several solutions were developed by various authors, with some being implemented in the final code. The first consideration was using higher order elements to deal with the checkerboard patterns, as the improved numerical calculations that these elements have avoid these. Although these resolved the problems of checkerboarding, they don't resolve the problem of mesh dependency, and increase the computation time. In order to deal with both these issue the best method is to use a filtering technique.

Filtering techniques are methods that work by establishing a dependence between design variables of a specific element with those from neighboring elements, situated inside a fixed radius region. By establishing this dependence, the "new" design variables become weighted averages of those inside the fixed region. This in turn mitigates the appearance of checkerboard patterns as these regions would appear as *grey regions*, regions without a defined material which are penalized by the imposed penal-

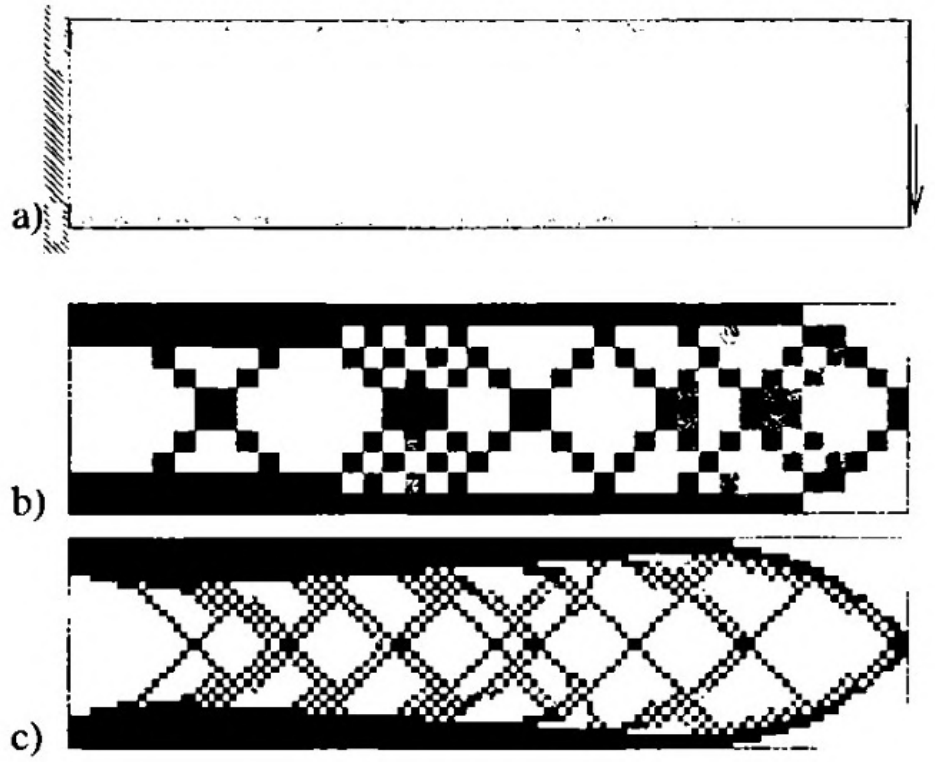

Figure 2.5: The checkerboard problem demonstrated on a long cantilever beam. a) Design problem, b) solution for 400 element discretization and c) solution for 6400 element discretization.[4]

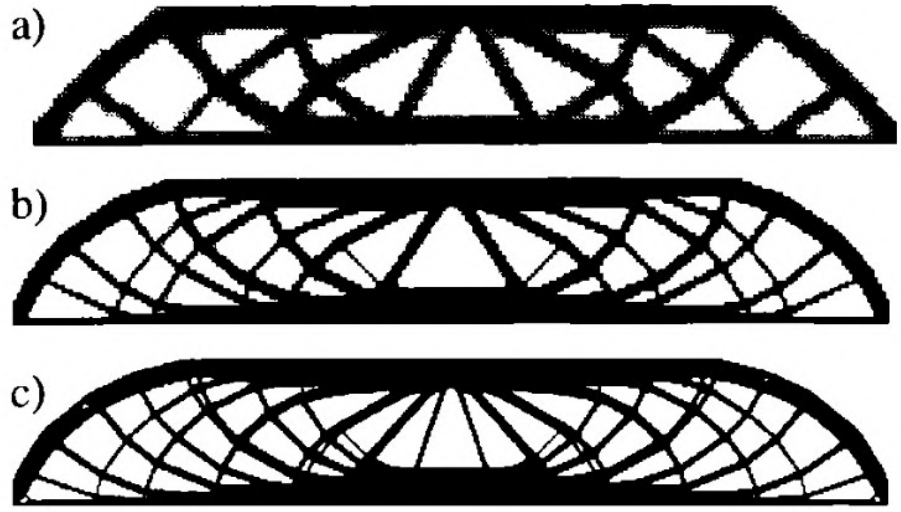

Figure 2.6: Dependence of the optimal topology on mesh refinement for the MBB-beam example. Solution for a discretization with a) 2700, b) 4800 and c) 17200 elements.[4]

ization in the DMO method. As for the mesh-dependence, this problem is also mitigated as the fixed radius of the filter imposes a minimum length scale avoiding the micro-structures seen in Fig. 2.6.

Over the years, several filtering techniques were developed, with various degrees of success. In this work, the density filter used in [37] and developed by Bruns and Tortorelli [38] and Bourdin [39]

[4]Figures taken from M. P. Bendsøe and O. Sigmund. *Topology Optimization: theory, methods and applications*, volume 95. Springer Berlin Heidelberg, Berlin, Heidelberg, 2004. ISBN 978-3-642-07698-5. doi: 10.1007/978-3-662-05086-6

is applied. In discrete material optimization, the density filter works by filtering each unique material candidate across all elements inside the radius of the filtered candidate material. The filtered candidate material variables are thus defined as

$$\tilde{x}_{ec} = \frac{\sum_{i \in \mathbb{N}_e} \mathrm{w}^e(\mathbf{x}_i) V_i x_{ic}}{\sum_{i \in \mathbb{N}_e} \mathrm{w}^e(\mathbf{x}_i) V_i}; \qquad \forall (e, c) \tag{2.33}$$

where $\mathbb{N}_e$ are the elements inside the filter radius, r, relative to the e'th element, V_i is the volume of the i'th element, x_{ic} is the non-filtered design variable relative to the i'th element and unique candidate material c and $\mathrm{w}^e(\mathbf{x}_i)$ is a standard linear decaying weight function defined as

$$\mathrm{w}^e(\mathbf{x}_i) = 1 - \frac{\|\mathbf{x}_i - \mathbf{x}_e\|}{r} \tag{2.34}$$

In (2.34), the term $\|\mathbf{x}_i - \mathbf{x}_e\|$ is the distance between the center points of the i'th and e'th elements based on the Euclidean norm of the vectors containing the coordinates of these points.

After calculating the filtered design variables in (2.33), these are then substituted in the DMO schemes used. As the DMO method relies on gradient based optimization, the influence of the filter used needs to be ascertained for the calculation of the sensitivity analysis. By using the chain rule of differentiation, the sensitivity of the generic function, f, with respect to the design variables, x_{ec}, can be obtained as follows:

$$\frac{\partial f}{\partial x_{ec}} = \sum_{i \in \mathbb{N}_e} \frac{\partial f}{\partial \tilde{x}_{ic}} \frac{\partial \tilde{x}_{ic}}{\partial x_{ec}} \tag{2.35}$$

In (2.35), the function f, could either be the objective function, (2.7), or the constraint function, (2.11). The first part of the chain rule is the sensitivity of the function, f, with respect to the filtered design variables, $\tilde{x}_{ic}$, which was already obtained for the objective function in (2.22) and for the constrain function in (2.25). The final part is the sensitivity of the filtered variables, $\tilde{x}_{ic}$, with respect to the "real" design variables, x_{ec}, which are updated by the optimizer:

$$\frac{\partial \tilde{x}_{ic}}{\partial x_{ec}} = \frac{\mathrm{w}^i(\mathbf{x}_e) V_e}{\sum_{j \in \mathbb{N}_i} \mathrm{w}^i(\mathbf{x}_j) V_j} \tag{2.36}$$

Note that in (2.36), $\mathbb{N}_i$ are the elements inside the density filter radius relative to the i'th element.

2.3.3 Optimizer

When choosing the optimizer for structural topology optimization, several parameters should be considered. The optimizer should be able to deal with a great number of design variables with few constraints, take a minimal amount of time per iteration and be able to converge in a reasonable number of iterations. Although several optimization algorithms have been developed over the years and used in this type of problems, such as Sequential Linear Programming methods (SLP) and Sequential Quadratic Programming methods (SQP), one of the most popular optimizers for structural topology optimization has been the Method of Moving Asymptotes (MMA) [40].

This optimizer has been implemented using the Matlab source code developed and provided by

Professor Krister Svanberg from the Royal Institute of Technology in Stockholm, Sweden.

MMA belongs to a class of optimization methods known as *conservative convex separable approximation* (CCSA) *methods*. The method works by simplifying the original problem using simpler approximate subproblems which are separable and convex, allowing the use of dual methods or interior point algorithms to solve the subproblem and calculate the next iteration point. The method considers the optimization problem as being written in the form

$$\begin{aligned} \text{minimize} \quad & f_0(\mathbf{x}) + a_0 z + \sum_{i=1}^{m} (c_i y_i + \frac{1}{2} d_i y_i^2) \\ \text{subject to} \quad & f_i(\mathbf{x}) - a_i z - y_i \leq 0, \qquad i = 1, \ldots, m \\ & \mathbf{x} \in X, \quad \mathbf{y} \geq \mathbf{0}, \quad z \geq 0 \end{aligned} \tag{2.37}$$

In order to transform (2.37) into the ”standard” non-linear programming form (2.38)

$$\begin{aligned} \text{minimize} \quad & f_0(\mathbf{x}) \\ \text{subject to} \quad & f_i(\mathbf{x}) \leq 0, \qquad i = 1, \ldots, m \\ & \mathbf{x} \in X, \end{aligned} \tag{2.38}$$

and used in (2.17), the recommended values of $a_i = 0$, $d_i = 0$ were used. Since c_i is recommended to be ”a large number”, the value of $c_i = 1000$ was used [40].

2.3.4 Optimization Convergence

To determine convergence of the optimization, an approach similar to the algorithm used by Sørensen and Lund [37] was implemented. The program starts by calculating the relative change of design variables and verifying if this is below a certain established threshold. This relative change of the design variables is calculated as

$$R = \sqrt{\frac{\sum_{i=1}^{N^e} \sum_{c=1}^{n^e} (x_{ic}^{n+1} - x_{ic}^{n})^2}{\sum_{i=1}^{N^e} \sum_{c=1}^{n^e} (\overline{x}_{ic} - \underline{x}_{ic})^2}} \tag{2.39}$$

where n is the number of the current iteration, $\overline{x}_{ic}$ and $\underline{x}_{ic}$ are the upper and lower bounds of the i'th element and c'th discrete material, i.e., 1 and 0, respectively. If R is below the established threshold, which could be for example $R = 0.01$, meaning that if the relative change of the design variables is below 1%, or if the value of the objective function didn't change significantly, the optimization is considered to have converged numerically. This solution could, however, still be unacceptable, or still have room for improvement.

To confirm that the optimization achieved a satisfactory solution, i.e., a single material was selected in all the elements, a DMO convergence measure was implemented from [1]. First, the convergence for each element is measured, by comparing the Euclidean norm of the weight factors for each weight factor, w_i:

$$w_i \geq \epsilon \sqrt{w_1^2 + w_2^2 + \cdots + w_{n^e}^2} \tag{2.40}$$

where ϵ is a tolerance level, with typical values ranging between 95% - 99.5%. If inequality (2.40) is

satisfied, the element is flagged as converged. After analyzing the convergence of all elements, the DMO convergence (also called as the solution discreteness), h_ϵ, can be calculated by dividing the number of converged elements, N_c^e, by the number of total elements, N^e,

$$h_\epsilon = \frac{N_c^e}{N^e} \tag{2.41}$$

with full convergence considered to have been achieved when $h_\epsilon = 1$.

If the DMO convergence is above an imposed minimum, the solution is considered satisfactory. However, if the non-discreteness of the solution is deemed unacceptable and the penalization power p is below p_{max}, the optimization is reinitialized with an increased penalization.

Chapter 3

Computational Model

This chapter is dedicated to the implementation of the optimization algorithm in a finite element program. The theory and implementation of the finite element method is presented together with the finite elements used in the program. Later in the chapter, some case studies are introduced and analyzed: the MBB problem and a 3 point tensile problem.

3.1 Finite Element Analysis

In the last chapter, the objective function was defined as the minimization of the compliance of the structure, which was defined for the linear case in (2.7) but is stated here again for reference:

$$\mathcal{C} = \mathbf{u}^T \mathbf{p} = 2U \tag{3.1}$$

where $\mathbf{p}$ are the applied forces, $\mathbf{u}$ are the displacements at the point of load application and U is the total strain energy. In order to calculate the displacement of a structure with multiple degrees of freedom subject to a static load, one of the most used methods is the finite element method.

The finite element analysis is a powerful numerical method used to simulate and solve many real-world problems such as heat conduction, structural behavior and fluid mechanics, by dividing a given domain into several, smaller subdomains, which then have their governing differential equations solved using a collection of simple polynomials.

The finite element method begins by dividing the geometrically complex domain of the problem into a series of geometrically simple subdomains called *finite elements*. This is designated as *mesh generation*. These *finite elements* are defined by points called *nodes* and a *mesh* can be composed by different types of elements, with the same number of nodes or not. Then, over each *finite element*, "algebraic equations of among the quantities of interest are developed using the governing equations of the problem" [34, p. 13]. After developing these equations for all the *finite elements*, these are then assembled altogether to obtain the algebraic equations that characterize the total problem. Finally, after the application of the boundary conditions, such as loads, displacements, etc, the solution of the equations can

be found, which should then be post-processed for the quantities of interest. More information about the finite element method can be found in [34].

In this work only linear elastic problems were considered, which is common in various topology optimization routines. In this case, the stress-strain relation is considered to be linear, as seen in (2.1), and the displacements are assumed to be small. The linear relation between stress and strain results in a linear behavior between the applied forces and the resulting displacement of the structure. The solution of the finite element method in a problem of linear elasticity is the approximate nodal displacements of a structure given a set of applied boundary conditions, i.e, fixed displacements and applied loads.

In the case of plane stress in the x-y plane, the stress components are assumed to only have contributions in the xx, yy and xy components, while all the -z components are assumed to have value of zero. This means that the only displacements that will be influenced are the ones in the horizontal (u_x) and vertical (u_y) directions.

The approximate solution of these displacements can be determined as a linear combination of nodal displacements u_x^i and u_y^i and approximation functions known as *shape functions* $\psi_i^e(x, y)$:

$$u_x \approx \sum_{i=1}^{n} u_x^i \psi_i^e(x, y), \qquad u_y \approx \sum_{i=1}^{n} u_y^i \psi_i^e(x, y) \tag{3.2}$$

where i corresponds to the i'th node of element e and n is the total number of nodes of said element.

These shape functions are expressed as polynomial functions with certain properties. The first property in known as *interpolation property* in which the value of ψ_i^e is unity at the i'th node and zero at every other node. The other property is known as the *partition of unity* where the sum of the shape functions of a given element is unity. These properties are summarized in equation (3.3) [34]

$$\begin{aligned} &\psi_i^e(x_j^e, y_j^e) = \begin{cases} 0 \;\; if \;\; i \neq j \\ 1 \;\; if \;\; i = j \end{cases} \\ &\textstyle\sum_{i=1}^{n} \psi_i^e(x, y) = 1 \end{aligned} \tag{3.3}$$

The development of the finite element model is provided in [34]. For the linear static equilibrium problem, this is defined as:

$$\mathbf{K}^e \mathbf{u}^e = \mathbf{p}^e \tag{3.4}$$

where $\mathbf{K}^e$ is the element stiffness matrix, already defined in (2.10), but stated here again for reference:

$$\mathbf{K}^e = \int_{V^e} \mathbf{B}^T \mathbf{C} \mathbf{B} \, dV \tag{3.5}$$

In chapter 2, the constitutive matrix $\mathbf{C}$ was introduced along with the transformation matrix $\mathbf{T}(\theta)$ for a generic tridimensional case. However, for plane stress in the x-y plane, as was already mentioned, the -z stress components are assumed to have value zero which allows us to simplify both matrices by eliminating the terms, lines and columns associated with these components. In the case of orthotropic

materials, the constitutive matrix $\mathbf{C}$ in (2.3) is written as:

$$\mathbf{C} = \begin{bmatrix} \frac{E_1}{1-\nu_{12}\nu_{21}} & \frac{\nu_{12}E_2}{1-\nu_{12}\nu_{21}} & 0 \\ \frac{\nu_{21}E_1}{1-\nu_{12}\nu_{21}} & \frac{E_2}{1-\nu_{12}\nu_{21}} & 0 \\ 0 & 0 & G_{12} \end{bmatrix} \tag{3.6}$$

(Note that for isotropic materials the constitutive matrix $\mathbf{C}$ in (3.6) has $E_1 = E_2$ and $\nu_{12} = \nu_{21}$)

The transformation matrix $\mathbf{T}(\theta)$ in (2.6) is written as:

$$\mathbf{T}(\theta) = \begin{bmatrix} \cos^2\theta & \sin^2\theta & -2\cos\theta\sin\theta \\ \sin^2\theta & \cos^2\theta & 2\cos\theta\sin\theta \\ \cos\theta\sin\theta & -\cos\theta\sin\theta & \cos^2\theta - \sin^2\theta \end{bmatrix} \tag{3.7}$$

By combining matrices (3.6) and (3.7) similarly as in Eq. (2.5), we obtain the transformed constitutive matrix $\bar{\mathbf{C}}$:

$$\bar{\mathbf{C}} = \mathbf{T}(\theta)\,\mathbf{C}\,\mathbf{T}(\theta)^T \tag{3.8}$$

which is then substituted in (2.14) for each orthotropic material candidate.

The strain-displacement matrix $\mathbf{B}$ in Eq. (3.5) is calculated from the partial derivatives of the shape functions ψ as:

$$\mathbf{B} = \mathbf{D}^T\boldsymbol{\psi} = \begin{bmatrix} \frac{\partial\psi_1}{\partial x} & 0 & \frac{\partial\psi_2}{\partial x} & 0 & \dots & \frac{\partial\psi_n}{\partial x} & 0 \\ 0 & \frac{\partial\psi_1}{\partial y} & 0 & \frac{\partial\psi_2}{\partial y} & \dots & 0 & \frac{\partial\psi_n}{\partial y} \\ \frac{\partial\psi_1}{\partial y} & \frac{\partial\psi_1}{\partial x} & \frac{\partial\psi_2}{\partial y} & \frac{\partial\psi_2}{\partial x} & \dots & \frac{\partial\psi_n}{\partial y} & \frac{\partial\psi_n}{\partial x} \end{bmatrix} \tag{3.9}$$

$$\mathbf{D} = \begin{bmatrix} \frac{\partial}{\partial x} & 0 & \frac{\partial}{\partial y} \\ 0 & \frac{\partial}{\partial y} & \frac{\partial}{\partial x} \end{bmatrix}$$

Finally, the element stiffness matrix $\mathbf{K}^e$ in (3.5) can be expressed for a bidimensional element composed of an orthotropic material as:

$$\mathbf{K}^e = \int_{A^e} h\,\mathbf{B}^T\bar{\mathbf{C}}\mathbf{B}\,dA \tag{3.10}$$

where h is the thickness of the structure in the z direction and A^e is the area of the element. All that is left to do is sum over all elements the equations in (3.4), making sure to correspond the local nodes of each element with the corresponding global nodes of the mesh and solve the linear static equilibrium equations

$$\mathbf{K}\mathbf{u} = \mathbf{p} \tag{3.11}$$

thus obtaining the vector of global displacements $\mathbf{u}$.

However, when using irregular elements in a mesh such as quadrilateral elements, its easier to evaluate the integral in (3.10) over a rectangular geometry and as such, a transformation of the finite element equations from a quadrilateral to a rectangular element is performed. This normally results in complicated algebraic integral expressions hard to calculate analytically. Therefore, these are often evaluated using numerical integration methods such as the Gauss quadrature method [33, 34].

In the Gauss quadrature method, the integral of element Ω_e with coordinate system (x, y) must be expressed over region $\hat{\Omega}$ with coordinate system (ξ, η) to be such that $-1 \leq (\xi, \eta) \leq 1$. This transformation from element Ω_e to *master element* $\hat{\Omega}$ (or vice-versa) is performed by a transformation of the form

$$\mathbf{x} = \sum_{i=1}^{m} x_i^e \hat{\psi}_i^e(\xi, \eta), \qquad \mathbf{y} = \sum_{i=1}^{m} y_i^e \hat{\psi}_i^e(\xi, \eta) \tag{3.12}$$

where $\hat{\psi}_i^e$ are the shape functions of master element $\hat{\Omega}$.

This transformation from global (x, y) to local (ξ, η) coordinates will involve for the strain-displacement matrix $\mathbf{B}$ in (3.9) to be expressed in this new coordinate system by means of Eq. (3.12). By the chain rule of partial differentiation, we have [34]

$$\begin{aligned} \frac{\partial \psi_i^e}{\partial \xi} &= \frac{\partial \psi_i^e}{\partial x}\frac{\partial x}{\partial \xi} + \frac{\partial \psi_i^e}{\partial y}\frac{\partial y}{\partial \xi} \\ \frac{\partial \psi_i^e}{\partial \eta} &= \frac{\partial \psi_i^e}{\partial x}\frac{\partial x}{\partial \eta} + \frac{\partial \psi_i^e}{\partial y}\frac{\partial y}{\partial \eta} \end{aligned} \tag{3.13}$$

which in matrix notation becomes

$$\begin{Bmatrix} \dfrac{\partial \psi_i^e}{\partial \xi} \\ \dfrac{\partial \psi_i^e}{\partial \eta} \end{Bmatrix} = \begin{bmatrix} \dfrac{\partial x}{\partial \xi} & \dfrac{\partial y}{\partial \xi} \\ \dfrac{\partial x}{\partial \eta} & \dfrac{\partial y}{\partial \eta} \end{bmatrix} \begin{Bmatrix} \dfrac{\partial \psi_i^e}{\partial x} \\ \dfrac{\partial \psi_i^e}{\partial y} \end{Bmatrix} \equiv \mathbf{J} \begin{Bmatrix} \dfrac{\partial \psi_i^e}{\partial x} \\ \dfrac{\partial \psi_i^e}{\partial y} \end{Bmatrix} \tag{3.14}$$

where $\mathbf{J}$ is known as the *Jacobian matrix* of the transformation in (3.12).

In (3.14), the relation between the derivatives of ψ_i^e with respect to the global and local coordinates is established. From (3.12) we notice that what is required is the inverse relation to then substitute in the $\mathbf{B}$ matrix (3.9). Therefore, Eq. (3.14) must be inverted:

$$\begin{Bmatrix} \dfrac{\partial \psi_i^e}{\partial x} \\ \dfrac{\partial \psi_i^e}{\partial y} \end{Bmatrix} = \mathbf{J}^{-1} \begin{Bmatrix} \dfrac{\partial \psi_i^e}{\partial \xi} \\ \dfrac{\partial \psi_i^e}{\partial \eta} \end{Bmatrix} \tag{3.15}$$

The development of the Jacobian matrix $\mathbf{J}$ in (3.14) can be written by direct application of (3.12), which gives us:

$$\begin{aligned} \mathbf{J} &= \begin{bmatrix} \frac{\partial x}{\partial \xi} & \frac{\partial y}{\partial \xi} \\ \frac{\partial x}{\partial \eta} & \frac{\partial y}{\partial \eta} \end{bmatrix} = \begin{bmatrix} \sum_{i=1}^{m} x_i \frac{\partial \hat{\psi}_i^e}{\partial \xi} & \sum_{i=1}^{m} y_i \frac{\partial \hat{\psi}_i^e}{\partial \xi} \\ \sum_{i=1}^{m} x_i \frac{\partial \hat{\psi}_i^e}{\partial \eta} & \sum_{i=1}^{m} y_i \frac{\partial \hat{\psi}_i^e}{\partial \eta} \end{bmatrix} \\ &= \begin{bmatrix} \frac{\partial \hat{\psi}_1^e}{\partial \xi} & \frac{\partial \hat{\psi}_2^e}{\partial \xi} & \cdots & \frac{\partial \hat{\psi}_m^e}{\partial \xi} \\ \frac{\partial \hat{\psi}_1^e}{\partial \eta} & \frac{\partial \hat{\psi}_2^e}{\partial \eta} & \cdots & \frac{\partial \hat{\psi}_m^e}{\partial \eta} \end{bmatrix} \begin{bmatrix} x_1 & y_1 \\ x_2 & y_2 \\ \vdots & \vdots \\ x_m & y_m \end{bmatrix} \end{aligned} \tag{3.16}$$

As noted before, $\hat{\psi}_i^e$ are the interpolation functions of the master element $\hat{\Omega}$. These are generally different from the interpolation functions of the original element Ω_e. However, if the two elements have equal

number of nodes resulting in an equal degree of approximation, then $\hat{\psi}_i^e$ and ψ_i^e are the same, when written in the local coordinate system (ξ, η) and the elements are called *isoparametric elements*.

In order to be able to invert the Jacobian matrix $\mathbf{J}$ in (3.15), this needs to be nonsingular. For a matrix to be considered nonsingular, a necessary and sufficient condition is that its determinant needs to be nonzero. For the Jacobian matrix $\mathbf{J}$, this determinant is called the Jacobian $\mathcal{J}$ and can be stated as:

$$\mathcal{J} \equiv \det[J] = \frac{\partial x}{\partial \xi}\frac{\partial y}{\partial \eta} - \frac{\partial x}{\partial \eta}\frac{\partial y}{\partial \xi} > 0 \tag{3.17}$$

By writing the element area $dA = dx\ dy$ in local coordinates (ξ, η) as

$$dA \equiv dx\ dy \equiv \mathcal{J}\ d\xi\ d\eta \tag{3.18}$$

and substituting (3.15) in (3.9) and (3.18) in (3.10), we can now write the elemental stiffness matrix, $\mathbf{K}^e$, in local coordinates (ξ, η) as

$$\mathbf{K}^e = \int_{-1}^{1}\int_{-1}^{1} h\,\mathbf{B}(\xi,\eta)^T \bar{\mathbf{C}}\mathbf{B}(\xi,\eta)\ \mathcal{J}\ d\xi\ d\eta \equiv \int_{\hat{\Omega}} F(\xi,\eta)d\xi d\eta \tag{3.19}$$

As stated earlier, the calculation of the integral in (3.19) results in complicated algebraic expressions. By using numerical quadrature formulas such as the Gauss quadrature, the resulting expression is much simpler to deal with. As such, we obtain [34]:

$$\int_{\hat{\Omega}} F(\xi,\eta)d\xi d\eta \approx \sum_{I=1}^{M}\sum_{J=1}^{N} F(\xi_I,\eta_J)W_I W_J \tag{3.20}$$

where M and N correspond to the number of quadrature points in the ξ and η directions, (ξ_I, η_J) correspond to the Gauss points and W_I and W_J are the corresponding Gauss weights. For a polynomial of degree p to be integrated exactly, the number of Gauss points used most be greater than $\frac{1}{2}(p+1)$.

3.1.1 Integration of linear master finite elements

These are the simplest and least computationally expensive finite elements, being generally used in topology optimization. The use of both quadrilateral and triangular elements can accurately represent the geometry of an irregular domain, without as much element distortion as using solely quadrilateral elements with the same size.

3.1.1.1 Linear Master Rectangular Element

The polynomial associated with this element is a 2^{nd} degree polynomial and is given by

$$\mathbf{u}(x,y) = \mathbf{a_1} + \mathbf{a_2}x + \mathbf{a_3}y + \mathbf{a_4}xy \tag{3.21}$$

By applying the interpolation functions properties in (3.3) to the nodes associated with the linear rectangular element in Fig. 3.1(a), we can develop its interpolation functions, as seen in Fig. 3.1(b), written in

the local coordinate system (ξ, η).

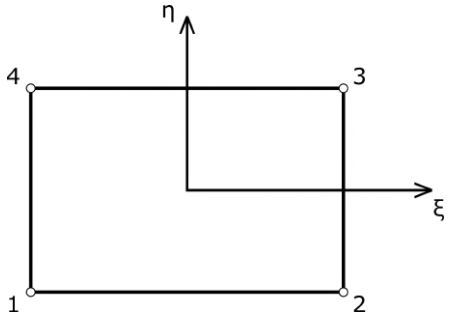

(a)

$$\hat{\psi}_1 = \frac{1}{4}(1-\xi)(1-\eta)$$
$$\hat{\psi}_2 = \frac{1}{4}(1+\xi)(1-\eta)$$
$$\hat{\psi}_3 = \frac{1}{4}(1+\xi)(1+\eta)$$
$$\hat{\psi}_4 = \frac{1}{4}(1-\xi)(1+\eta)$$

(b)

Figure 3.1: Node numbering and shape functions for the linear rectangular element

The integration points and respective weight values used to evaluate the function in (3.20) for the rectangular finite element for multiple degrees of accuracy are summarized in Table 3.1, adapted from [34].

Table 3.1: Weights and points for the Gauss quadrature in one coordinate direction

N or M	Points ξ_I or η_J	Weights W_I or W_J
1	0	2
2	$-\sqrt{\frac{1}{3}}, \sqrt{\frac{1}{3}}$	1, 1
3	$-\sqrt{\frac{3}{5}}$, 0, $\sqrt{\frac{3}{5}}$	$\frac{5}{9}, \frac{8}{9}, \frac{5}{9}$

The linear rectangular finite element has a maximum polynomial degree of $p = 2$. The number of Gauss points necessary to accurately evaluate the integrals most be greater than $N = \frac{1}{2}(p+1) = \frac{3}{2}$, which means that a minimum of two Gauss points will be required for each of the coordinate directions (ξ, η), bringing the total of Gauss points to four. A representation of the Gauss points location for the constant, linear and quadratic quadrilateral finite element can be seen in Fig. 3.2.

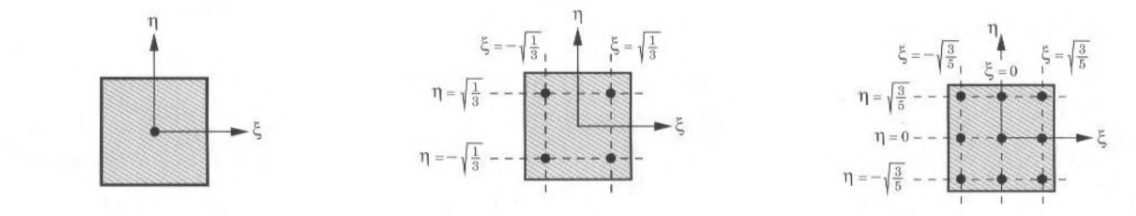

(a) Constant element (b) Linear element (c) Quadratic element

Figure 3.2: Location of Gauss points for the constant, linear and quadratic quadrilateral elements [5]

[5] Figures taken from J. N. Reddy. *An introduction to the finite element method.* McGraw-Hill, 3rd edition, 2006. ISBN 0072466855

3.1.1.2 Linear Master Triangular Element

The polynomial associated with this element is a 1^{st} degree polynomial, given by

$$\mathbf{u}(x,y) = \mathbf{a_1} + \mathbf{a_2}x + \mathbf{a_3}y \tag{3.22}$$

By applying the interpolation functions properties in (3.3) to the nodes associated with the linear triangular element in Fig. 3.3(a), we can develop its interpolation functions, as seen in Fig. 3.3(b), written in the local coordinate system (ξ, η).

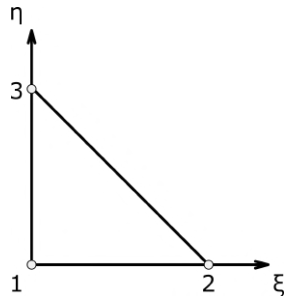

(a)

$$\hat{\psi}_1 = L_1 = 1 - \xi - \eta$$
$$\hat{\psi}_2 = L_2 = \xi$$
$$\hat{\psi}_3 = L_3 = \eta$$

(b)

Figure 3.3: Node numbering and shape functions for the linear triangular element

For the linear triangular element, these interpolation functions $\hat{\psi}_i$ are equivalent to the area coordinates $L_i (i = 1, 2, 3)$ which are three nondimensionalized coordinates that "relate respectively to the sides directly opposite nodes 1, 2 and 3 such that (see Fig. 3.4)

$$L_i = \frac{A_i}{A} \qquad A = \sum_{i=1}^{3} A_i \tag{3.23}$$

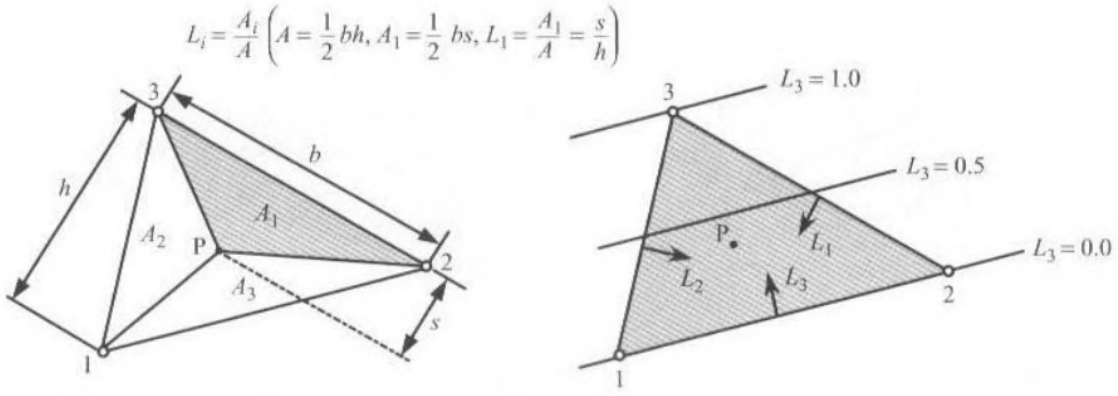

Figure 3.4: Definition of the natural coordinates of a triangular element [6]

where A_i is the area of the triangle formed by nodes j and k and an arbitrary point P in the element, and A is the total area of the element" [34, p. 528]. The interpolation functions for higher-order triangular

[6] Figure taken from J. N. Reddy. *An introduction to the finite element method.* McGraw-Hill, 3rd edition, 2006. ISBN 0072466855

elements can be easily constructed with the use of these area coordinates L_i.

From Eq. (3.23) we can write that $\sum L_i = 1$ and so we can treat L_1 and L_2 as linearly independent coordinates, since $L_3 = 1 - L_1 - L_2$. After transformation from the local coordinates (ξ, η) to the area coordinates (L_1, L_2), we can write Eq. (3.15) as

$$\begin{aligned} \frac{\partial \psi_i}{\partial x} &= \frac{\partial \psi_i}{\partial L_1}\frac{\partial L_1}{\partial x} + \frac{\partial \psi_i}{\partial L_2}\frac{\partial L_2}{\partial x} \\ \frac{\partial \psi_i}{\partial y} &= \frac{\partial \psi_i}{\partial L_1}\frac{\partial L_1}{\partial y} + \frac{\partial \psi_i}{\partial L_2}\frac{\partial L_2}{\partial y} \end{aligned} \tag{3.24}$$

or

$$\begin{Bmatrix} \frac{\partial \psi_i}{\partial x} \\ \frac{\partial \psi_i}{\partial y} \end{Bmatrix} = \mathbf{J}^{-1} \begin{Bmatrix} \frac{\partial \psi_i}{\partial L_1} \\ \frac{\partial \psi_i}{\partial L_2} \end{Bmatrix}, \qquad \mathbf{J} = \begin{bmatrix} \frac{\partial x}{\partial L_1} & \frac{\partial y}{\partial L_1} \\ \frac{\partial x}{\partial L_2} & \frac{\partial y}{\partial L_2} \end{bmatrix} \tag{3.25}$$

which leads us to a similar expression as Eq. (3.20) with the form

$$\int_{\hat{\Omega}} G(\xi, \eta) d\xi d\eta = \int_{\hat{\Omega}} \hat{G}(L_1, L_2, L_3) dL_1 d_2 \approx \frac{1}{2} \sum_{i=1}^{N} \hat{G}(S_I) W_I \tag{3.26}$$

where W_I and S_I are the weight and integration points of the quadrature rule which are summarized in Table 3.2 for one- and three-point quadrature rules over triangular elements. Fig. 3.5 shows the location of the integration points.

Table 3.2: Quadrature points and weights for triangular elements

Number of integration points	Integration points and weights				Nodes
	L_1	L_2	L_3	W	
1	$\frac{1}{3}$	$\frac{1}{3}$	$\frac{1}{3}$	1	a
3	$\frac{1}{2}$	0	$\frac{1}{2}$	$\frac{1}{3}$	a
	$\frac{1}{2}$	$\frac{1}{2}$	0	$\frac{1}{3}$	b
	0	$\frac{1}{2}$	$\frac{1}{2}$	$\frac{1}{3}$	c

(a) (b)

Figure 3.5: Quadrature points location for triangular elements with a) 1 integration point, b) 3 integration points [7]

3.2 Implementation of the Discrete Material Optimization Program

In order to be able to implement in a flexible way the DMO method discussed in chapter 2 into a finite element program, a custom MATLAB program was developed. The algorithm starts by reading a .dat file generated in the commercial finite element software Siemens NX. This file contains the pre-processed information such as nodes, elements, elemental connectivity matrix and boundary conditions of the design problem. The program then proceeds to initiate the optimization routine by computing the finite element analysis and sensitivity analysis whose results are used to calculate the compliance and design gradients. These are then used by the MMA algorithm to generate new design variables with each iteration of the optimization until an optimal design is attained, at which point, the program will then display the final results along with the optimal structure. A schematic of the general structure of the computer algorithm can be seen in Fig. 3.6:

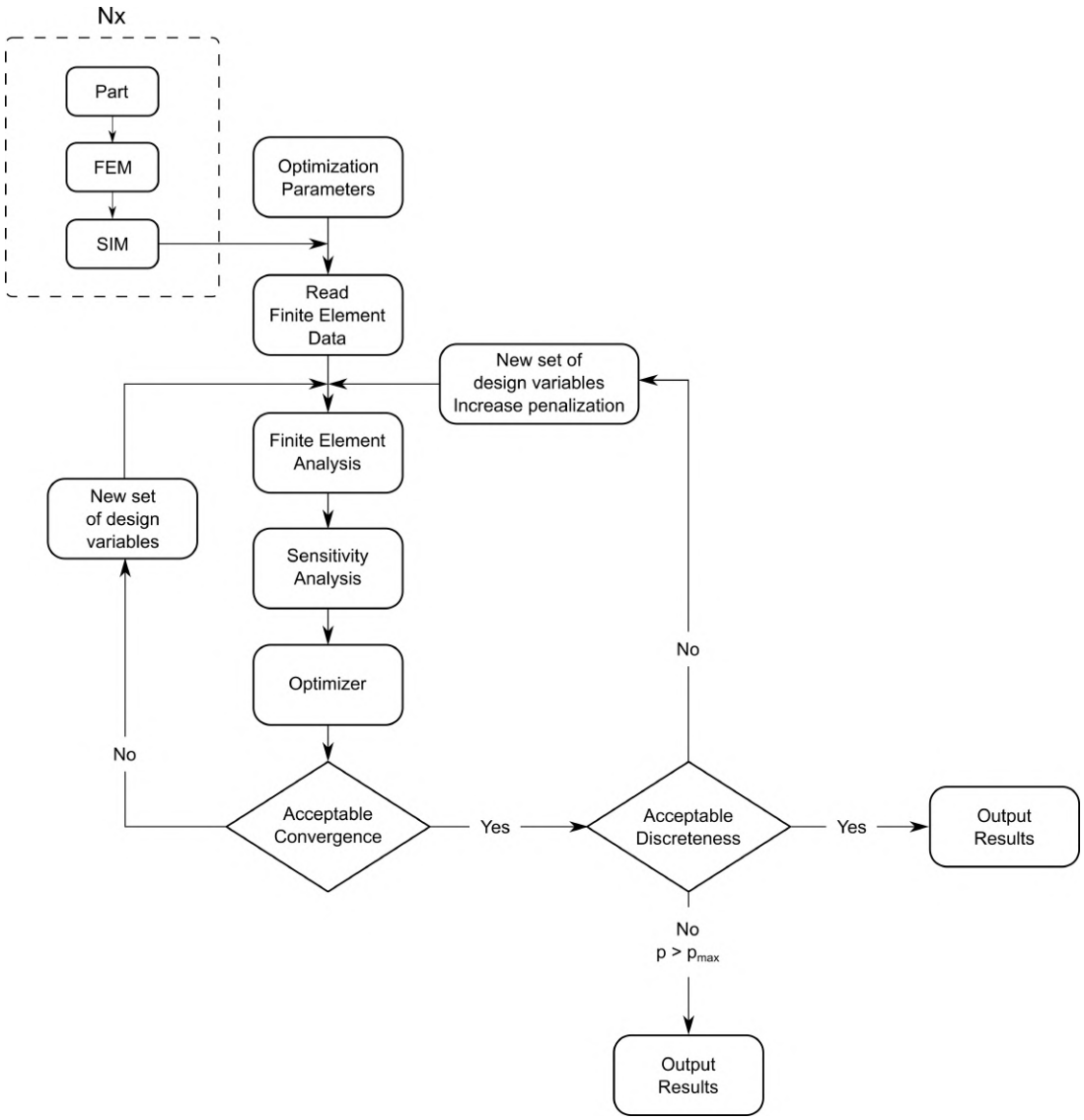

Figure 3.6: Flowchart of the developed Matlab algorithm

[7] Figures taken from J. N. Reddy. *An introduction to the finite element method.* McGraw-Hill, 3rd edition, 2006. ISBN 0072466855

3.2.1 Computational Results

Next, a series of material distribution and fiber angle optimizations will be presented using the Discrete Material Optimization (DMO) method. These optimizations will focus on the so-called Messerschimitt-Bölkow-Blohm (MBB) beam, first introduced by Olhoff et al. [41] and in a three-point tensile example. The goal of these optimizations will be to understand the influence of certain parameters in the final structure. In the first example, material properties and mesh-dependence will be studied and in the latter, the study will be focused on the volume fraction and its effects in the final compliance. In the optimization results, the presence of fiber material is represented by a darker element with a dash symbolizing the material orientation, while the solid, lighter elements represent void material. Black and white elements represent converged elements, while an intermediate, gray color represents unconverged elements. All the computations were performed on a laptop with an Intel i7-7700HQ CPU and 16 GB of RAM.

3.2.1.1 MBB Beam Optimization

The MBB beam has become a standard topology optimization problem, used as a benchmark for various optimizations methods. A modified model of the MBB beam can be seen in Fig. 3.7. The dimensions of the beam are 180 $\times$ 40 [mm] with a total thickness of 1 mm. The beam is supported on the bottom edge at two symmetrically placed points, 10 mm inwards from the lateral edges, fixing the vertical displacement at those points. A single 1 Newton downward load is applied at the top center of the structure.

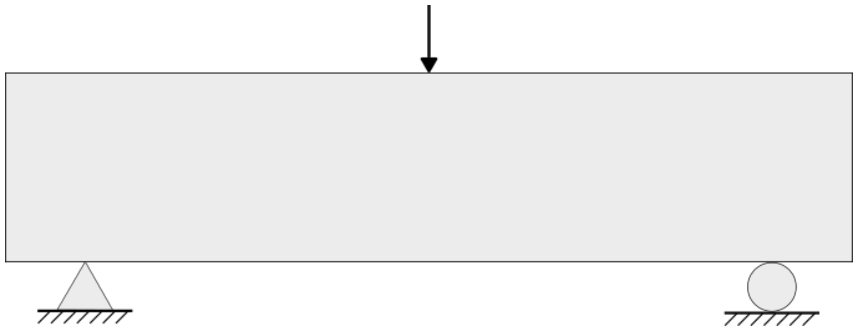

Figure 3.7: Loading conditions and geometry of the MBB beam

Young's Modulus ratio's influence in the MBB Beam optimization

To understand the influence of the Young's Modulus ratio on the results of the MBB beam optimization problem, when using the DMO method, a series of optimizations were run using different ratios by altering the value of the Young's Modulus for direction 2, i.e, E_2. A similar study was performed by Hoglund [17] using the CFAO method, for which there were no observable differences in the final structures using different ratios.

Since both the structure and boundary conditions share one axis of symmetry, the optimizations were performed on one half of the structure, as seen in Fig. 3.8, using the appropriate symmetry conditions. This allows for the use of smaller finite elements without increasing the computation time, leading to a

better resolution of the complete structure.

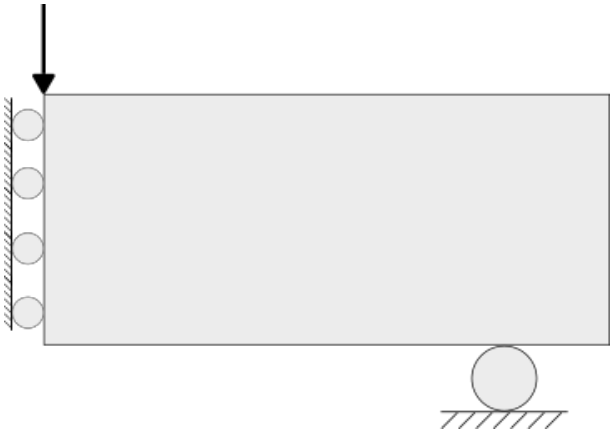

Figure 3.8: Loading and boundary conditions for one half of the MBB beam

The beam was modeled using a regular mesh of 90 by 40 rectangular elements, resulting in a total of 3600 elements. The orthotropic material properties used were $E_1 = 10$ MPa, $G_{12} = 0.4$ MPa and $\nu_{12} = 0.25$ with 8 possible orientations [$90°$, $\pm 67.5°$, $\pm 45°$, $\pm 22.5°$, $0°$], while the void material properties are $E = 0.001$ MPa and $\nu = 0.4$. The volume fraction was set at $f = 0.5$ and a filter radius of $r = 1.4$ mm was used to prevent checkerboarding and define the minimal frame thickness of the structure. The starting penalization was set as $p = 3$, increasing by 4 up to a maximum of $p = 23$, if the convergence requirements of a minimum of 95% converged elements weren't met. These requirements were tested when the relative change of the design values was below $R = 0.005 = 0.5\%$ or the change in compliance was below 0.001%. In table 3.3 the results of the optimizations have been summarized, where the compliance and volume fraction are computed for a totally converged structure, by setting the highest design variable for each element to 1 and the rest to 0.

Table 3.3: MBB test results by varying Young's Modulus ratio

Young's Modulus [$E_1 : E_2$]	Ratio	Number of iterations	Total Time [s]	Final Compliance [N.m] $\times 10^{-3}$	Volume Fraction	Convergence [%]
10 MPa : 10 MPa	1:1	111	750	7.255	0.487	0.958
10 MPa : 5 MPa	2:1	108	3187	7.959	0.485	0.946
10 MPa : 2.5 MPa	4:1	120	2645	7.983	0.486	0.945
10 MPa : 1.667 MPa	6:1	132	3005	9.183	0.481	0.934
10 MPa : 1.25 MPa	8:1	142	3292	9.763	0.481	0.936
10 MPa : 1 MPa	10:1	123	3856	10.131	0.478	0.923

In the 1:1 ratio optimization, the material was altered to have isotropic properties with $G_{12} = 4$ MPa and the material orientation was set to $0°$ to avoid problems with unconverged fiber elements, since

there wouldn't be a preferred material orientation. For this reason, the resulting isotropic structure is represented only as black and white, as is common in topology optimization results. This explains the discrepancy in the total optimization time, since the 1:1 ratio optimization has a total of 7200 design variables and the rest of the optimizations have a total of 32400 design variables.

The results indicate that, as the orthotropy ratio increases, the volume fraction and the convergence of the solution decreases, revealing a higher difficulty for the optimizer to choose between the materials and orientations. The opposite can be observed for the compliance, which increases with the orthotropy ratio. For the most part, an increase in orthotropy ratio leads to an increase in the number of iterations needed for the optimization to converge. The same could be said about the total computing time, but conclusions can't be drawn since the processor wasn't always completely dedicated to the optimizations.

The structures from the resulting optimizations can be seen in Fig. 3.9. The isotropic 1:1 ratio structure is similar to results obtained using normal topology optimization, acquiring a truss-like design. For the rest of the structures, the optimal material distribution remains approximately the same, with slight variations, independently of the Young's modulus ratio, which agrees with the results obtained by Hoglund [17]. This explains the increase in compliance values for higher degrees of orthotropy, since the decrease of Young's modulus E_2 results in a weaker material, leading to a higher displacement of the structure, for the same force. By observing the insignificant increase in compliance when comparing the 4:1 ratio with the 2:1 ratio structure as opposed to the rest and then comparing the structures, it seems that the extra reinforcement created in the 4:1 optimization creates a stiffer structure while maintaining the mass. This reinforcement can be seen to be developed for increased orthotropic ratios although with little success. In all the orthotropic optimizations, the material orientation is observed to be aligned along the principal stress directions of the structure's frame.

Mesh-dependence study using the DMO method with a density filter

To investigate the influence different mesh sizes have on optimizations performed with the DMO method coupled with a density filter, a study of the MBB beam problem was conducted using the same material properties for different sized meshes.

For this test, the orthotropic material properties were $E_1 = 10$ MPa, $E_2 = 1.667$ MPa, $G_{12} = 0.4$ MPa and $\nu_{12} = 0.25$ with possible orientations $[90^\circ, \pm 67.5^\circ, \pm 45^\circ, \pm 22.5^\circ, 0^\circ]$, while the void material remained the same with $E = 0.001$ MPa and $\nu = 0.4$. The volume fraction and filter radius were, respectively, $f = 0.5$ and $r = 1.4$ mm. The same optimization parameters of the previous test were used. Results for the varying mesh sizes can be seen in table 3.4 with the resulting material distribution and orientations shown in Fig. 3.10.

The mesh-independent density filter was successful in preventing mesh-dependency for the different mesh sizes as the resulting structures have similar material distribution. The results for the mesh of 45 by 20 elements show a slightly different material distribution, with extra frames appearing in the middle, and the appearance of the checkerboard effect, since the element size is approximately the same as the filter diameter. The reinforcement noticed in the previous study is also present in two of the optimization

(a) Results for a 1:1 ratio of Young's modulus

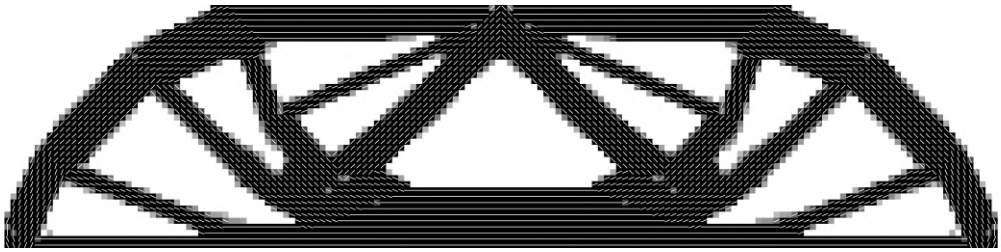

(b) Results for a 2:1 ratio of Young's modulus

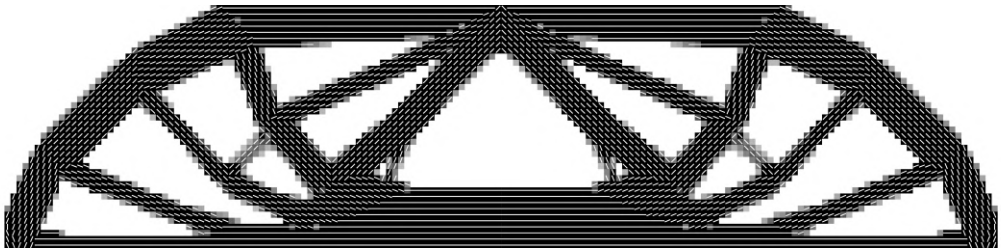

(c) Results for a 4:1 ratio of Young's modulus

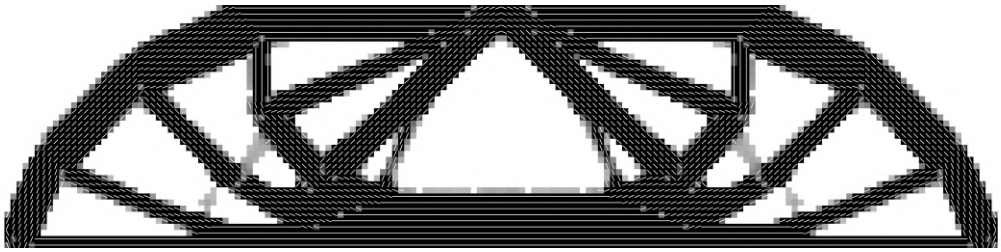

(d) Results for a 6:1 ratio of Young's modulus

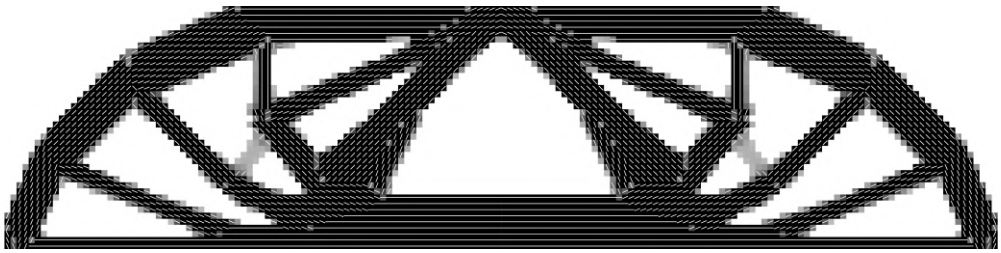

(e) Results for a 8:1 ratio of Young's modulus

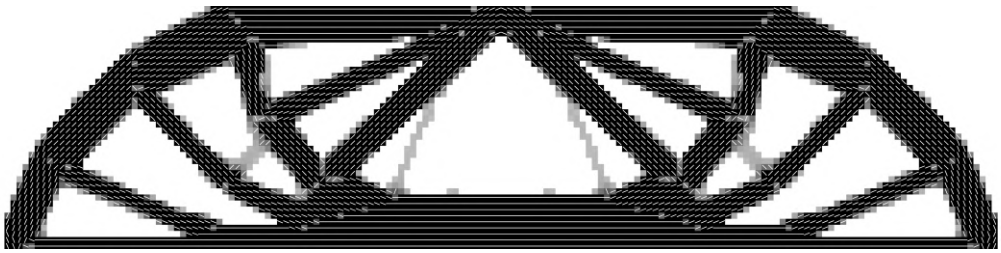

(f) Results for a 10:1 ratio of Young's modulus

Figure 3.9: Results for the MBB beam optimization problem using the DMO method for different ratios of Young's modulus

Table 3.4: MBB test results for different finite element mesh sizes

Mesh sizes	Number of iterations	Total Time [s]	Final Compliance [N.m] $\times 10^{-3}$	Volume Fraction	Convergence [%]
45 by 20	84	255	9.247	0.471	0.956
72 by 32	220	3566	10.262	0.469	0.938
90 by 40	132	3005	9.183	0.481	0.934
144 by 64	102	17855	8.570	0.488	0.938

results, although the presence of unconverged elements in the area indicate the optimizer's difficulty to decide if the reinforcement must be there or not.

As the mesh size increases, the number of necessary iterations tend to increase as well as the total computation time which greatly increases. This behavior of the computation time can be explained by the increase of number of design variables with more refined meshes.

Shear modulus influence in the MBB Beam optimization

For this study, the effect of the shear modulus G_{12} in the material distribution and orientation in the MBB beam optimization is investigated. The material parameters were maintained throughout the various optimizations with exception of the shear modulus. The materials used were an orthotropic material with $E_1 = 10$ MPa, $E_2 = 2.5$ MPa and $\nu_{12} = 0.25$ with possible orientations $[90^\circ, \pm 67.5^\circ, \pm 45^\circ, \pm 22.5^\circ, 0^\circ]$, as well as an isotropic void material with $E = 0.001$ MPa and $\nu = 0.4$. The same optimization parameters of the previous studies were used. A mesh with 90 by 40 elements was used for the computations. Table 3.5 summarizes the results of this study.

Contrary to the previous study for the Young's modulus, there's no indication of a decrease in compliance as the shear modulus increases. In Fig. 3.11 the material distribution and orientation for the different values of G_{12} are represented. As the value of G_{12} increases, the material distribution becomes increasingly similar to that of the isotropic structure seen in Fig. 3.9(a) until $G_{12} = 2.857$ MPa. For values of $G_{12} > 2.857$ MPa, the orientation of the material begins to not correspond with those of the principal stress directions in the structure's members. The explanation for this behavior can be explained by the values of β in table 3.5. The parameter β relates the various material properties and is used to measure the shear stiffness of the material [36, 42]. It can be stated as:

$$\beta = \frac{E_1}{1 - \nu_{12}\nu_{21}} + \frac{E_2}{1 - \nu_{12}\nu_{21}} - 2\frac{\nu_{12}E_2}{1 - \nu_{12}\nu_{21}} - 4G_{12} \tag{3.27}$$

Most materials are characterized as being weak in shear with $\beta \geq 0$, representing low shear stiffness, with isotropic materials having $\beta = 0$. Materials with high shear stiffness, i.e, $\beta < 0$ can be designed with

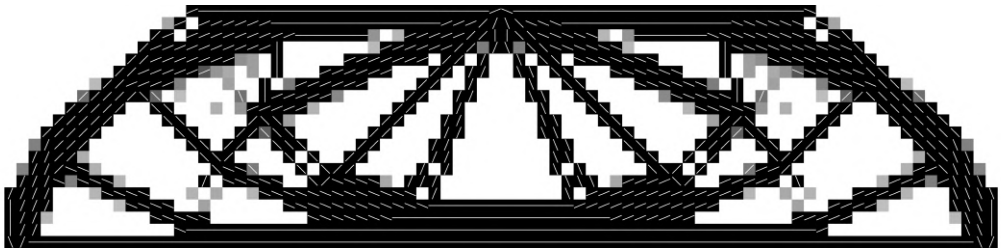

(a) Finite element mesh with 45 by 20 elements

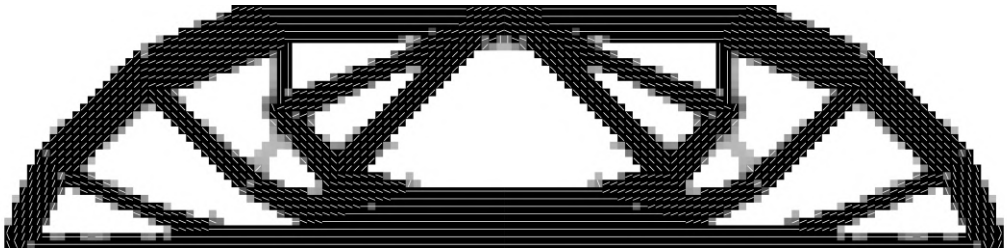

(b) Finite element mesh with 72 by 32 elements

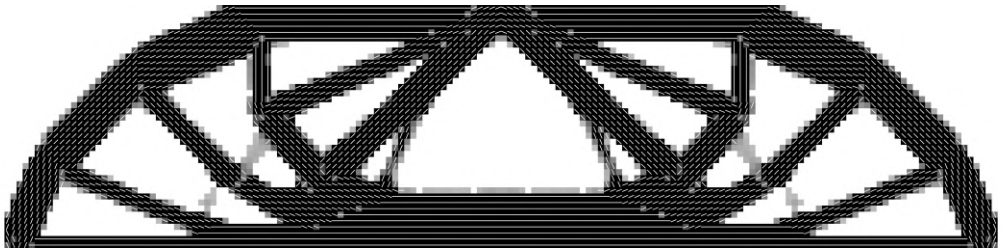

(c) Finite element mesh with 90 by 40 elements

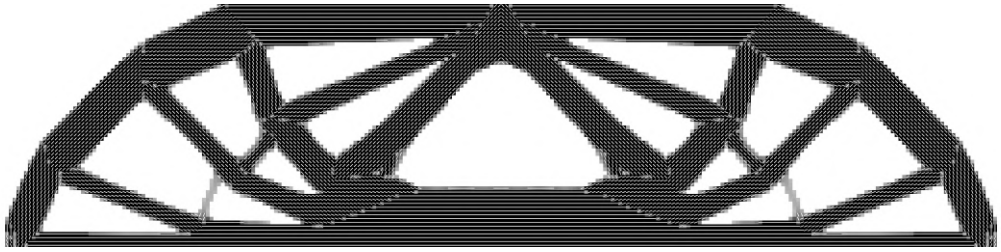

(d) Finite element mesh with 144 by 64 elements

Figure 3.10: Results for the MBB beam optimization problem using the DMO method for different mesh sizes

the use of laminates. This can explain the similar material distribution of Fig. 3.11(f) with $G_{12} = 2.857$ MPa with the one in Fig. 3.9(a) for an isotropic material, as $\beta = 0$ for these materials.

Although these results seem promising, the guarantee of global minimum cannot be assured even when using the DMO method. This can be proven by taking the material with $G_{12} = 4$ MPa and substituting it in the structure seen in Fig. 3.11(a), with $G_{12} = 0.4$ MPa. This results in a compliance of 7.466×10^{-3} N.m, better than the original compliance of 7.805×10^{-3} N.m, for the same volume fraction and the material now oriented with the principal stress directions.

In an attempt to reach an even better optimal solution with material $G_{12} = 4$ MPa, an optimization was performed using the final design values of the optimization result for $G_{12} = 0.4$ MPa as initial design values, using the same optimization parameters as before. The results of this optimization can be seen in table 3.6 and the resulting material distribution and orientation is shown in Fig. 3.12.

Table 3.5: MBB test results by varying Shear Modulus G_{12} value

Shear Modulus [G_{12}]	Number of iterations	Total Time [s]	Final Compliance [N.m] $\times 10^{-3}$	Volume Fraction	Convergence [%]	β
0.4 MPa	120	2645	7.983	0.486	0.945	9.829
0.7 MPa	119	2455	8.240	0.485	0.957	8.627
1 MPa	110	2617	7.891	0.483	0.953	7.429
1.5 MPa	83	1790	8.386	0.473	0.959	5.429
2.5 MPa	80	1865	8.042	0.475	0.967	1.429
2.857 MPa	87	2395	8.087	0.476	0.963	0
3 MPa	116	2791	8.352	0.479	0.951	-0.571
3.5 MPa	102	3036	9.063	0.469	0.957	-2.571
4 MPa	111	3278	7.805	0.484	0.959	-4.571

Table 3.6: MBB beam optimization results for $G_{12} = 4$ MPa using $G_{12} = 0.4$ MPa optimization's final design variables

Number of iterations	Total Time [s]	Final Compliance [N.m] $\times 10^{-3}$	Volume Fraction	Convergence [%]
69	1990	7.284	0.489	0.959

This optimization results in a structure with a lower compliance than the previous structures for the material with $G_{12} = 4$ MPa. In order to understand if this new structure results in a better solution for the material with $G_{12} = 0.4$ MPa, the compliance for this structure was calculated using this material. The resulting compliance was 9.411$\times 10^{-3}$ N.m, higher than the compliance value of 7.983$\times 10^{-3}$ N.m for the original optimization in Fig. 3.11(a).

3.2.1.2 Three-point tensile optimization

The objective for this optimization is to compare material distribution and orientation as well as stiffness of structures with different mass values, when subjected to the same load conditions. The geometry of the initial design domain can be seen in Fig. 3.13. It consists of a rectangle with dimensions 100 $\times$ 85 [mm] with a thickness of 1 mm. It has three centered Ø5 mm holes, two aligned at the bottom situated 80 mm apart and one at the top, 65 mm vertically from the others. A 1 Newton bearing force is applied upwards in the top hole while the remaining holes remain fixed in the horizontal and vertical directions.

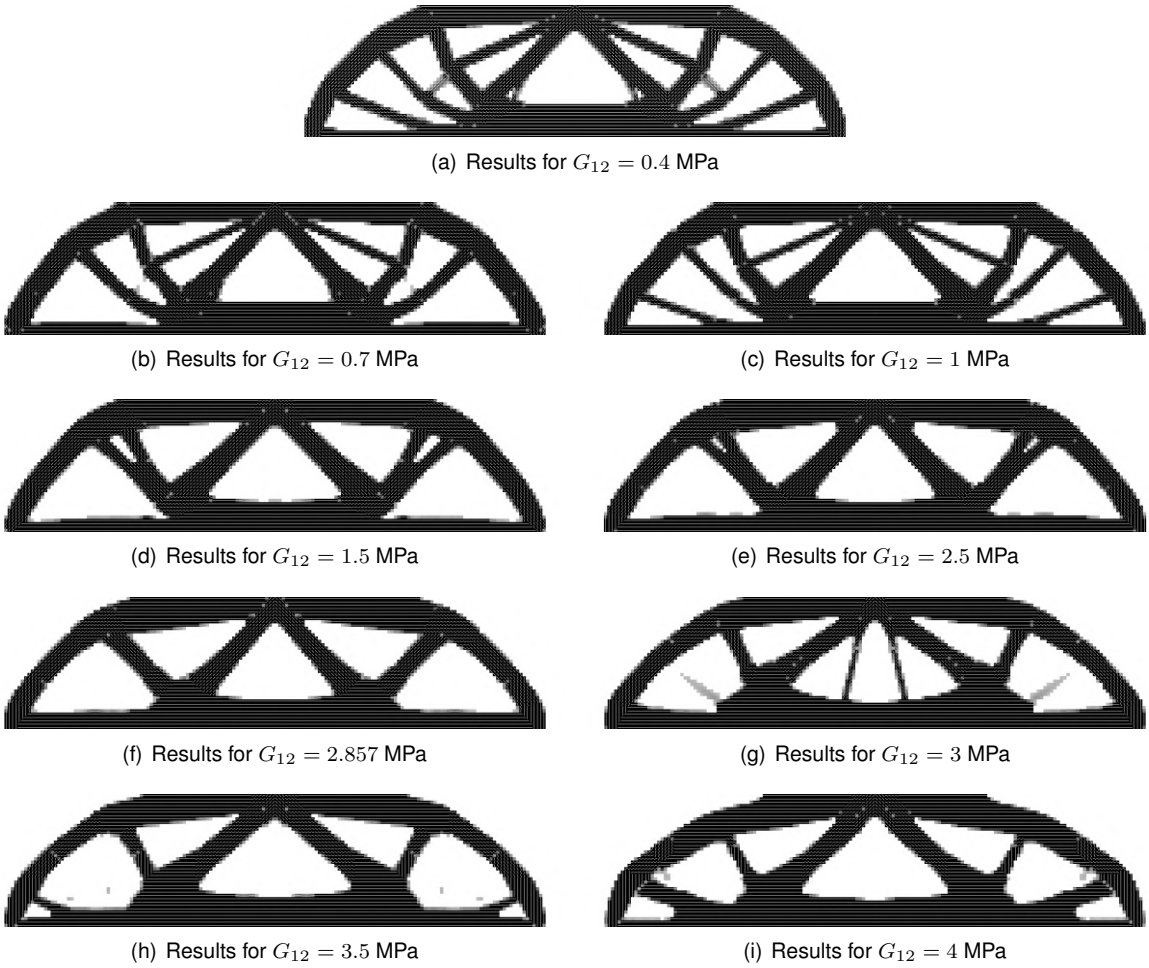

(a) Results for $G_{12} = 0.4$ MPa

(b) Results for $G_{12} = 0.7$ MPa

(c) Results for $G_{12} = 1$ MPa

(d) Results for $G_{12} = 1.5$ MPa

(e) Results for $G_{12} = 2.5$ MPa

(f) Results for $G_{12} = 2.857$ MPa

(g) Results for $G_{12} = 3$ MPa

(h) Results for $G_{12} = 3.5$ MPa

(i) Results for $G_{12} = 4$ MPa

Figure 3.11: Results for the MBB beam optimization problem using the DMO method for different values of shear modulus G_{12}

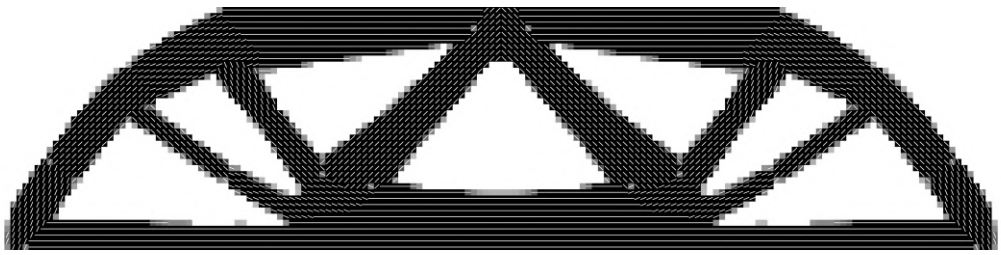

Figure 3.12: MBB beam optimization material distribution and orientation results for $G_{12} = 4$ MPa using $G_{12} = 0.4$ MPa optimization's final design variables

The design domain was meshed using a symmetric matrix with 2202 quadrilateral elements and 94 triangular elements, with a maximum size of 2 mm. The resulting mesh and boundary conditions are shown in Fig. 3.14, with the red arrows representing the applied loads and the blue lines are the fixed nodal displacements.

The candidate materials used are an orthotropic material with $E_1 = 10$ MPa, $E_2 = 2.5$ MPa, $G_{12} = 0.4$ MPa and $\nu_{12} = 0.25$ oriented at $[90^\circ, \pm 67.5^\circ, \pm 45^\circ, \pm 22.5^\circ, 0^\circ]$, as well as an isotropic void material with $E = 0.001$ MPa and $\nu = 0.4$. The optimization parameters used as well as the filter radius of $r = 1.4$ mm remain the same as previous studies. The optimization results are shown in Table 3.7.

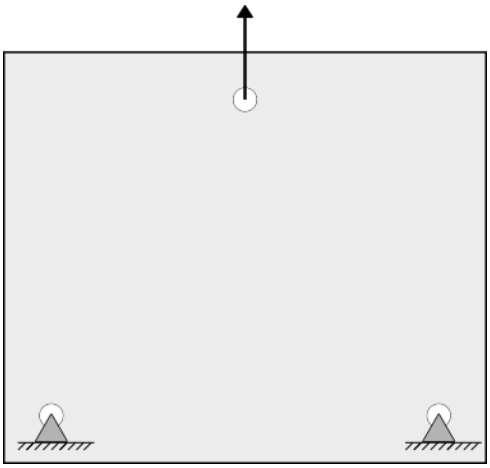

Figure 3.13: Loading conditions and geometry of the three-point tensile problem

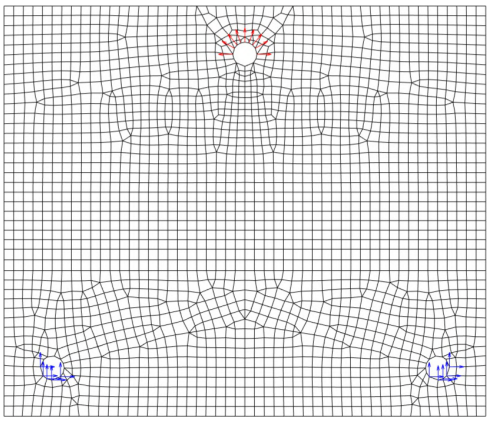

Figure 3.14: Finite element mesh and boundary conditions for the three-point tensile problem

Table 3.7: Three-point tensile optimization results for different volume fractions

f	Number of iterations	Total Time [s]	Final Compliance [N.m] $\times 10^{-3}$	Final Volume Fraction	Convergence [%]	Normalized Compliance [N.m] $\times 10^{-3}$
0.4	56	598	2.368	0.395	0.9874	0.936
0.6	41	477	2.009	0.592	0.9852	1.191
0.8	27	334	1.946	0.794	0.9865	1.547
1	29	331	1.957	0.999	0.9895	1.957

The results indicate that as the volume fraction increases, the compliance of the structure decreases, as expected. However when comparing the compliance values between $f = 0.8$ and $f = 1$, this is not the case. By observing Fig. 3.15, which shows the final material distribution and orientation, the logical conclusion for this result is that the areas with no material in $f = 0.8$ are not subject to significant stress values in the $f = 1$ structure and small variations in the fiber orientation for both structures lead to a smaller compliance value for the $f = 0.8$ structure, when comparing against the $f = 1$ structure.

By multiplying the compliance with the volume fraction of the structure and dividing by the weightiest structure's volume fraction, the normalized compliance can be determined. The results in this case indicate that by decreasing the volume fraction, the normalized compliance decreases as well, resulting in a better stiffness/weight ratio, as expected.

Although the generated finite element mesh is symmetric, leading to the expectation of also symmetric results, examination of the optimization outcome show the contrary, with a few differences in each side of the structures. The problem was found to be caused by rounding differences performed by Matlab when calculating the $\mathbf{K}$ matrix for opposite elements, which when factoring multiple iterations after lead to major differences in values. In this case, this issue is not very significant but for other cases with symmetric structures and boundary conditions, it's better to apply symmetry conditions.

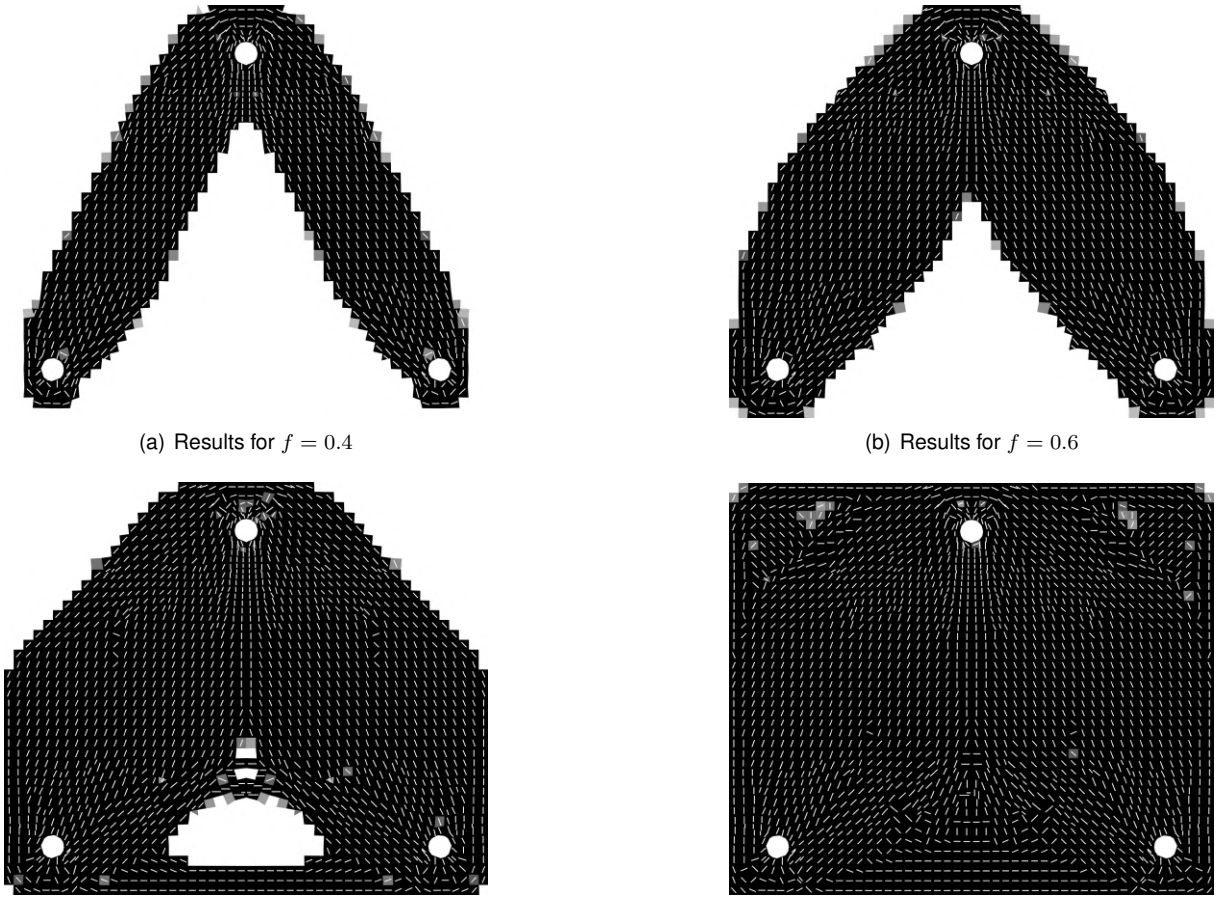

(a) Results for $f = 0.4$

(b) Results for $f = 0.6$

(c) Results for $f = 0.8$

(d) Results for $f = 1$

Figure 3.15: Results for the three-point tensile optimization using different volume fractions

Chapter 4

Experimental Testing and Results

In this chapter, experimental tests in structures printed using continuous fiber fabrication technology are performed, in order to validate the computational results for optimal material distribution and orientation using the DMO method. The structures are printed with a Markforged Mark Two printer using a sandwich panel design with the outer layers reinforced with fiberglass and a triangular nylon core. The material properties of the sandwich panel are obtained with the use of an Instron tension-compression test machine to allow a comparison between the computational and experimental results. The goal of the MBB beam experimental testing is to compare the stiffness of similarly weighted topology optimized structures with topology and material orientation optimized structures. In the 3-point tensile experimental testing, the goal is to compare quasi-isotropic structures against structures with optimized material orientation for different volume fractions. These tests serve to understand the advantages and disadvantages of topology optimization vs topology and material orientation optimization using CFF and also advantages and disadvantages of printed laminated, quasi-isotropic structures vs printed structures with optimized material orientation in the context of CFF.

4.1 Sandwich panel properties

To be able to establish a comparison between the computational and experimental results, the mechanical properties of the sandwich panels must be obtained. These include the Young's modulus E_1 and E_2, the shear modulus G_{12} and the Poisson's ratios ν_{12} and ν_{21} which are obtained using a unidirectional layered sandwich panel. Using a quasi-isotropic layup, the Young's modulus E and Poisson's ratio ν can also be obtained. These mechanical material properties are used in the material distribution and orientation optimizations and in the topology optimizations, respectively.

A quasi-isotropic layup is obtained by combining multiple, unidirectional fiber layers, in different orientations to simulate the in-plane properties of an isotropic material. Since this is done by layers, the properties in the transversal direction won't be the same as in the other in-plane directions, hence the name quasi-isotropic.

As previously mentioned, the structures are printed using a Markforged Mark Two printer capable of

printing composite structures using continuous fiber filament. The .mdf files needed to use the printer are generated by the Markforged's browser slicing software, Eiger. In Eiger, the default, quasi-isotropic parameters consist in 4 fiber layers oriented at $[0^\circ, 45^\circ, 90^\circ, 135^\circ]$ at the top and at the bottom, resulting in a total of 8 fiber layers. This fiber fill type is called *Isotropic* and will be used to refer to this type of layup in the future. It can also be used to create a unidirectional layup by selecting only one angle.

The ASTM standard used to obtain the mechanical properties of the sandwich panel is the ASTM D3039 [43] also used by Markforged for their fiber composite test specimens. This test method is specifically designed for polymer matrix composite materials with the goal of determining their in-plane tensile properties.

In accordance with this standard, rectangular specimens were printed with dimensions 200 $\times$ 25 [mm] and a nominal thickness of 5 mm, as illustrated in Fig. 4.1. The specimens were printed using 8 fiber layers, in consideration for the default *Isotropic* parameters, to ensure each specimen had the same amount of fiber. The sandwich core was printed using the default triangular infill pattern with a 37% fill density. The wall layers were reduced to the minimum of 1 wall, to ensure maximum in-plane fiber deposition and the recommended value of 4 roof and floor layers were used.

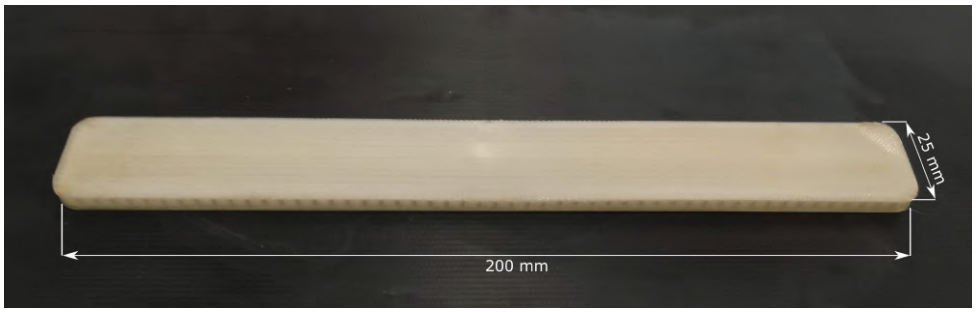

Figure 4.1: General dimensions for the rectangular specimens with a 5 mm thickness

In a study by Ferreira et al. [44], focusing on the mechanical characterization of 3D printed materials reinforced with short carbon fibers, 3 specimens configurations are required to fully characterize E_1, E_2, G_{12}, ν_{12} and ν_{21}. Young's modulus E_1 and Poisson's ratio ν_{12} can be determined using a laminate with fibers printed at 0° along the tensile direction. E_2 and ν_{21} are obtained with a 90° stacking sequence and to determine G_{12}, alternating layers at 45° and -45° are used. The isotropic properties E and ν are determined using a $[0^\circ, 45^\circ, 90^\circ, -45^\circ]$ stacking sequence.

Although the testing of five specimens per sample is recommended, due to shortage of strain gauges at the time, only one specimen per sample was tested. This allows an estimate of the in-plane tensile properties of the sandwich panel, but further testing would be required for a more in-dept analysis. The four specimens were printed with stacking sequences $[0^\circ]_{4s}$, $[90^\circ]_{4s}$, $[45^\circ / -45^\circ]_{2s}$ and $[0^\circ, 45^\circ, 90^\circ, -45^\circ]_s$ using Markforged's fiberglass and nylon filament, whose properties can be found in B.1.

The experiments were performed using an Instron 3369 universal testing system with a 50 kN load cell. All but the 90° specimen were tested until material failure occurred. Strains were measured using an extensometer/strain gauge combination. The strains aligned with the loading direction were measured

with a static clip-on extensometer while the strains in the loading transversal direction were measured at determined load intervals using a BFLA-5 strain gauge. The experimental assembly is demonstrated in Fig. 4.2. The strain-stress curves resulting from the tensile tests are shown in Figs. 4.3 and 4.4. Fig. 4.5 shows the tested specimens after the experiments.

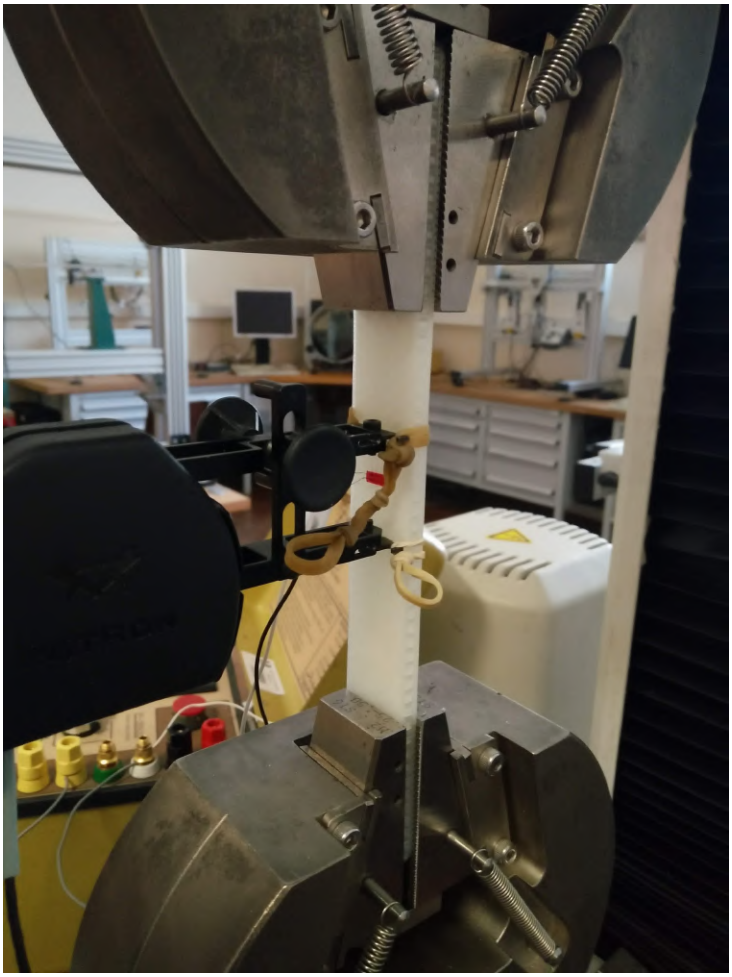

Figure 4.2: Setup for the tensile test

With the strain-stress results, the in-plane tensile properties of the unidirectional and the *Isotropic* composite sandwich panels can be obtained. These are shown in Tables 4.1 and 4.2.

Table 4.1: In-plane tensile properties for the unidirectional composite sandwich panel

Parameter	Symbol	Value
Young's modulus (GPa)	E_1	3.869
	E_2	0.356
In-plane shear modulus (GPa)	G_{12}	0.742
Poisson's Ratio	ν_{12}	0.426
	ν_{21}	0.022

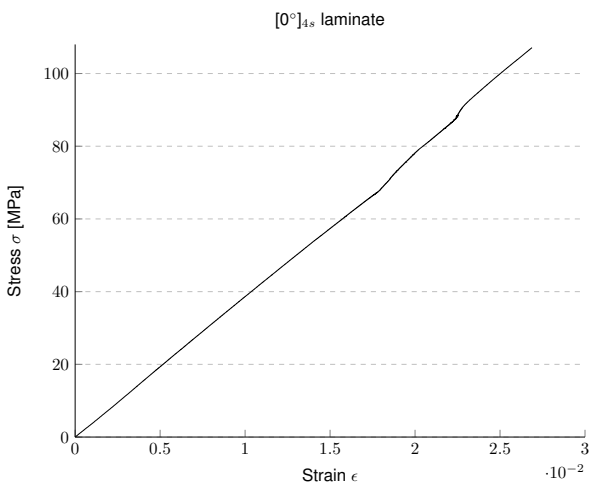

(a) Strain-stress data for the $0°$ specimen

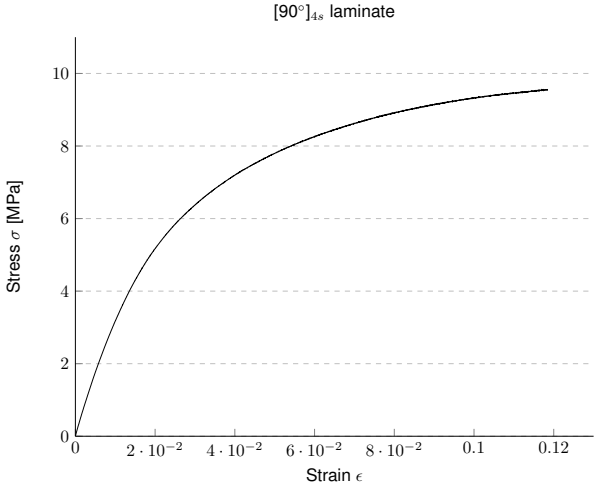

(b) Strain-stress data for the $90°$ specimen

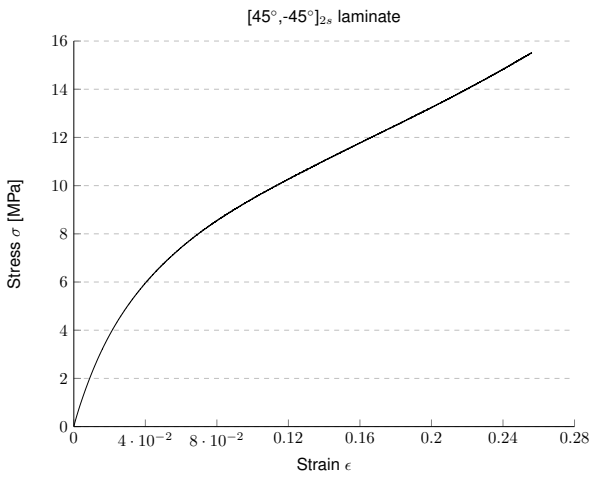

(c) Strain-stress data for the $\pm 45°$ specimen

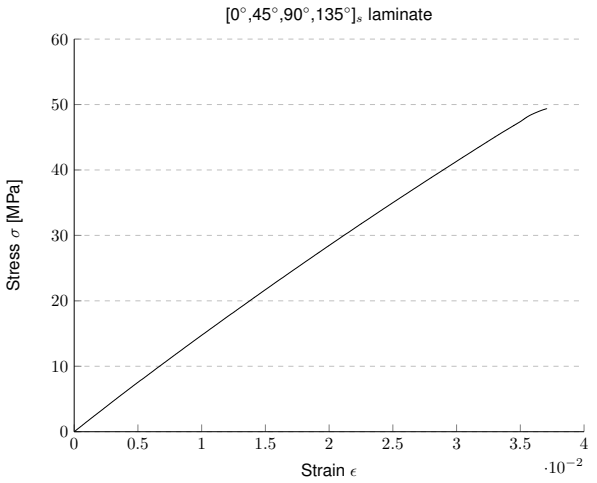

(d) Strain-stress data for the *Isotropic* specimen

Figure 4.3: Strain-stress results for the various laminates

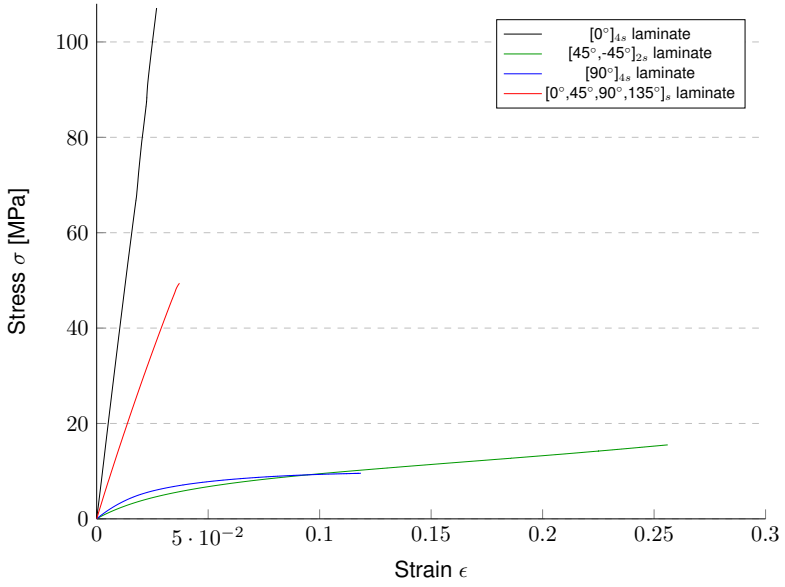

Figure 4.4: Combined strain-stress results for the various laminates

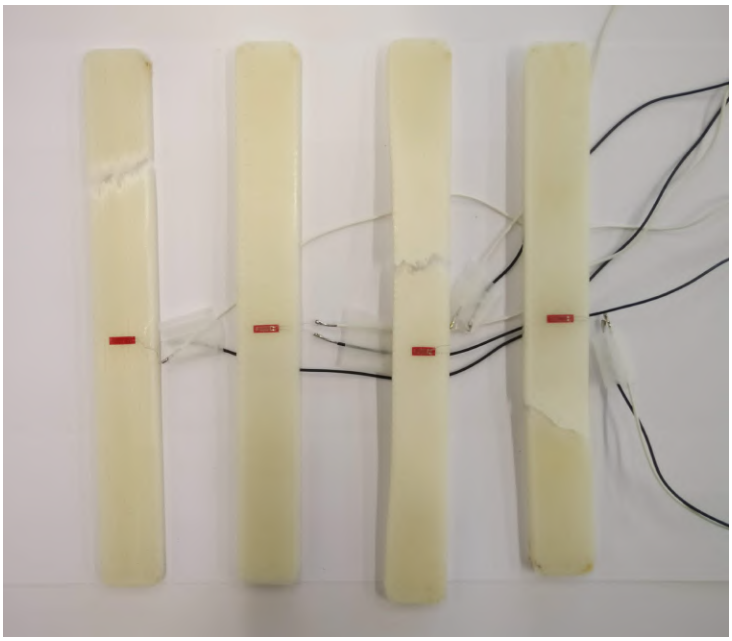

Figure 4.5: Tested specimens with unidirectional fiber configuration 0^o, 90^o, $\pm 45^o$ and $Isotropic$ configuration, respectively

Table 4.2: In-plane tensile properties for the *Isotropic* composite sandwich panel

Parameter	Symbol	Value
Young's modulus (GPa)	E	1.513
Poisson's Ratio	ν	0.394

4.2 MBB beam optimization, printing and experimental results

In this section, the final designs for the MBB beam optimization problem are determined taking into account the printer limitations and the in-plane tensile properties obtained in section 4.1. One design consists in a structure assuming an orthotropic material optimized in its distribution and orientation. The other structure will assume an isotropic material that will be optimized in its distribution. Both structures are printed using the $Concentric$ fiber fill type in which the fiber is printed parallel to the walls. The goal of this experiment is to compare the stiffness of structures optimized considering the orthotropic nature of CFF printing and topology optimized structures.

4.2.1 MBB beam final designs

One limitation of printing using CFF has to do with the invariable width of the deposited fiber filament. A minimum fiber reinforcement feature width of 2.8 mm is recommended by Markforged to allow the use of a single fiber strand as reinforcement. Thinner features may not be fiber reinforced, depending on other printing parameters, such as number of wall layers. To fit two fiber strands, the minimum recommended width is 3.6 mm. This is illustrated in Fig. 4.6. To account for these limitations, the filter radius used in

the optimizations must be set to half of the minimum recommended width of 2.8 mm, meaning that $r =$ 1,4 mm. This value for the filter radius was already used in previous optimizations for this reason.

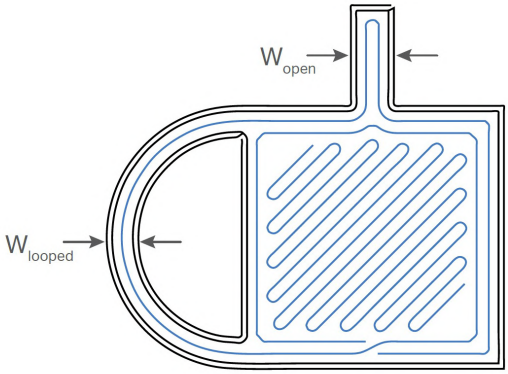

Figure 4.6: Minimum fiber reinforcement feature width [8]

As previously mentioned, two different optimizations will be performed. The first optimization, named *MBB_ORTHO*, will be using the orthotropic properties previously obtained with $E_1 = 3.869$ GPa, $E_2 =$ 0.356 GPa, $G_{12} = 0.742$ GPa and $\nu_{12} = 0.426$ oriented at $[90°, \pm 67.5°, \pm 45°, \pm 22.5°, 0°]$. This will be performed for material distribution and orientation optimization. The second optimization, named *MBB_ISO*, uses the previously determined isotropic properties $E = 1.513$ GPa and $\nu = 0.394$. The focus of this optimization is the material distribution. The optimization parameters used are the same as those in Section 3.2.1.1 as well as an imposed material usage of 50%, $f = 0.5$, and filter radius $r = 1.4$ mm. The beam geometry is modeled using a 144 by 64 mesh of rectangular elements, with a nominal thickness of 1 mm. The use of a more refined mesh results in a smoother optimal structure which is easier to correctly model as will be shown further in the chapter. The optimizations results can be seen in Table 4.3 and Fig. 4.7.

Table 4.3: MBB beam results for the *MBB_ORTHO* and *MBB_ISO* optimizations

Optimization	Number of iterations	Total Time [s]	Final Compliance [N.m] $\times 10^{-6}$	Volume Fraction	Convergence
MBB_ORTHO	83	13735	21.847	0.4850	0.953
MBB_ISO	61	4317	53.713	0.4745	0.952

The results show a similar optimal material distribution for both cases with the material distribution of *MBB_ORTHO* resembling the results seen in Fig. 3.11(e), for a material with $\beta = 1.429$. Since the parameter β for the material used in *MBB_ORTHO* is $\beta = 1.022$, this similarity of material distribution using materials with similar shear stiffness should be object of future studies.

Despite these results, since previous studies in Section 3.2.1.1 indicated a possibility of these being

[8] Figure taken from Markforged design guide. `https://s3.amazonaws.com/mf.product.doc.images/Composites_DesignGuide/CompositesDesignGuide_V1-2.pdf`, . Accessed: 16-09-2019

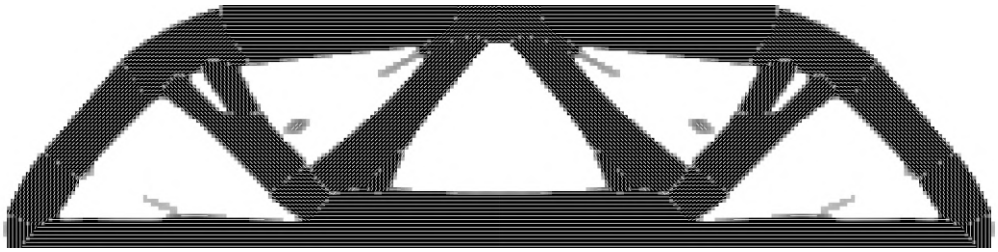

(a) Optimal material and fiber angle distribution for the *MBB_ORTHO* optimization

(b) Optimal material distribution for the *MBB_ISO* optimization

Figure 4.7: Optimal material distribution and orientation results for the *MBB_ORTHO* and *MBB_ISO* optimizations

local minimum solutions, previous optimization results were analyzed by substitution of the materials used in *MBB_ORTHO* and *MBB_ISO*. Although this does not guaranteed that the final designs are global minimum solutions of the optimization problem, they guarantee better final designs. The results of this study can be seen in Table 4.4, in which the compliance improvement per weight is presented. The material and fiber angle distribution can be seen in Fig. 4.8.

Table 4.4: Final MBB beam results for the *MBB_ORTHO* and *MBB_ISO* optimizations

Optimization	Final Compliance [N.m] $\times 10^{-6}$	Volume Fraction	Convergence	Improvement per weight [%]
MBB_ORTHO	21.248	0.490	0.930	1.74
MBB_ISO	46.522	0.493	0.962	10.01

4.2.2 MBB beam printed designs

With the establishment of the structures final design, the 3D printing process can begin. In order to use a slicing software such as Eiger, an .stl file must first be created containing the structure's geometrical information. To create the .stl file, the program used was the CAD program SolidEdge ST10, although other CAD programs could have been used for the same purpose. To transform the obtained 2D results to a 3D structure, a BMP image of the results was used, allowing the tracing of the contours of the structure using splines, lines and the round feature. Fig. 4.9 illustrates this process. To increase the stability of the structure during the tests, a thickness of 10 mm was used for the structure.

With the STL file created, the Eiger software can now be used to define the printing parameters. In

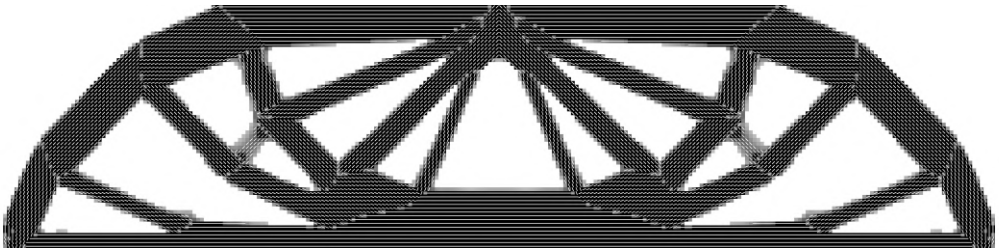

(a) Final optimal material and fiber angle distribution for the *MBB_ORTHO* optimization

(b) Final optimal material distribution for the *MBB_ISO* optimization

Figure 4.8: Final optimal material distribution and orientation results for the *MBB_ORTHO* and *MBB_ISO* optimizations

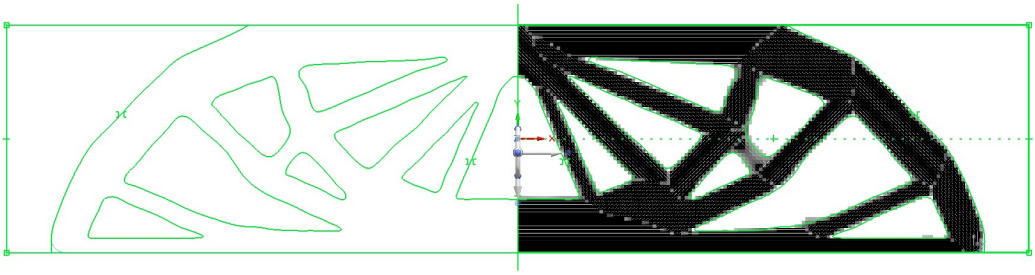

Figure 4.9: Obtaining the contour of the *MBB_Ortho* structure using SolidEdge

order to replicate the material orientation of the optimizations, aligned with the principal stress directions which are parallel to the structure's walls, the *Concentric* fiber fill type was used. Since the structures now have twice the thickness of 5 mm used in the sandwich panels tested in Section 4.1, a total of 16 fiber layers should be used to maintain the fiber/nylon ratio used in the sandwich panels. Other printing parameters such as the fill pattern and number of wall layers remained the same, respectively, 37% triangular fill pattern and 1. Regarding the roof and floor layers, which are layers printed using solid infill in the external layers and also before and after a consecutive set of fiber layers, these also remained the same with the value of 4. However, since these are nylon layers using a solid infill, they should also be doubled. This was accomplished by dividing the 16 fiber layers into 4 equal groups, 2 at the top and 2 at the bottom and separated, forcing the software to double the nylon layers. The reasoning behind this was to maintain the four consecutive fiber layers used in the sandwich panels. A symmetric fiber deposition can be ensured by modifying the *Start Rotation Percent* parameter for every fiber layer. This tells the printer were it should start printing fiber in each layer. Due to the fiber printing limitations, only certain positions allow the fiber to be symmetrically deposited. Fig. 4.10 shows the 3D and 2D internal view of the *MBB_ISO* structure in the Eiger program.

In Fig. 4.11, a comparison between the optimal material and fiber angle distribution and the fiber

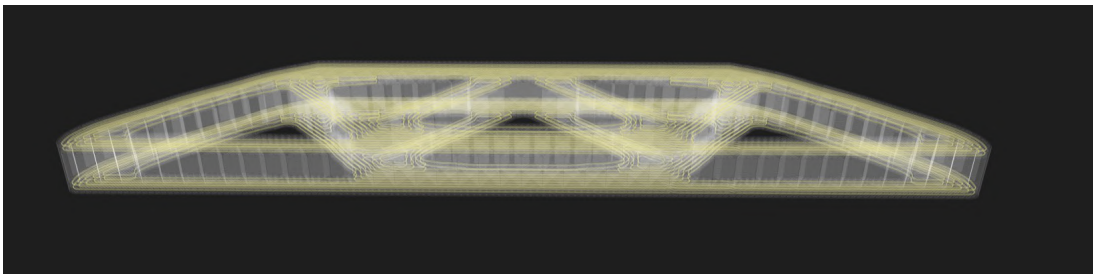

(a) 3D internal view for *MBB_ISO* structure illustrating the different layers distribution

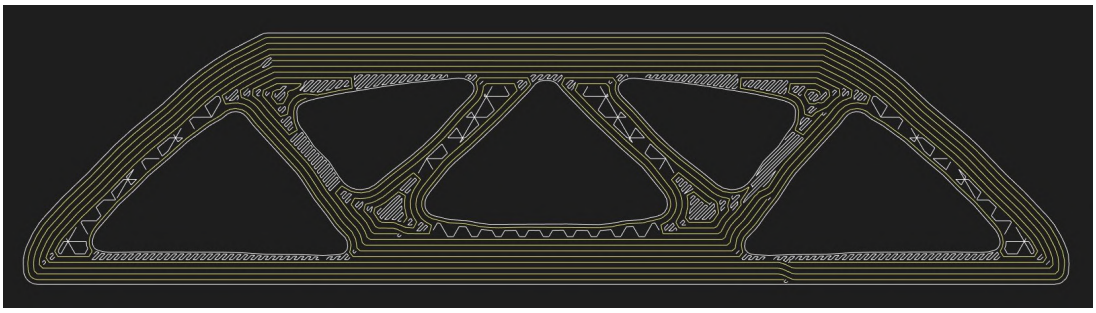

(b) 2D internal view for *MBB_ISO* structure illustrating the material deposition in the fiber layers

Figure 4.10: 3D and 2D representations of the *MBB_ISO* structure in the Eiger program

deposition in the printed results is shown. As mentioned before, one of the printing limitations of using fiber is the minimum reinforcement width for which fiber can be placed. Other limitations include the minimum fiber length that can be used, which is 45 mm, corresponding to the length between the fiber cutter and the nozzle. These limitations, combined with the program specifications to try to use the maximum of continuous fiber possible, results in certain areas of the fiber layers needing to be filled with nylon, differing from the computational results.

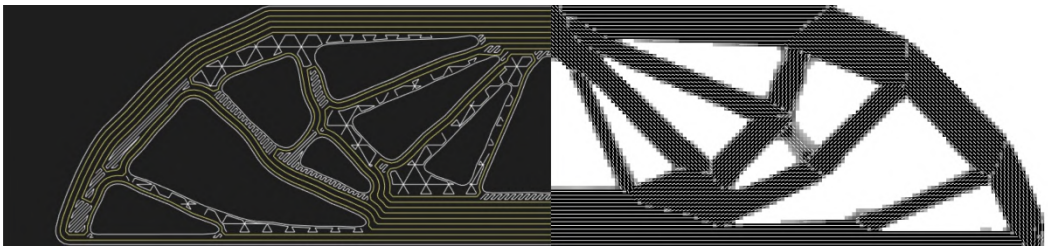

Figure 4.11: Side-by-side comparison of the material distribution and orientation between the printed structure and optimization result for the *MBB_Ortho*

In order to promote bed adhesion and prevent warping, the structures were printed using brim and the recommended Elmer's Disappearing Purple Glue was used. A total of six structures were printed, three for each design. Each *MBB_ORTHO* structure took approximately 7h of printing time while each *MBB_ISO* structure was printed in approximately 5h30m. The final printed structures can be seen in Fig. 4.12.

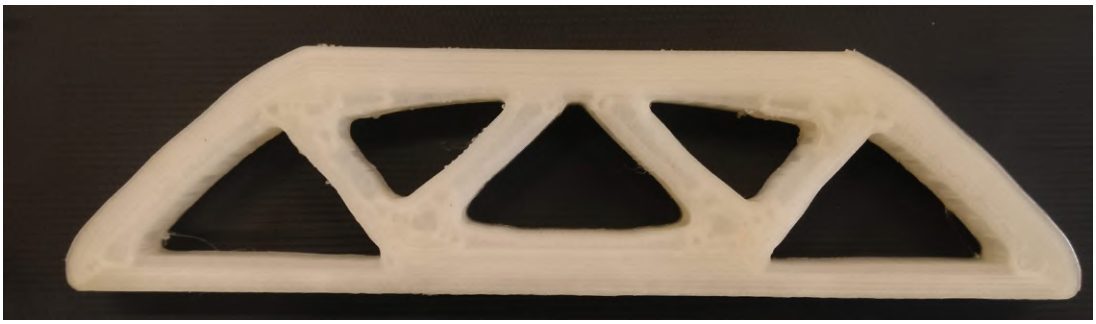

(a) Printed *MBB_Ortho* structure

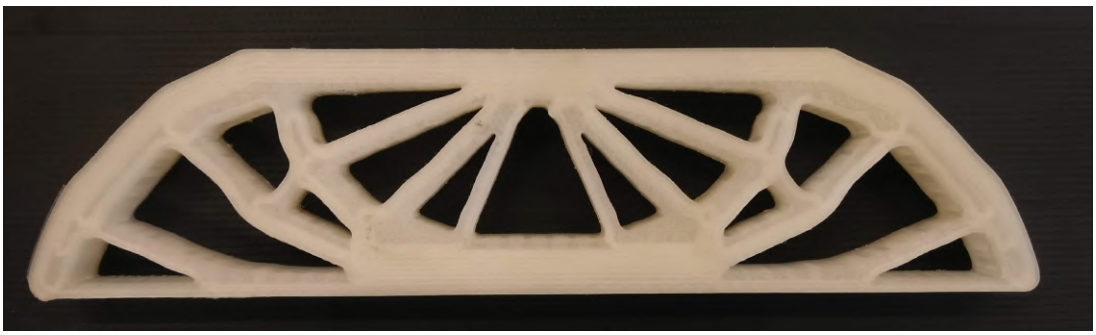

(b) Printed *MBB_ISO* structure

Figure 4.12: Printed MBB structures

4.2.3 MBB beam experimental results

To provide a fair comparison between the different structures, the total mass of each structure should be registered since heavier structures tend to be stiffer than lighter ones. These measurements will allow us to compare the different stiffness results using a normalized stiffness. Although both structures were optimized using a 50% material volume and the final volume fraction being 49% for both structures, due to the transformation to a 3D structure, the different material depositions and other factors can lead to a difference in weight. These measurements can be seen in Table 4.5 that shows the weight of the different samples in grams, after removing the brim and protruding material left from the printing process and wiping the leftover glue.

As was expected, the weight distribution is similar across all samples with slight variations between them. These will be taken into consideration when presenting the stiffness test results.

To test the MBB structures, a three point bending setup was used in an Instron 5566 universal testing machine with a 10 kN load cell. The printed beams were placed in the two support cylinders of the fixture which were distanced 160 mm from each other's center, simulating the boundary conditions used in the finite element model. This allows free horizontal movement in those points while fixing the vertical displacement. The loading cylinder sits in the top center of the beam, exerting a downwards force corresponding to the loading conditions used. The setup for this experiment can be seen in Fig. 4.13.

Since the stiffness is computed as the linear relation between the applied load and the resulting displacement, to determine the experimental stiffness of the structures, the slope of the linear elastic

Table 4.5: Weights of the MBB structures printed using CFF

MBB Sample	Weight(g)
MBB_ORTHO_1	28.20
MBB_ORTHO_2	28.18
MBB_ORTHO_3	28.18
MBB_ISO_1	27.16
MBB_ISO_2	27.04
MBB_ISO_3	27.15

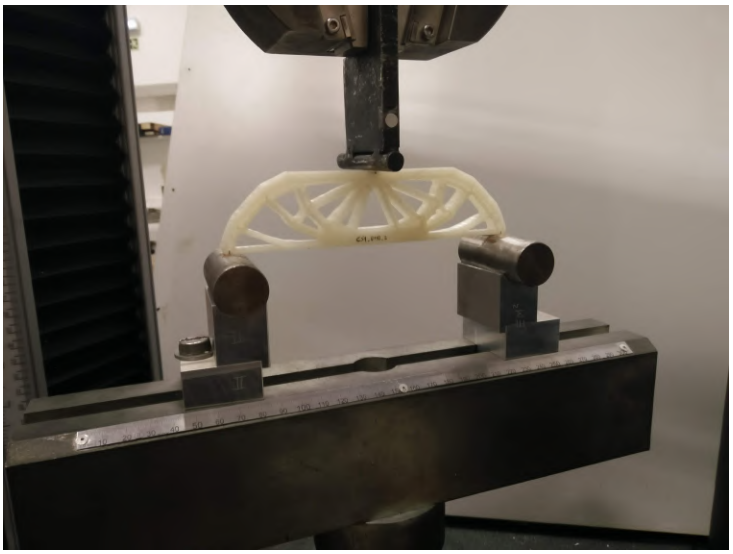

Figure 4.13: Experimental setup for testing of the printed MBB beam structures

region in the load-displacement curve must be determined. This is accomplished by selecting a set of points in the linear elastic region and calculating the linear regression for these values. The linear regression value represents the stiffness of the structure, given in SI units as N/m.

Before each sample's test, the correct positioning and alignment of the structures was verified to make sure the force was applied in the top center of the beam and the cylinders were perpendicular to the structure. For one sample of each structure, the experiment proceeded until structural failure of the sample in order to understand the structural behavior of the structure until the point of failure. The rest of the structures were tested until a displacement of around 3.5 mm was reached, so as to not break the structures. The load-displacement curves for the three point bend tests can be seen in Figs. 4.14 and 4.15. During the testing of the *MBB_ORTHO_1* sample, an improper positioning of the structure, which was not correctly centered, resulted in a displacement of the structure to the side with the increased load. This invalidated the results for the structural failure test, which were then repeated for *MBB_ORTHO_2*. From Fig. 4.15, the stiffness of each structure is determined by obtaining the slope

of the load-displacement curves from data-points inside the linear elastic region. Table 4.6 displays the experimental stiffness and normalized stiffness values for each sample as well as the theoretical values.

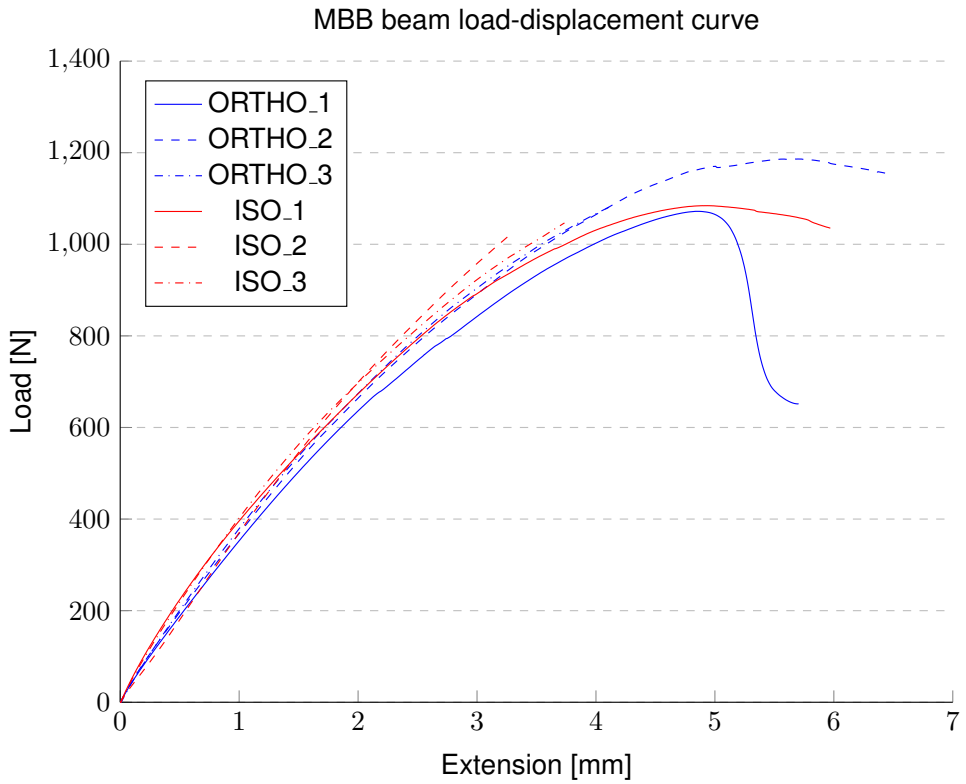

Figure 4.14: Load-displacement curves for the 3 point bending test of optimized MBB structures

Table 4.6: Experimental and theoretical stiffness results for the 3 point bending test of optimized MBB structures printed using CFF

MBB Sample	Stiffness [N/m]$\times 10^3$	Normalized Stiffness [N/m]$\times 10^3$
MBB_ORTHO_1	284.06	284.06
MBB_ORTHO_2	295.47	295.68
MBB_ORTHO_3	293.75	293.96
MBB_ISO_1	276.34	286.92
MBB_ISO_2	328.33	342.42
MBB_ISO_3	294.74	306.14
MBB_ORTHO_THEO	940.96	
MBB_ISO_THEO	913.04	

From analysis of Fig. 4.14, both types of structures fail after a loading cylinder's displacement of

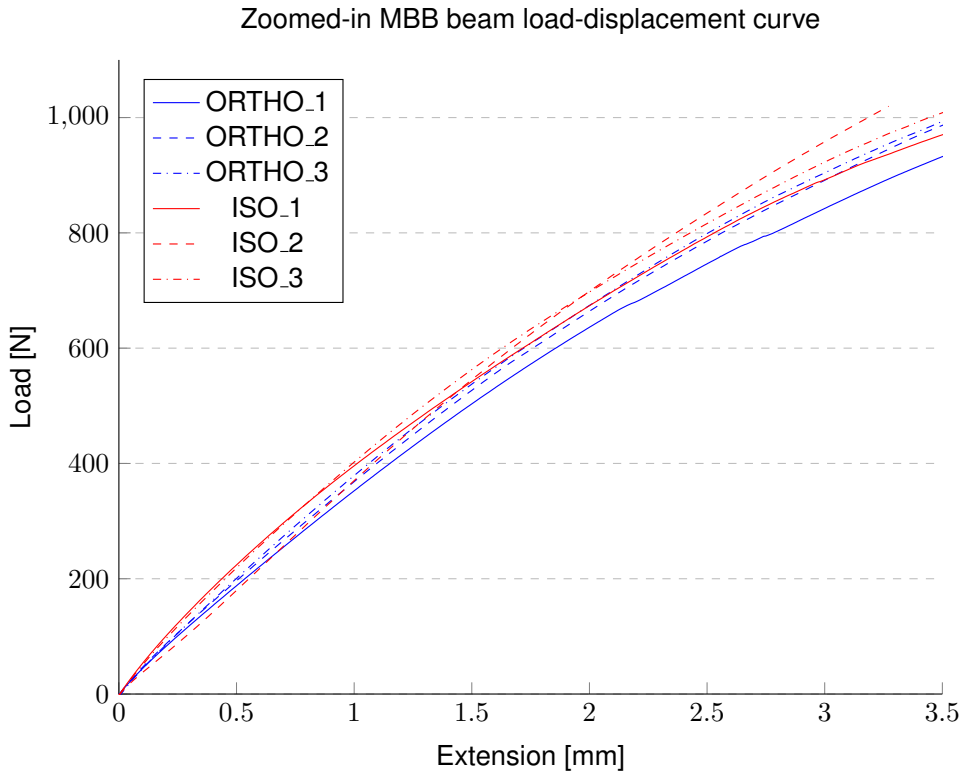

Figure 4.15: Zoomed-in load-displacement curves for the 3 point bending test of optimized MBB structures

5 mm, with the failure of *MBB_ORTHO* occurring at higher loads. However, further testings would be required since one result for each structure only allows simple observations. From the analysis of the experimental stiffness results, the structures seem to have similar stiffness, with the *MBB_ISO* having a greater variation in results and an overall better performance. These experimental results contradict the theoretical results obtained through the optimizations. These differences can be related to the printing patterns, which cannot be replicated through the optimization program. The results will be discussed further in section 4.4.

4.3 3-point tensile optimization, printing and experimental results

In this section, the 3-point tensile design will be tested for different volume fractions and fiber fill types. A method to enforce the optimal material orientation will be tested as well as a study of hole tolerance. To test the designs, special fixtures were machined. The goal of these tests is to compare the stiffness between designs printed with optimal material orientation and the default *Isotropic* fiber fill, for different volume fractions.

4.3.1 3PT final designs

As seen in section 4.2.1, the final designs for the MBB structures were obtained by performing optimizations with the material properties determined in 4.1. Using a similar approach for the 3PT structure, two

optimizations were performed for 2 different volume fractions. The material used in the optimizations has orthotropic properties $E_1 = 3.869$ GPa, $E_2 = 0.356$ GPa, $G_{12} = 0.742$ GPa and $\nu_{12} = 0.426$ oriented at $[90°, \pm 67.5°, \pm 45°, \pm 22.5°, 0°]$. The same optimizations parameters seen in section 3.2.1.2 were used and the imposed volume fractions were $f = 0,4$ and $f = 1$. The optimizations results can be seen in Table 4.7 with the material distribution and orientation represented in Fig. 4.16. The finite element mesh was discretized using 8608 quadrilateral elements and 144 triangular elements with size 1 mm.

Table 4.7: Final 3PT optimization results for volume fractions $f = 0,4$ and $f = 1$

Optimization	Final Compliance [N.m] $\times 10^{-6}$	Volume Fraction	Convergence
3PT_0,4	1.058	0.398	0.981
3PT_1,0	0.968	1.000	0.979

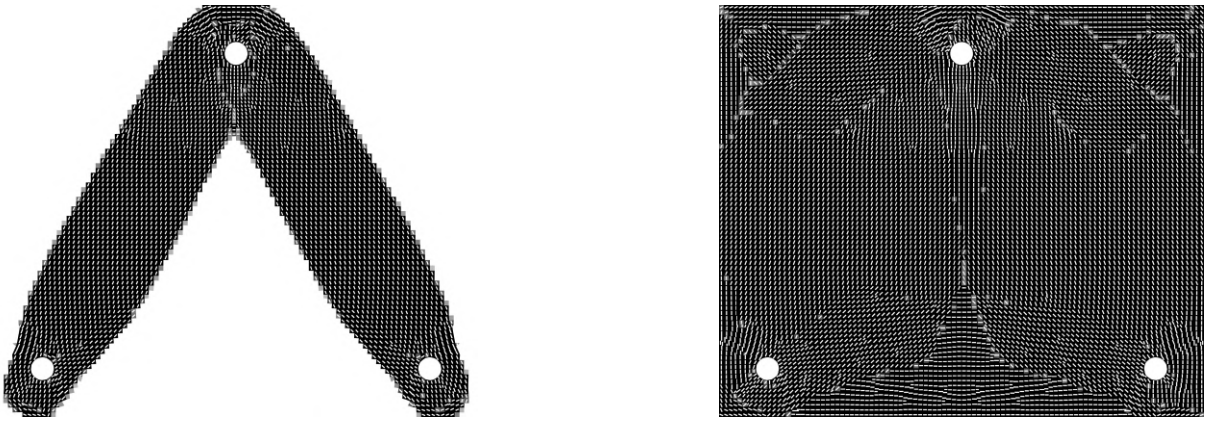

(a) Results for $f = 0.4$

(b) Results for $f = 1$

Figure 4.16: Final structures for the 3PT optimization results for volume fractions $f = 0,4$ and $f = 1$

4.3.2 3PT test setup and printing

To test the structures, fixtures had to be designed and machined to be used in a tensile test. Two fixtures were machined in a milling machine. The top fixture, where the stresses would be greater, was machined from a 12 mm steel plate and the bottom fixture was machined from a 7075 aluminum block. The fixtures were machined so that the structure would sit in between the 6 mm grooves, attached by long M5 screws so that the smooth cylindrical part of the screw was in contact with the structure, to simulate the bearing load used in the simulations. The setup's assembly with the fixtures and structure is represented in Fig. 4.17.

To print the structure in Fig. 4.16(a), the *Concentric* fiber fill type can be used to approximate the optimal material orientation. This however is not the case for the structure in Fig. 4.16(b), since using the *Concentric* fiber fill type leads to the fiber printing pattern illustrated in Fig. 4.18. In order to force

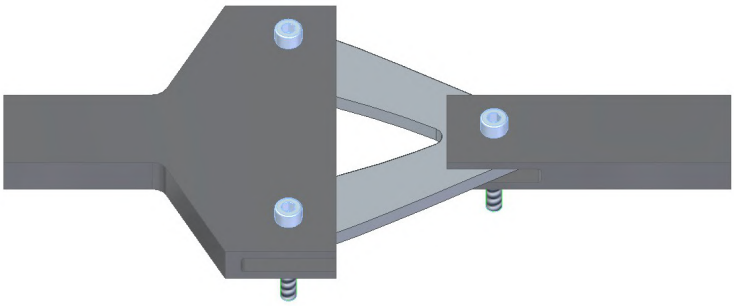

Figure 4.17: CAD representation of the assembly of the 3PT testing setup

Eiger to print the fiber in a pattern similar with the results obtained from the optimizations, a proposed method was used, consisting in cutting small, 0,1 mm features which are recognized by the program and reinforced. Since these features are so small, the objective was that these would be closed by the printer, due to it's inability to reproduce such small features. However, other printing parameters need to be used for these gaps to be closed, since by default the program enlarges them to be able to reproduce them. In order for this to happen, the parameter *Expand thin features* must be used, which will force the program to try and print these features in their real size at the expense of some dimensional accuracy. Fig. 4.19 shows the comparison of prints with/without *Expand thin features* ON.

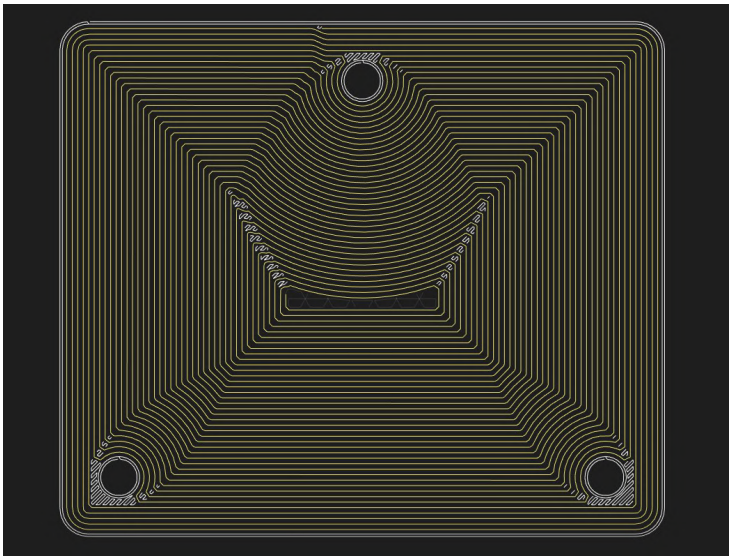

Figure 4.18: Printing pattern using *Concentric* fill type for the unmodified $f = 1$ 3PT structure

Using this technique, a total of 10 unique variations of the structure in Fig. 4.16(b) were developed to find the one that could best approximate to the optimal material orientation. Fig. 4.20 shows four of these variations. All the variations can be found in A.1.

Other tests that involve testing printing parameters is the hole tolerance parameters. Since we will be using M5 screws, in order to achieve a perfect fit between the holes and the screws, a set of hollowed cylindrical structures were printed, with various hole diameters. These can be seen in Fig. 4.21. These tests were performed with and without the *Expand thin features* parameter ON, since the use of this

Figure 4.19: Side by side comparison of using the *Expand thin features* ON and OFF, respectively

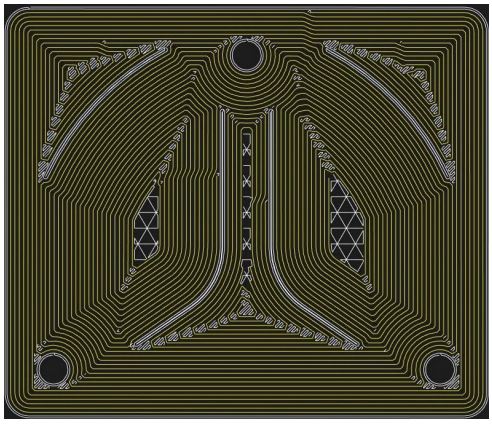

(a) Variation # 1

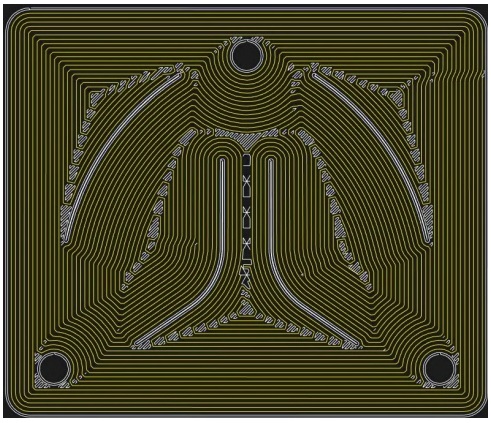

(b) Variation # 4

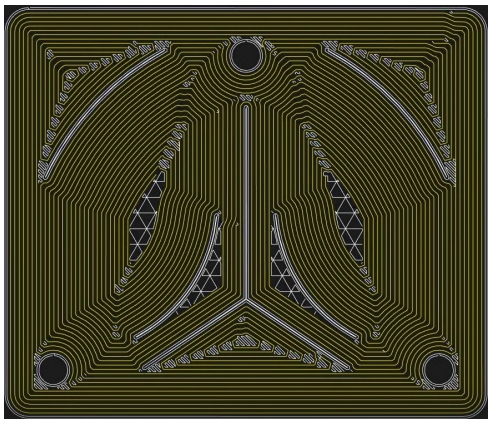

(c) Variation # 6

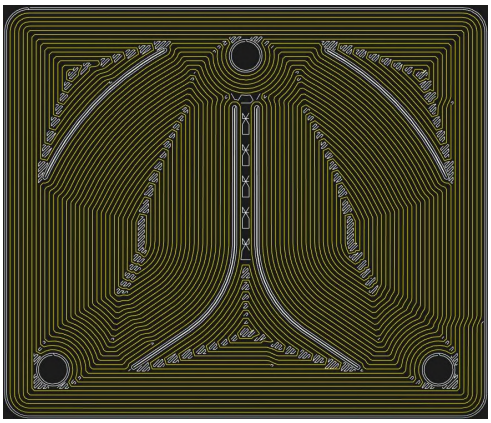

(d) Variation # 9

Figure 4.20: Some variations in printing pattern for the 3PT structure

parameter results in holes with a smaller size than the defined diameter. Using these tests, the required hole dimensions for an M5 screw were determined to be:

- ø5 mm with *Expand thin features* "OFF"
- ø6 mm with *Expand thin features* "ON"

Using the results from these experiences, 2 different structures were first printed and tested, with 3 samples per structure and fiber fill type, resulting in a total of 12 printed samples. These first samples were printed before the material properties were known, using the previous results determined in Section 3.2.1.2.

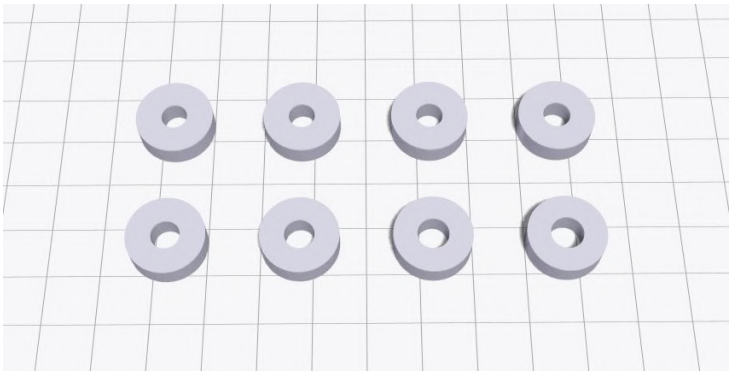

Figure 4.21: Printed structures with different diameters to determine dimensional tolerance for holes

The samples were printed using the previous printing parameters. A reinforcement of 3 concentric rings around the holes in a total of 4 layers were used to prevent the holes deformation from influencing the results. Each structure was printed with a thickness of 5mm. A comparison between the computational results and the fiber printing pattern is shown in Fig. 4.22.

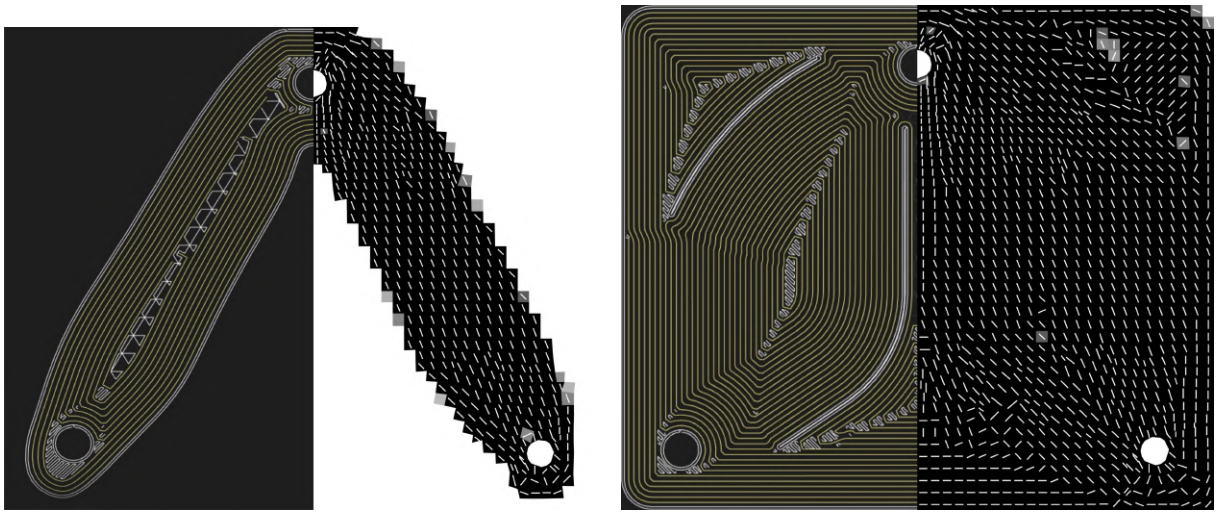

(a) Structure with $f = 0.4$

(b) Structure with $f = 1$

Figure 4.22: Side by side comparison of the fiber orientation in the printed structures and the computational results

As can be seen, the same printing limitations observed in section 4.2.2 are present in these structures.

4.3.3 3PT experimental testing and results

To test the 3PT printed samples, a standard tensile setup was used in the Instron 3369 previously used to determine the in-plane tensile material properties. The machined fixtures were secured via mechanical grips while the structures were fixed by the three screws to the fixtures. The screws were held in place by nuts. The assembly was properly checked to make sure everything was properly aligned. The testing setup can be seen in Fig. 4.23.

As was previously done for the MBB beam tests, the stiffness of the different structures printed with

Figure 4.23: Experimental setup for the testing of the 3PT structures

the various printing patterns is to be obtained by the load-displacement curves obtained by the tensile tests. The load-displacement curves of the different tests can be seen in Fig. 4.24.

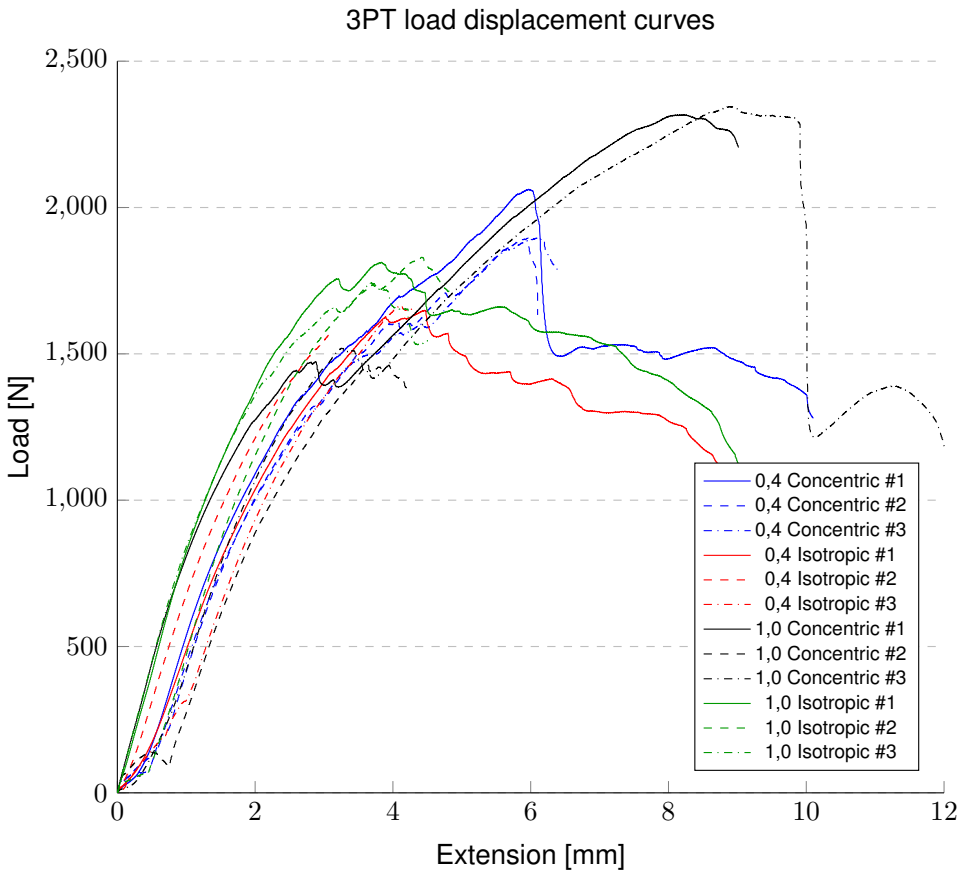

Figure 4.24: Load displacement curves for the 3PT tests

By observing that in all the curves the response to the loads was very similar, tests were performed to understand if the hole deformation was the cause, since the reinforcement of the holes was the same for all the samples. To test this theory, two samples were printed with volume fraction $f = 0.4$, with *Concentric* and *Isotropic* fiber fill. These samples had the holes reinforced in all the core layers, with a maximum of 5 concentric fiber rings reinforcing the top hole. These samples were tested in the same conditions of the first tests. The resulting load-displacement curves for these reinforced structures against the previous curves can be seen in Fig. 4.25.

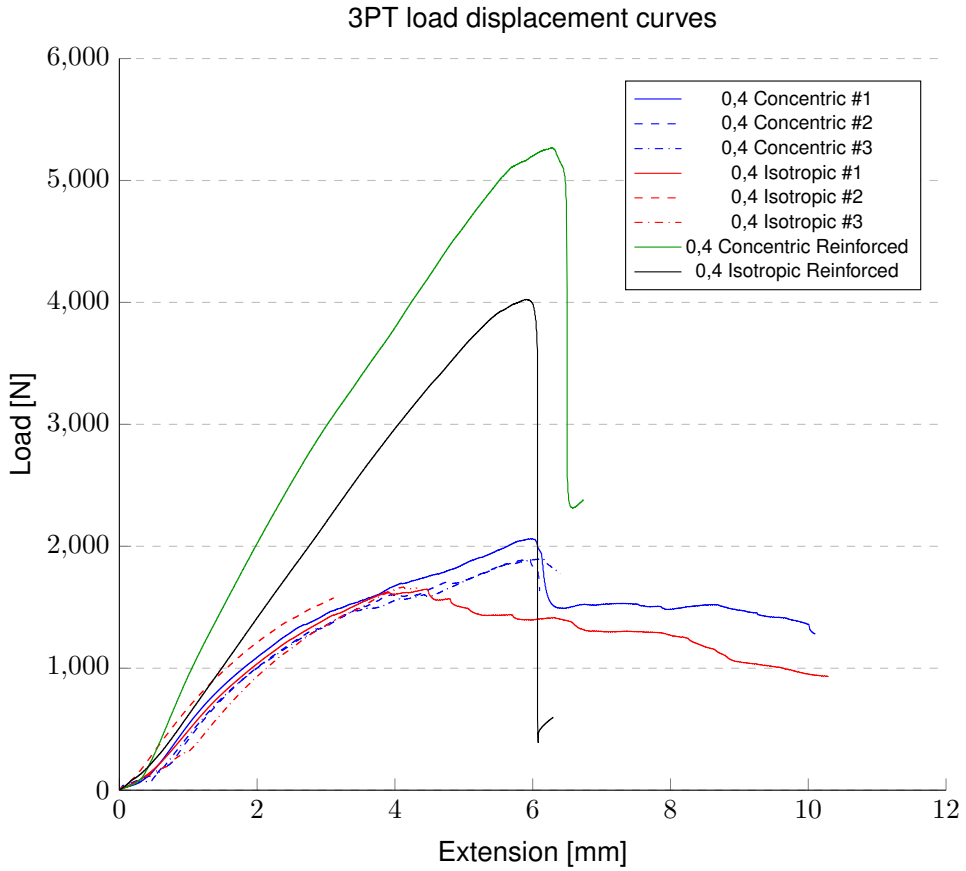

Figure 4.25: Load displacement curves for the 3PT tests with reinforced structures

This time both reinforced structures' load-displacement curves exhibit a distinct behavior from each other as expected, with the *Concentric* structure exhibiting a steeper linear-elastic slope, resulting in a greater stiffness, than the *Isotropic* structure as is expected. With these results, further tests were performed, this time with the holes fully reinforced to prevent the hole deformation from influencing the results. These tests were now performed with the optimizations result obtained in section 4.3.1, since the material properties were now known. During the first tests of 3PT_Concentric_1,0, a design flaw in the way the cuts were made to orient the fiber was exposed which lead to a modification of the design. Fig. 4.26 shows the printing pattern and optimal material distribution and orientation for the structures.

These designs were then printed and tested. The results can be seen in Figs. 4.27, 4.28, 4.29. From the load-displacement curves, the experimental stiffness can be determined as was previously done in section 4.2.3. Table 4.8 shows the experimental and normalized stiffness results of the samples tested.

(a) Structure with $f = 0.4$ (b) Structure with $f = 1$

Figure 4.26: Side by side comparison of the fiber orientation in the printed structures and the computational results for the final structures

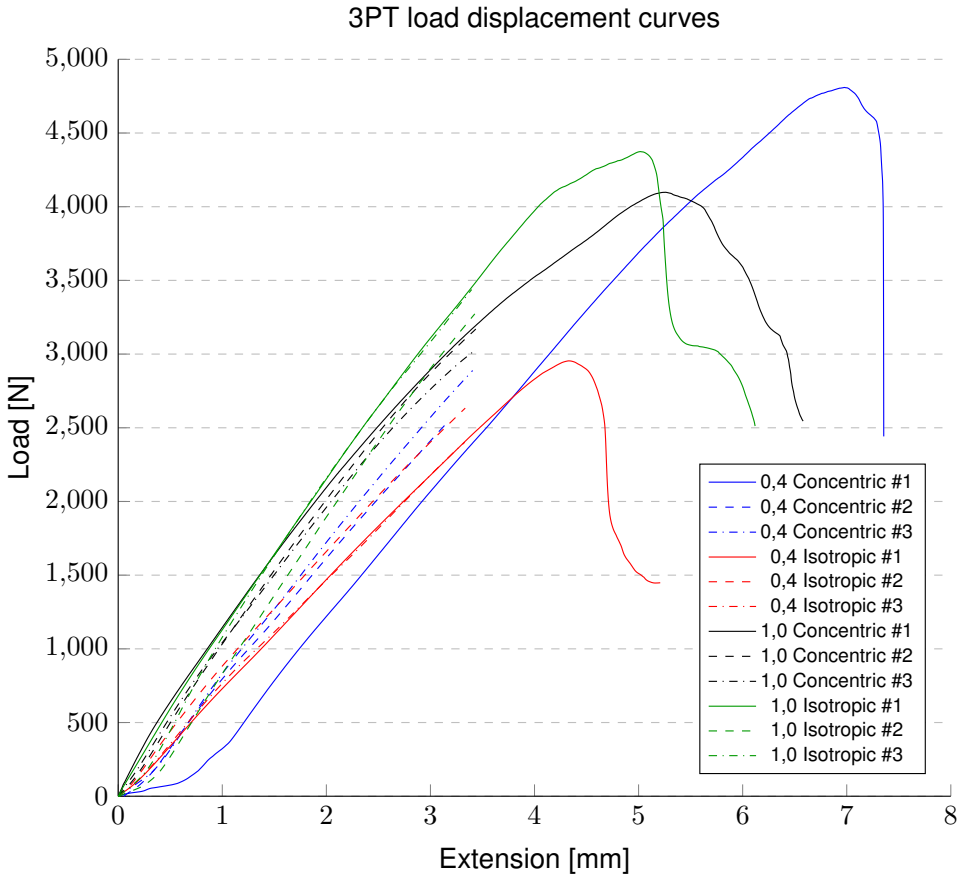

Figure 4.27: Load-displacement results for the final testing samples of 3PT structures

By analyzing the load-displacement curves, several conclusions can be drawn. Since the ultimate-stress for the 0,4 Concentric structure is greater than the 1,0 Concentric one, this leads to the conclusion that the technique for orienting the fiber with the use of small cut features was not very successful for this problem. The similar ultimate-stress results of the 1,0 structures in Fig. 4.29 (which contrast greatly with

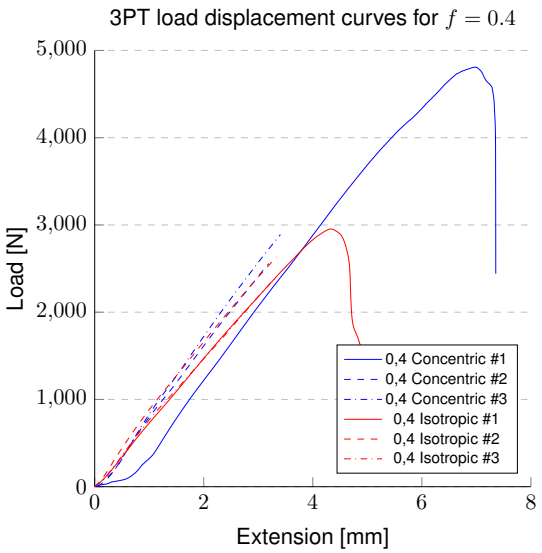

Figure 4.28: Load-displacement results for the final testing samples of $f = 0.4$ 3PT structures

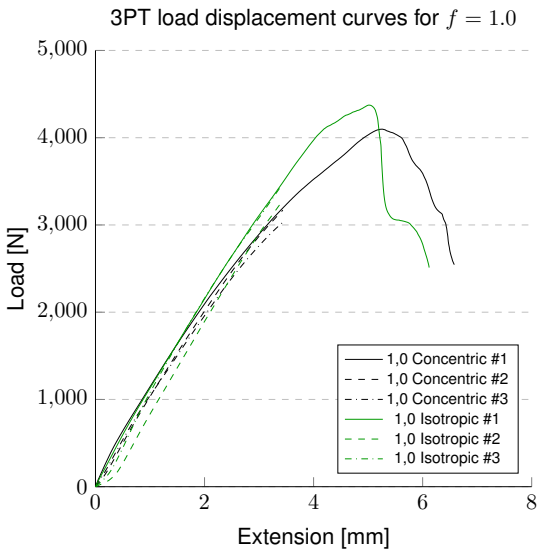

Figure 4.29: Load-displacement results for the final testing samples of $f = 1$ 3PT structures

Table 4.8: Experimental and theoretical stiffness results for the tensile test of optimized 3PT structures printed using CFF

Volume fraction	Sample	Weight [g]	Stiffness [N/m]$\times 10^3$	Normalized Stiffness [N/m]$\times 10^3$
f=0.4	Concentric Fill			
	#1	14.08	923.18	2233.20
	#2	13.87	815.61	2002.86
	#3	13.91	886.58	2170.88
	Comp. Result		3780.71	
	Isotropic Fill			
	#1	13.80	741.84	1830.95
	#2	13.90	774.23	1897.14
	#3	13.79	694.64	1715.70
	Comp. Result		1895.73	
f=1.0	Concentric Fill			
	#1	34.06	949.31	949.31
	#2	33.66	981.24	992.90
	#3	33.63	922.40	934.19
	Comp. Result		4653.87	
	Isotropic Fill			
	#1	33.12	1023.88	1052.94
	#2	33.11	1062.89	1093.39
	#3	33.22	1081.17	1108.51
	Comp. Result		2443.49	

the results obtained in Fig. 4.28 for the 0,4 structures) support this theory, since structures printed with the fiber oriented in the principal stress direction should have an increased ultimate-stress value when compared to structures printed with a quasi-isotropic laminate and using the same amount of fiber. The

effect of hole deformation is also possible, again revealing that this problem was not the most well suited to be tested.

By analyzing the stiffness results, again several conclusions can be drawn. The experimental results agree with the computational results in that the structures with a higher volume fraction have greater stiffness. For $f = 0,4$ the Concentric structures are stiffer than the Isotropic structures, as is expected. However, the computational results indicate that the stiffness difference should be twice as much, which is not the case. For $f = 1,0$, the opposite occurs with Isotropic structures being stiffer than the Concentric structures, which is not expected. This result could indicate that the technique is not useful in this case. When observing the normalized stiffness results, the value of the $f = 0,4$ structures are bigger than the $f = 1,0$ structures, almost by a factor of two, since the stiffness results don't increase as much as the weight. This justifies using the $f = 0,4$ structures since their stiffness/weight ratio is greater. The results from the experimental tests differ greatly in terms of numerical value from the computational results, which could be explained by the difficulty in simulating the behavior of the sandwich panel, due to the printing process, as the fiber can't be printed with the same distribution and orientation as in the optimization results and also because the local hole deformation may not be accounted for in the simulations.

4.4 Discussion of the experimental results

In this section, a discussion of the experimental results will be performed as well as the implications of using CFF to print the structures.

One complication of printing the structures using the Markforged's Mark Two printer lies with the difficulty to print full fiber layers as seen in Fig. 4.10(b). Due to the fiber deposition limitations, void spaces are created which are then filled with nylon. The existence of these void spaces lead to a lower experimental structural stiffness when comparing with the optimal results, since the latter can't account for the existence of these voids as can be seen in Fig. 4.11.

In the case of the MBB beam, both structures exhibit similar stiffness values as was expected. The experimental results reveal that the structure obtained by topological optimization is stiffer, with the computational results revealing the opposite situation. When analyzing the fiber volume used in each structure, these reveal that the *MBB_ISO* structure was printed with 4.10 cm^3 of fiber and the *MBB_ORTHO* was printed with 3.49 cm^3. Although both structures have similar weight, with the *MBB_ISO* structure being slightly lighter, it also uses more fiber to be printed. Due to the more intricate structure of the *MBB_ORTHO*, the fiber has a greater difficulty in following the optimal deposition created by the computational program, leading to the generation of more voids spaces than the simpler *MBB_ISO* structure, resulting in a structure with less stiffness as demonstrated by the experimental results.

For the 3PT structures, the presence of void spaces can also have an effect on the experimental results. The experimental results for the lighter structures confirm that orienting the fiber in the fiber layers according to the principal stress directions increases the stiffness of the structure when comparing with using a quasi-isotropic layup. However, the increase in the experimental stiffness is not as noticeable as

the obtained through the computational results. For the heavier structures, the experimental results confirm that these are stiffer than the lighter structures, with the structure printed using the quasi-isotropic layup revealing to be stiffer, contrary to the computational results. Although for the structure printed using the *Concentric* fill type an experimental technique was used to force the fiber to follow the optimal orientation, which could result in a weaker structure, hole deformation issues cannot be discarded, due to stress concentration in that area, explaining the small increase in stiffness among the lighter structures. In order to fully engage the fibers, a clamping mechanism, similar to the ones used for general tensile testing, should have been used. As it stands, conclusions about the fiber orientation technique used can't be drawn, since the boundary conditions used weren't suitable for the experiment.

In general, the results from the experimental testing confirmed, qualitatively, the results obtained by the computational program, in regards to the stiffness of the different structures during testing. Although the stiffness values obtained by the computational program are greatly superior to the values obtained by the experimental testing, due to the difficulty in accurately model the printing pattern of the printer, through these results one can infer which structure is preferable to print and the optimal printing orientation of the fibers.

Chapter 5

Conclusions and Future Work

In this chapter, conclusions drawn from this work are presented, followed by recommendations for future work in the area of optimization of fiber reinforced composite structures produced by AM processes.

5.1 Conclusions

The goal of this thesis was to develop a structural optimization program capable of determining optimal material distribution and orientation for structures created by FFF processes implementing continuous fiber filament. To this end, a Matlab program was developed based on the DMO method, using the MMA optimizer to minimize the compliance of the structure. This method uses as design variables the fiber with discrete orientation angles and a ”weak” material to represent the void, to determine the optimal material distribution. To allow the study of complex bidimensional structures, the finite mesh generation is performed by the finite element program Siemens Nx, using triangular and quadrilateral finite elements.

Although the use of the DMO method is not recommended to optimize FFF processes due to the continuous fiber deposition and the use of discrete fiber orientations by the method, it still proved successful in the optimization of the structures, producing similar results obtained by continuous fiber optimization methods for the study of the MBB beam. Even though in this work, the use of eight discrete material orientations was implemented, to satisfactory simulate continuous fiber orientation without excessively increasing the computation time, other parameterization methods could have been implemented that could increase the number of possible orientations while maintaining the processing time. This would allow to better simulate the continuous fiber process similarly to the CFAO method while still minimizing the local minima issues.

To test the developed program, the MBB beam and a three-point tensile problem were optimized in respect to the material distribution and orientation. The studies showed that changing the ratio of Young’s modulus has no significant effect on the final structure and material orientation, while changing the shear stiffness can have a significant impact in the material distribution and orientation of the final structures. Local minima issues were also discovered and attempts to reach better solutions were made. In order

to complement the computational results, experimental testing and characterization of the composite layup was performed and samples of the MBB beam and 3PT structures were printed and tested with fiberglass continuous fiber reinforcement using Markforged's Mark Two 3D printer, to determine their stiffness.

The major findings obtained by the experimental tests can be summarized as:

- Topology optimized structures and material distribution and orientation optimized structures have similar stiffness when printed with fiber oriented along the principal stress directions if the composite material has a shear stiffness similar to an isotropic material ($\beta = 0$).
- Lighter, functional structures have higher stiffness/weight ratio than heavier structures, but lower stiffness overall.
- Structures printed with optimal fiber orientation have better performance than structures printed with generic quasi-isotropic layups for the same fiber volume.
- Conclusions about the proposed fiber orientation technique can't be performed due to improper experimental testing, requiring further examination.
- The experimental results confirm the general findings obtained by the computational results for the MBB beam and 3PT structure, although with lower stiffness results due to the CFF process limitations and local stress concentration.

Given the presented work, the objectives proposed for this thesis are considered satisfied and the obtained results should help to further develop the optimization of structures produced by the FFF method using continuous fiber reinforcement.

5.2 Future Work

Several improvements to the presented work could still be implemented and will be presented here as future work ideas as follows:

- Instead of using the DMO4 and DMO5 parameterization methods, other methods could be used to increase the number of possible orientations without increasing the computation time.
- Use of a discrete "weak" material lead to convergence difficulty. Use of a SIMP like method of using a pseudo-density could prove more useful.
- An Equivalent Single Layer Model (ESLM) was used to simulate the structures. Use of a layerwise model would be interesting to implement in order to simulate the layer-by-layer behavior of the FFF process and determine which layers should have fiber and its orientation.
- Further experimental studies of the material orientation technique should be implemented using better case studies to assess the practicality of the method.

Bibliography

[1] J. Stegmann. *Analysis and optimization of laminated composite shell structures*. PhD thesis, Aalborg University, 2004. URL https://www.researchgate.net/publication/235219180_Analysis_and_Optimization_of_Laminated_Composite_Shell_Structures. 1.1, 1.3.1, 2.1.2, 2.2, 2.2, 2.2, 2.3.4

[2] P. W. Christensen and A. Klarbring. Topology optimization of distributed parameter systems. In *An Introduction to Structural Optimization*, volume 153, pages 179–201. Springer Netherlands, Dordrecht, 2009. ISBN 978-1-4020-8666-3. doi: 10.1007/978-1-4020-8666-3_9. 1.1

[3] M. Caminero, J. Chacón, I. García-Moreno, and J. Reverte. Interlaminar bonding performance of 3d printed continuous fibre reinforced thermoplastic composites using fused deposition modelling. *Polymer Testing*, 68:415 – 423, 2018. ISSN 0142-9418. doi: https://doi.org/10.1016/j.polymertesting.2018.04.038. 1.2

[4] A. N. Dickson, J. N. Barry, K. A. McDonnell, and D. P. Dowling. Fabrication of continuous carbon, glass and Kevlar fibre reinforced polymer composites using additive manufacturing. *Additive Manufacturing*, 16:146–152, 2017. ISSN 2214-8604. doi: 10.1016/j.addma.2017.06.004. 1.2

[5] M. Caminero, J. Chacón, I. García-Moreno, and G. Rodríguez. Impact damage resistance of 3D printed continuous fibre reinforced thermoplastic composites using fused deposition modelling. *Composites Part B: Engineering*, 148:93–103, 2018. ISSN 1359-8368. doi: 10.1016/j.compositesb.2018.04.054. 1.2

[6] Markforged. https://markforged.com/products/composite/, . Accessed: 16-09-2019. 1.2

[7] Anisoprint. http://anisoprint.com/product-composer. Accessed: 16-09-2019. 1.2

[8] M. P. Bendsøe and N. Kikuchi. Generating optimal topologies in structural design using a homogenization method. *Computer Methods in Applied Mechanics and Engineering*, 71(2):197–224, 1988. ISSN 0045-7825. doi: 10.1016/0045-7825(88)90086-2. 1.3.1

[9] K. Suzuki and N. Kikuchi. A homogenization method for shape and topology optimization. *Computer Methods in Applied Mechanics and Engineering*, 93(3):291–318, 1991. ISSN 0045-7825. doi: 10.1016/0045-7825(91)90245-2. 1.3.1

[10] Y. Xie and G. Steven. A simple evolutionary procedure for structural optimization. *Computers & Structures*, 49(5):885–896, 1993. ISSN 0045-7949. doi: 10.1016/0045-7949(93)90035-C. 1.3.1

[11] O. Querin, G. Steven, and Y. Xie. Evolutionary structural optimisation (ESO) using a bidirectional algorithm. *Engineering Computations*, 15(8):1031–1048, 1998. ISSN 0264-4401. doi: 10.1108/02644409810244129. 1.3.1

[12] M. P. Bendsøe. Optimal shape design as a material distribution problem. *Structural Optimization*, 1(4):193–202, 1989. ISSN 0934-4373. doi: 10.1007/BF01650949. 1.3.1

[13] M. Zhou and G. Rozvany. The COC algorithm, Part II: Topological, geometrical and generalized shape optimization. *Computer Methods in Applied Mechanics and Engineering*, 89(1-3):309–336, 1991. ISSN 0045-7825. doi: 10.1016/0045-7825(91)90046-9. 1.3.1

[14] H. P. Mlejnek. Some aspects of the genesis of structures. *Structural Optimization*, 5(1-2):64–69, 1992. ISSN 0934-4373. doi: 10.1007/BF01744697. 1.3.1

[15] O. Sigmund. A 99 line topology optimization code written in Matlab. *Structural and Multidisciplinary Optimization*, 21(2):120–127, 2001. ISSN 1615-147X. doi: 10.1007/s001580050176. 1.3.1

[16] D.-K. Lee, D. Q. Hoan, L.-A. Tuan, K.-H. Lee, and J.-H. Lee. Topology optimization of laminated composite plates with isotropic and orthotropic material. 2015. URL `http://www.i-asem.org/publication_conf/asem15/1.ISEM15/3f/F2C.5.SM121_2165F1.pdf`. 1.3.1

[17] R. M. Hoglund. An Anisotropic Topology Optimization Method For Carbon Fiber-Reinforced Fused Filament Fabrication. Master's thesis, Baylor University, 2016. URL `http://hdl.handle.net/2104/9821`. 1.3.1, 3.2.1.1, 3.2.1.1

[18] P. Pedersen. On optimal orientation of orthotropic materials. *Structural Optimization*, 1(2):101–106, 1989. ISSN 0934-4373. doi: 10.1007/BF01637666. 1.3.1

[19] P. Pedersen. Bounds on elastic energy in solids of orthotropic materials. *Structural Optimization*, 2 (1):55–63, 1990. ISSN 0934-4373. doi: 10.1007/BF01743521. 1.3.1

[20] P. Pedersen. On thickness and orientational design with orthotropic materials. *Structural Optimization*, 3(2):69–78, 1991. ISSN 0934-4373. doi: 10.1007/BF01743275. 1.3.1

[21] L. V. Gibiansky and A. V. Cherkaev. Microstructures of Composites of Extremal Rigidity and Exact Bounds on the Associated Energy Density. In *Topics in the Mathematical Modelling of Composite Materials*, pages 273–317. Birkhäuser Boston, Boston, MA, 1997. ISBN 9783319971841. doi: 10.1007/978-1-4612-2032-9_8. 1.3.1

[22] M. Bruyneel and C. Fleury. Composite structures optimization using sequential convex programming. *Advances in Engineering Software*, 33(7-10):697–711, 2002. ISSN 0965-9978. doi: 10.1016/S0965-9978(02)00053-4. 1.3.1

[23] E. Lindgaard and E. Lund. Optimization formulations for the maximum nonlinear buckling load of composite structures. *Structural and Multidisciplinary Optimization*, 43(5):631–646, 2011. ISSN 1615-147X. doi: 10.1007/s00158-010-0593-8.

[24] P. Pedersen. Examples of density, orientation, and shape-optimal 2D-design for stiffness and/or strength with orthotropic materials. *Structural and Multidisciplinary Optimization*, 26(1-2):37–49, 2004. ISSN 1615-147X. doi: 10.1007/s00158-003-0295-6. 1.3.1

[25] H. P. Jia, C. D. Jiang, G. P. Li, R. Q. Mu, B. Liu, and C. B. Jiang. Topology Optimization of Orthotropic Material Structure. *Materials Science Forum*, 575-578:978–989, 2008. ISSN 1662-9752. doi: 10.4028/www.scientific.net/MSF.575-578.978. 1.3.1

[26] R. Hoglund and D. E. Smith. Continuous Fiber Angle Topology Optimization for Polymer Fused Filament Fabrication. *Solid Freeform Fabrication Symposium*, 1:1078–1090, 2016. URL `http://sffsymposium.engr.utexas.edu/sites/default/files/2016/088-Hoglund.pdf`. 1.3.1

[27] D. Jiang. Three dimensional topology optimization with orthotropic material orientation design for additive manufacturing structures. Master's thesis, Baylor University, 2017. URL `https://www.researchgate.net/publication/328580375_Three_dimensional_topology_optimization_with_orthotropic_material_orientation_design_for_additive_manufacturing_structures`. 1.3.1

[28] T. Nomura, E. M. Dede, J. Lee, S. Yamasaki, T. Matsumori, A. Kawamoto, and N. Kikuchi. General topology optimization method with continuous and discrete orientation design using isoparametric projection. *International Journal for Numerical Methods in Engineering*, 101(8):571–605, 2015. ISSN 0029-5981. doi: 10.1002/nme.4799. 1.3.1

[29] T. Nomura, E. M. Dede, T. Matsumori, and A. Kawamoto. Simultaneous Optimization of Topology and Orientation of Anisotropic Material using Isoparametric Projection Method. *11th World Congress on Structural and Multidisciplinary Optimization*, 2015. 1.3.1

[30] J. Stegmann and E. Lund. Discrete material optimization of general composite shell structures. *International Journal for Numerical Methods in Engineering*, 62(14):2009–2027, 2005. ISSN 0029-5981. doi: 10.1002/nme.1259. 1.3.1

[31] M. Bruyneel. SFP—a new parameterization based on shape functions for optimal material selection: application to conventional composite plies. *Structural and Multidisciplinary Optimization*, 43 (1):17–27, 2011. ISSN 1615-147X. doi: 10.1007/s00158-010-0548-0. 1.3.1

[32] T. Gao, W. Zhang, and P. Duysinx. A bi-value coding parameterization scheme for the discrete optimal orientation design of the composite laminate. *International Journal for Numerical Methods in Engineering*, 91(1):98–114, 2012. ISSN 0029-5981. doi: 10.1002/nme.4270. 1.3.1

[33] J. N. Reddy. *Mechanics of Laminated Composite Plates and Shells: Theory and Analysis*. CRC Press, London, 2nd edition, 2004. ISBN 9780203502808. doi: 10.1201/b12409. 2.1.2, 3.1

[34] J. N. Reddy. *An introduction to the finite element method*. McGraw-Hill, 3rd edition, 2006. ISBN 0072466855. 2.1.3, 3.1, 3.1, 3.1, 3.1, 3.1, 3.1, 3.1.1.1, 3.1.1.2

[35] O. Sigmund and S. Torquato. Design of materials with extreme thermal expansion using a three-phase topology optimization method. *Journal of the Mechanics and Physics of Solids*, 45(6):1037–1067, 1997. ISSN 0022-5096. doi: 10.1016/S0022-5096(96)00114-7. 2.2

[36] M. P. Bendsøe and O. Sigmund. *Topology Optimization: theory, methods and applications*, volume 95. Springer Berlin Heidelberg, Berlin, Heidelberg, 2004. ISBN 978-3-642-07698-5. doi: 10.1007/978-3-662-05086-6. 2.3.2, 3.2.1.1

[37] R. Sørensen and E. Lund. In-plane material filters for the discrete material optimization method. *Structural and Multidisciplinary Optimization*, 52(4):645–661, 2015. ISSN 1615-147X. doi: 10.1007/s00158-015-1257-5. 2.3.2, 2.3.4

[38] T. E. Bruns and D. A. Tortorelli. Topology optimization of non-linear elastic structures and compliant mechanisms. *Computer Methods in Applied Mechanics and Engineering*, 190(26-27):3443–3459, 2001. ISSN 0045-7825. doi: 10.1016/S0045-7825(00)00278-4. 2.3.2

[39] B. Bourdin. Filters in topology optimization. *International Journal for Numerical Methods in Engineering*, 50(9):2143–2158, 2001. ISSN 0029-5981. doi: 10.1002/nme.116. 2.3.2

[40] K. Svanberg. The method of moving asymptotes—a new method for structural optimization. *International Journal for Numerical Methods in Engineering*, 24(2):359–373, 1987. ISSN 0029-5981. doi: 10.1002/nme.1620240207. 2.3.3, 2.3.3

[41] N. Olhoff, M. P. Bendsøe, and J. Rasmussen. On CAD-integrated structural topology and design optimization. *Computer Methods in Applied Mechanics and Engineering*, 89(1-3):259–279, 1991. ISSN 0045-7825. doi: 10.1016/0045-7825(91)90044-7. 3.2.1

[42] P. Pedersen. Optimal Orientation of Anisotropic Materials Optimal Distribution of Anisotropic Materials Optimal Shape Design with Anisotropic Materials Optimal Design for a Class of Non-Linear Elasticity. In *Optimization of Large Structural Systems*, volume II, pages 649–681. Springer Netherlands, Dordrecht, 1993. doi: 10.1007/978-94-010-9577-8_32. 3.2.1.1

[43] ASTM D 3039/D 3039M – 00, Standard Test Method for Tensile Properties of Polymer Matrix Composite Materials. ASTM International. West Conshohocken, PA, 2002. doi: 10.1520/D3039_D3039M-08. URL `www.astm.org`. 4.1

[44] R. T. L. Ferreira, I. C. Amatte, T. A. Dutra, and D. Bürger. Experimental characterization and micrography of 3D printed PLA and PLA reinforced with short carbon fibers. *Composites Part B: Engineering*, 124:88–100, 2017. ISSN 1359-8368. doi: 10.1016/j.compositesb.2017.05.013. 4.1

[45] Markforged design guide. `https://s3.amazonaws.com/mf.product.doc.images/Composites_DesignGuide/CompositesDesignGuide_V1-2.pdf`, . Accessed: 16-09-2019.

Appendix A

Fiber Patterns

In the following section, all the obtained fiber patterns variations for the 3PT structure used to simulate the material distribution and orientation resulting from the optimizations are presented.

A.1 Fiber patterns variations for the 3PT structure

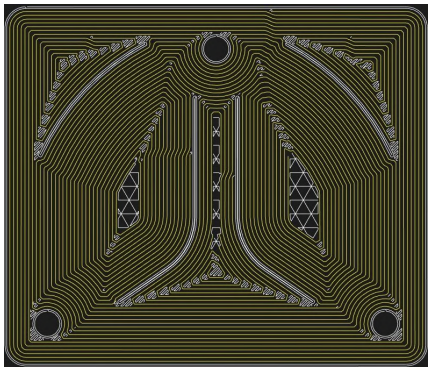

(a) Variation # 1

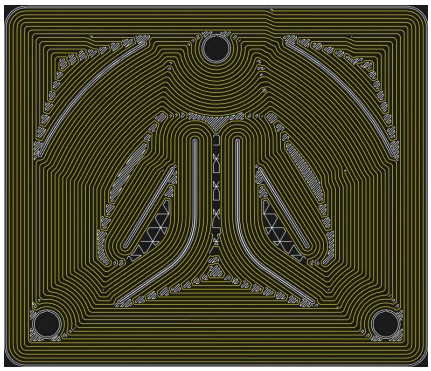

(b) Variation # 2

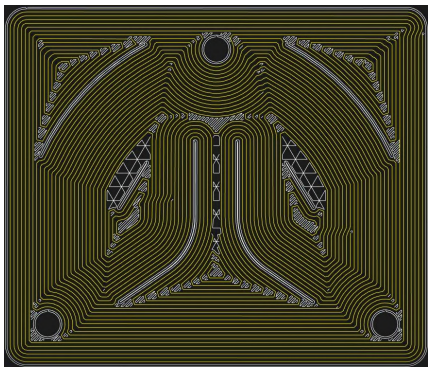

(c) Variation # 3

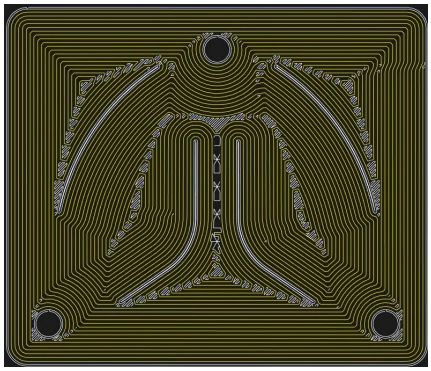

(d) Variation # 4

Figure A.1: Variations in printing pattern for the 3PT structure

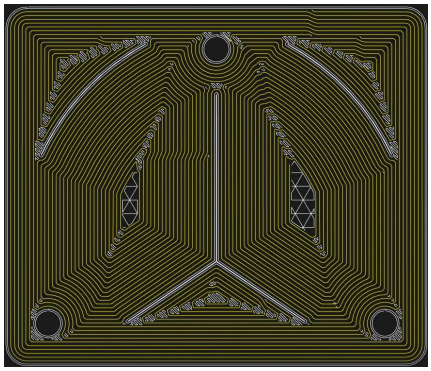

(c) Variation # 5

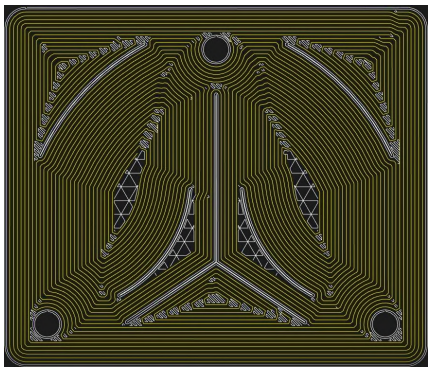

(d) Variation # 6

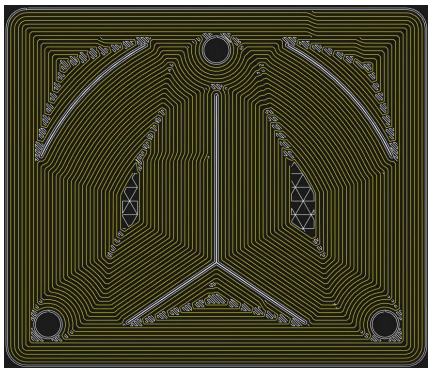

(e) Variation # 5

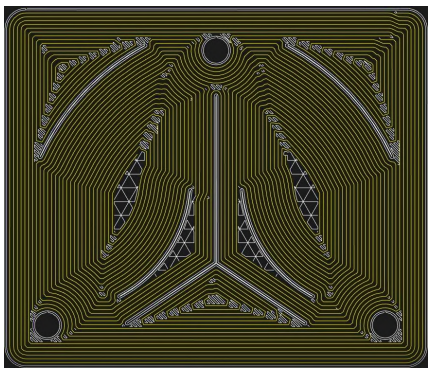

(f) Variation # 6

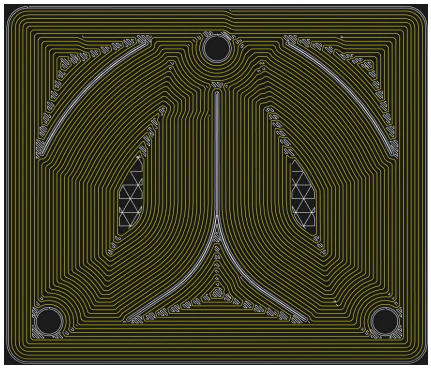

(g) Variation # 7

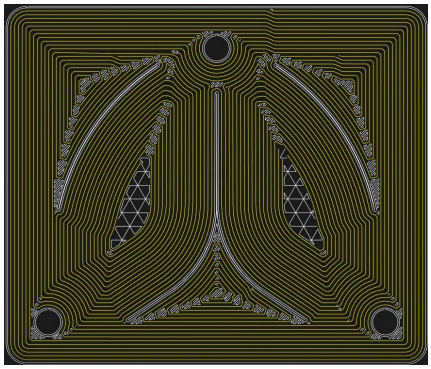

(h) Variation # 8

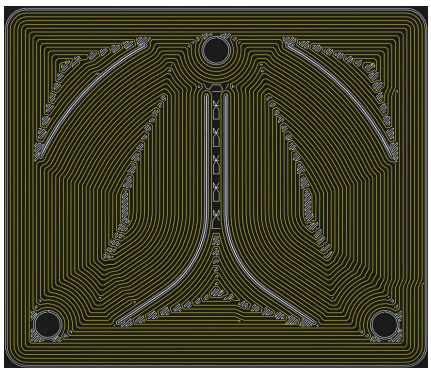

(i) Variation # 9

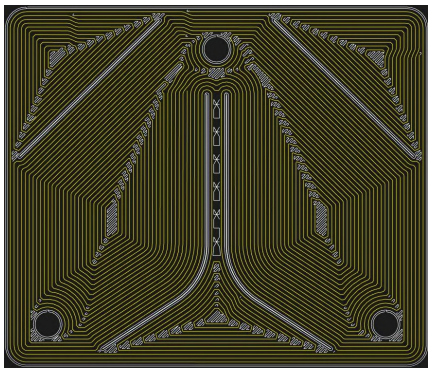

(j) Variation # 10

Figure A.1: Variations in printing pattern for the 3PT structure (cont.)

Appendix B

Technical Datasheets

B.1 Markforged's Composites Material Datasheet

MATERIAL DATASHEET

Composites

Markforged

Plastic Matrix	Test (ASTM)	Onyx	Nylon
Tensile Modulus (GPa)	D638	1.4	0.94
Tensile Stress at Yield (MPa)	D638	36	31
Tensile Strain at Yield (%)	D638	25	27
Tensile Stress at Break (MPa)	D638	30	54
Tensile Strain at Break (%)	D638	58	260
Flexural Strength (MPa)	D790[1]	81	32
Flexural Modulus (GPa)	D790[1]	2.9	0.84
Heat Deflection Temp (°C)	D648 B	145	49
Izod Impact - notched (J/m)	D256-10 A	330	1000
Density (g/cm^3)	—	1.2	1.1

Dimensions and Construction of Plastic Test Specimens:

- Tensile test specimens: ASTM D638 type IV beams
- Flexural test specimens: 3-pt. Bending, 4.5 in (L) x 0.4 in (W) x 0.12 in (H)
- Heat-deflection temperature at 0.45 MPa, 66 psi (ASTM D648-07 Method B)

All Markforged machines are equipped to print Onyx. Nylon is a specialized material that can only be printed on the Mark Two and X7. Machines that print Onyx cannot also print Nylon due to machine conditioning.

Markforged parts are primarily composed of plastic matrix. Users may add one type of fiber reinforcement in each part, enhancing its material properties.

1. Measured by a method similar to ASTM D790. Thermoplastic-only parts do not break before end of Flexural Test.

Fiber Reinforcement	Test (ASTM)	Carbon	Kevlar®	Fiberglass	HSHT FG
Tensile Strength (MPa)	D3039	800	610	590	600
Tensile Modulus (GPa)	D3039	60	27	21	21
Tensile Strain at Break (%)	D3039	1.5	2.7	3.8	3.9
Flexural Strength (MPa)	D790[1]	470	190	210	420
Flexural Modulus (GPa)	D790[1]	51	26	22	21
Flexural Strain at Break (%)	D790[1]	1.2	2.1	1.1	2.2
Compressive Strength (MPa)	D6641	320	97	140	192
Compressive Modulus (MPa)	D6641	54	28	21	21
Compressive Strain at Break (%)	D6641	0.7	1.5	—	—
Heat Deflection Temp (°C)	D648 B	105	105	105	150
Izod Impact - notched (J/m)	D256-10 A	960	2000	2600	3100
Density (g/cm^3)	—	1.4	1.2	1.5	1.5

Dimensions and Construction of Fiber Composite Test Specimens:

- Test plaques used in these data are fiber reinforced unidirectionally (0° Plies)
- Tensile test specimens: 9.8 in (L) x 0.5 in (H) x 0.048 in (W) (CF composites), 9.8 in (L) x 0.5 in (H) x 0.08 in (W) (GF and Kevlar® composites)
- Compressive test specimens: 5.5 in (L) x 0.5 in (H) x 0.085 in (W) (CF composites), 5.5 in (L) x 0.5 in (H) x 0.12 in (W) (Kevlar® and GF composites)
- Flexural test specimens: 3-pt. Bending, 4.5 in (L) x 0.4 in (W) x 0.12 in (H)
- Heat-deflection temperature at 0.45 MPa, 66 psi (ASTM D648-07 Method B)

Tensile, Compressive, Strain at Break, and Heat Deflection Temperature data were provided by an accredited 3rd party test facility. Flexural data were prepared by Markforged, Inc. These represent typical values.

Markforged tests plaques are uniquely designed to maximize test performance. Fiber test plaques are fully filled with unidirectional fiber and printed without walls. Plastic test plaques are printed with full infill. To learn more about specific testing conditions or to request test parts for internal testing, contact a Markforged representative.

Part and material performance will vary by fiber layout design, part design, specific load conditions, test conditions, build conditions, and the like.

This representative data were tested, measured, or calculated using standard methods and are subject to change without notice. Markforged makes no warranties of any kind, express or implied, including, but not limited to, the warranties of merchantability, fitness for a particular use, or warranty against patent infringement; and assumes no liability in connection with the use of this information. The data listed here should not be used to establish design, quality control, or specification limits, and are not intended to substitute for your own testing to determine suitability for your particular application. Nothing in this sheet is to be construed as a license to operate under or a recommendation to infringe upon any intellectual property right.

MATERIAL DESCRIPTIONS

Composites

Markforged

Printing Methods

Plastic Matrix

In Fused Filament Fabrication (FFF), the printer heats thermoplastic filament to near melting point and extrudes it through its nozzle, building a plastic matrix layer by layer. Markforged prints all thermoplastics by this method.

Onyx Nylon

Fiber Reinforcement

Continuous Filament Fabrication (CFF) is our unique technology that adds fiber reinforcement to printed parts. Within our thermoplastic matrix, Markforged uses proprietary technology to lay down continuous long-strand fiber. Users can control the layers reinforced, amount, orientation, and type of reinforcing fiber.

Fiberglass Carbon Fiber Kevlar® HSHT Fiberglass

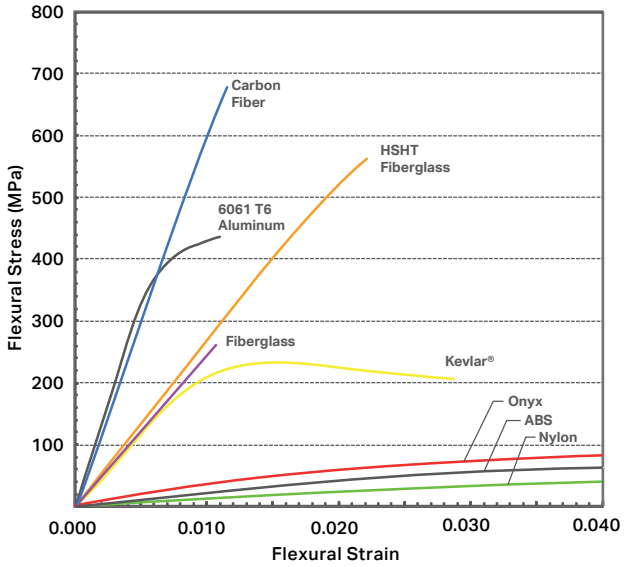

Materials

Onyx Plastic

Engineering Grade Thermoplastic

Onyx yields stiff, strong, and accurate parts. Already 1.4 times stronger and stiffer than ABS, Onyx can be reinforced with any continuous fiber. Onyx sets the bar for surface finish, chemical resistivity, and heat tolerance.

Flexural Strength	**81 MPa**
Flexural Stiffness	**2.9 GPa**

Fiberglass Fiber

Reinforced Fiber Strength

Fiberglass is our entry level continuous fiber, providing high strength at an accessible price. 2.5 times stronger and eight times stiffer than Onyx, Fiberglass reinforcement results in strong, robust tools.

Flexural Strength	**210 MPa**
Flexural Stiffness	**22 GPa**

Carbon Fiber Fiber

Aluminum Strength. Half the Weight.

Carbon Fiber has the highest strength to weight ratio of our reinforcing fibers. Six times stronger and eighteen times stiffer than Onyx, Carbon Fiber reinforcement is commonly used for parts that replace machined aluminum.

Flexural Strength	**470 MPa**
Flexural Stiffness	**51 GPa**

Nylon Plastic

Tough Flexible Thermoplastic

Nylon parts are flexible, impact-resistant and can be reinforced with any Markforged continuous fiber. The material works best in applications that require increased flexibility or low working friction.

Flexural Strength	**32 MPa**
Flexural Stiffness	**0.84 GPa**

Kevlar® Fiber

Lightweight, Durable, and Strong

Kevlar® possesses excellent durability, making it optimal for parts that experience repeated and sudden loading. As stiff as fiberglass and much more ductile, it's best used for end of arm tooling.

Flexural Strength	**190 MPa**
Flexural Stiffness	**26 GPa**

HSHT Fiberglass Fiber

Strength at High Temperatures

High Strength High Temperature (HSHT) Fiberglass exhibits Aluminum strength and high heat tolerance. Five times as strong and seven times as stiff as Onyx, it's best used for parts loaded in high operating temperatures.

Flexural Strength	**420 MPa**
Flexural Stiffness	**21 GPa**